MULTIPLE-PULSE TECHNIQUES FOR SOLID-STATE NUCLEAR MAGNETIC RESONANCE SPECTROSCOPY OF MATERIALS

ANTHONY D. MONTINA

B. Sc., University of Lethbridge, 2007

A Thesis

Submitted to the School of Graduate Studies

of the University of Lethbridge

in Partial Fulfillment of the

Requirements for the Degree

MASTER OF SCIENCE

Department of Chemistry and Biochemistry

University of Lethbridge

LETHBRIDGE, ALBERTA, CANADA

© Anthony D. Montina, 2010

To my loving wife Lyndsay, whose support for me is never-ending!

ABSTRACT

Solid state NMR has the ability to obtain detailed structural information at the molecular level in materials. This has led to the development of a large number of high resolution techniques, some of which utilize multiple pulse methods. The behaviour of these multiple pulse techniques has, to date, been explained using either relaxation or spin dynamics. Ultimately, an explanation based on a combination of both dynamics is required in order to properly understand the underlying mechanism of these techniques. This work presents an explanation of the experimental behaviour observed for three multiple pulse domain selection techniques: the DIVAM, Direct DIVAM, and Refocused DIVAM sequences. This is based on a combination of spin and relaxation dynamics and is accomplished using both analytical expressions and simulations obtained using a general simulation program for solid-state NMR spectroscopy (SIMPSON).

ACKNOWLEDGEMENTS

I would like to start off by expressing my deepest gratitude to my supervisor Dr. Paul Hazendonk. Paul has supported me through my years of research and, most importantly, put up with me for 5 years. I have also received a large amount of support from a few other academics that I would like to thank. Dr Filip Wormald has been a great friend and source of both information and assistance throughout my graduate degree. Dr David Siminovitch taught me a vast amount of Solid State NMR theory throughout the duration of courses in both my undergraduate and graduate degrees. Dr. Dinu Iuga taught me an 8 month course in experimental NMR and it was through a combination of this course and the rest of his training that I have learnt most of what I know about an NMR lab. Dr. Paul Hayes and Dr. Albert Cross served on my Masters committee and were a source of guidance for the entire duration of my Masters degree. Dr Joseph Rasmussen supervised me through some of the early stages of my career and helped me to develop both research and communication skills. I also would like to express my appreciation to the University of Lethbridge, The School of Graduate Studies, and the province of Alberta for this great opportunity and funding.

Lastly, I would like to thank all of my friends and family, especially my wife Lyndsay, for their support and patience throughout these long years. I would also like to thank an old friend, Stephen Cronin, for his support. It was because of Steve that I found my way into research and the world of NMR.

TABLE OF CONTENTS

LIST OF TABLES

LIST OF FIGURES

1. INTRODUCTION

1.1 Overview

Nuclear Magnetic Resonance (NMR) was independently discovered in 1946 by both Felix Bloch and Edward Mills Purcell.[1-2] Since this time numerous one- and two-dimensional techniques for application in both the solid- and solution-state have been developed.[3] These range from numerous through bond and through space multi-dimensional experiments to specialized one-dimensional experiments for determining parameters such as the dipolar coupling[4-6]. The large diversity and capabilities in available NMR experiments makes it a very powerful spectroscopic tool for the investigation of materials in the solid state.

The physical science and principles which form the foundation for an understanding of NMR[1-2] will be introduced along with a description of how NMR spectroscopy is being applied to polymer science as a tool for studying structure and dynamics. Section 1.2 reviews some basic angular momentum principles in physics and how these combine to form a classical picture of NMR.[7-10] Once the classical description of NMR is complete the quantum mechanical description can be established. Section 1.3 beings with a recap of the key concepts behind quantum mechanics[11-12] and concludes by developing the Hamiltonian used to describe NMR spectroscopy.[13-17] With this Hamiltonian in hand, the key differences between solution and solid state NMR can be explained. Section 1.4 outlines some of the key solid-state NMR (SSNMR) techniques used in this work, such as: magic angle spinning, decoupling, cross-polarization, and the Hahn echo. Lastly, Section 1.5 presents a brief review of polymer science and the various ways in which SSNMR spectroscopy has been applied to the study of polymer structure and dynamics.

1.2 Classical NMR

1.2.1 Spin, Angular Momentum, and Magnetism

All matter is composed of atoms which contain three different types of fundamental particles: electrons, protons, and neutrons. The nucleus of an atom is composed of the later two particles (nucleons) and these give rise to the three intrinsic properties of nuclei: mass, charge, and spin. All nuclei are defined by three numbers, the atomic number, mass number, and ground state nuclear spin quantum number, and the last of these is determined by the quantum mechanical property of nuclear spin. Each nucleus possesses spin and it is the number of neutrons and protons, given by the mass and atomic numbers, that determines whether the spin quantum number (I) is a positive integer ($0,1,2,....,n$) or half-integer ($\frac{1}{2},\frac{3}{2},\ldots,\frac{n}{2}$).

Nuclei which have a non-zero spin possess the intrinsic quantum mechanical property of spin angular momentum. The value of spin angular momentum (m) along the z-direction is quantized into 2I+1 sub-levels, ranging from –I to I in integer steps. For example, a nucleus with spin = ½ has two possible spin angular momentum values: m = ½ and –½, while a nucleus with spin = 1 has three possible values: $m=-1,0,and\,1$. Under normal circumstances, the energies resulting from the different spin angular momentum values are equivalent (degenerate) and cannot be utilized spectroscopically. The application of an external magnetic field lifts this degeneracy and provides a means to perform NMR spectroscopy.

As mentioned earlier, nuclei possess mass, charge, and spin. In the absence of an external magnetic field the magnetic moments of each spin, or nuclei, are randomly

aligned and cancel each other out, resulting in no net bulk magnetization (figure 1a). The application of an external magnetic field lifts the degeneracy of the angular momentum states and leads the magnetic moment of each spin to align either with or against the magnetic field (figure 1b).

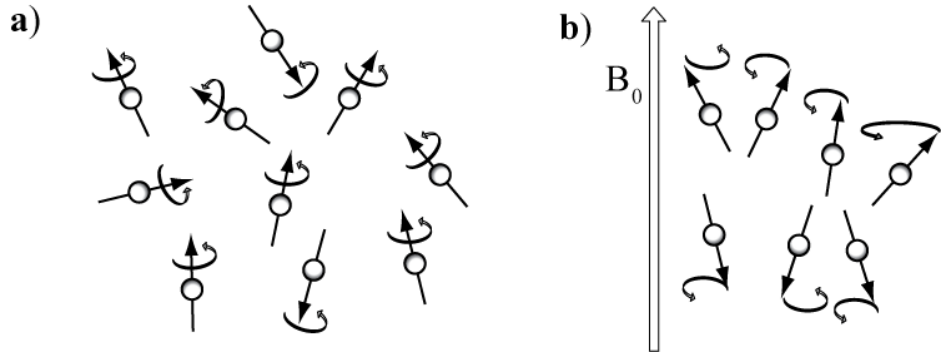

Figure 1 Alignment of spins in the absence (a) and presence (b) of a static magnetic field.[13]

The splitting of the energies into 2I+1 levels is known as *Zeeman Splitting* (figure 2). The energy value for each of these levels can be determined by looking at the interaction between the nucleus and the static magnetic field.

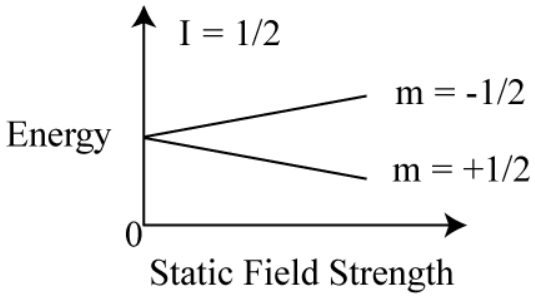

Figure 2 Zeeman splitting of the energy levels for a spin ½ in the presence of a static magnetic field.

Once the nucleus is placed in an external magnetic field its magnetic moment ($\boldsymbol{\mu}$) interacts with the field ($\mathbf{B}_0$) and experiences a torque given by:

$$\boldsymbol{\tau} = \boldsymbol{\mu} \times \mathbf{B}_0 \tag{1}$$

This causes the nucleus to precess, or rotate, along the direction of the applied magnetic field at an angular frequency of ω as shown in figure 3.

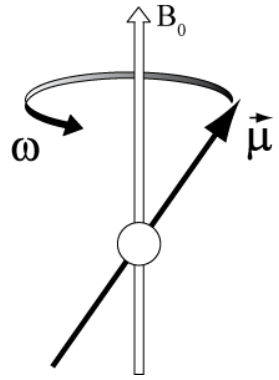

Figure 3 Precession of the magnetic moment of a nucleus in the presence of a static magnetic field.[18]

The energy required for a nucleus to precess in any of these 2I+1 levels is now equivalent to the work done by exerting this torque over the rotation angle θ (Work Energy Theorem).[19] The energy of a magnetic moment in a magnetic field is therefore given by:

$$W = E = \int \boldsymbol{\mu} \times \mathbf{B} d\theta = \int |\mu||\mathbf{B}| \sin\theta d\theta = -|\boldsymbol{\mu}||\mathbf{B}| \cos\theta = -\boldsymbol{\mu} \cdot \mathbf{B} \tag{2}$$

The vectors for angular momentum and the magnetic moment both occur in the rotation direction caused by the torque, and are therefore parallel. This results in a scaling factor that is a known as the gyromagnetic ratio:

$$\boldsymbol{\mu} = \gamma \mathbf{J} \tag{3}$$

The gyromagnetic ratio is a charge to mass ratio that is unique to each nucleus.

$$\gamma = \frac{\boldsymbol{\mu}}{\mathbf{J}} = \frac{q}{2m} \tag{4}$$

Now by substituting equation 3 into equation 2 the energy can be re-expressed in terms of angular momentum.

$$E = -\gamma \mathbf{J} \cdot \mathbf{B} \tag{5}$$

The applied field (B_0) is arbitrarily chosen to be along the z axis and as a result of the dot product only the J_z term remains. Substituting $J_z = \hbar m$, where m is the angular momentum value and $\hbar = h / 2\pi$, into equation 5 gives the final expression for the Zeeman energy levels in figure 2.

$$E_m = -\gamma \hbar m B_0 \tag{6}$$

Earlier it was mentioned that the torque experienced by a nucleus in the presence of a magnetic field leads to precession of the nuclei about the applied magnetic field (B_0) (figure3). The angular frequency (ω) at which nuclei precess can be obtained from the energy of the various 2I+1 angular momentum spin states. The energy required for a transition from the higher to the lower energy state, for the case of I = ½, can be given by the difference in their energies:

$$E = E_f - E_i = \gamma \hbar B_0 = \hbar \omega_0 \tag{7}$$

where the angular frequency is given by:

$$\omega_0 = \gamma B_0 \tag{8}$$

Since the angular frequency of precession depends upon the gyromagnetic ratio, and Equation 4 shows that this ratio is unique to each nucleus, the frequency must also be unique to each nucleus and is known as the Larmor frequency.

Now that the properties of a single spin in the presence of a magnetic field have been outlined, an understanding of how a collection of many spins (referred to as an ensemble of spins) behaves, can be examined. In the presence of an external magnetic field individual spins will either align with or against the field. Parallel orientations correspond to the lower energy state with m = ½ (spin up), while anti-parallel orientations correspond to a slightly higher energy state with m = –½ (spin down). According to the Boltzmann distribution there will always be slightly more spins in the low energy state then in the high energy state. This gives rise to a net longitudinal magnetization that has cylindrical symmetry due to spin precession, as seen in figure 4.

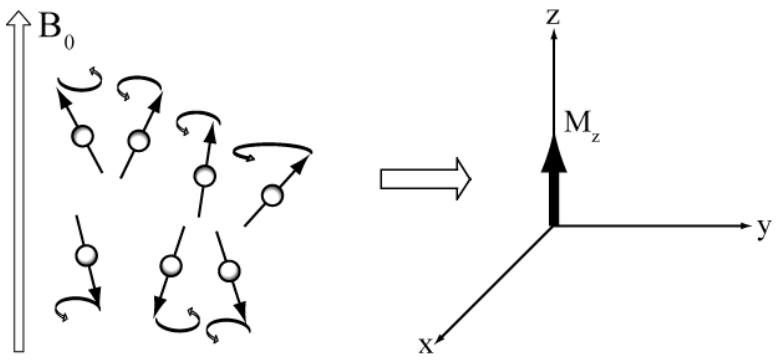

Figure 4 The alignment of spins in the presence of a static magnetic field and the resulting net magnetization.

1.2.2 The NMR Magnet

The static field (B_0) that is used to create Zeeman splitting in an NMR experiment is generated by a magnet.[20] Most modern magnets consist of a solenoid made from a superconducting Sn/Nb alloy that is submersed in a bath of liquid helium which is surrounded by a separate dewar containing liquid nitrogen. B_0 must not only be as strong as possible, it must also be as homogenous as possible with an accuracy of at least 1 part in 10^9 over the entire volume of a sample. This is why two sets of smaller solenoids, or

shims, are present and act as small adjustments to the magnetic field. One of these sets is located inside the liquid helium bath while the other is located inside the bore of the magnet and they are known as the cryo- and room-temperature shims, respectively. The strength of an NMR magnet is usually given in terms of the Larmor frequency of protons as given by equation 10. This corresponds to a conversion of γ = 42.58 MHz / Tesla; therefore a static field with a strength of 11.7441 Tesla is more commonly referred to as a 500 MHz field.

1.2.3 The NMR Experiment and Signal Generation

As mentioned earlier, when a sample is introduced to a static magnetic field a net bulk magnetization (**M**) is induced along the longitudinal plane. The NMR experiment measures how a state of the magnetization changes with respect to time in the transverse plane. Before this can be explained an understanding of how this bulk magnetization changes in time for all planes must be presented. In the following text the magnetization ($\boldsymbol{\mu}$) will be replaced with the bulk magnetization (**M**) of the spin ensemble. First, consider that a torque produces a change in angular momentum with respect to time in the following manner:

$$\boldsymbol{\tau} = \frac{d\mathbf{J}}{dt} = \frac{1}{\gamma}\frac{d\mathbf{M}}{dt} \tag{9}$$

Taking equation 9 and equating it to equation 1 gives us an equation that describes how the net magnetization changes with respect to time.

$$\frac{d\mathbf{M}}{dt} = \gamma(\mathbf{M} \times \mathbf{B}) \tag{10}$$

As the net magnetization is parallel to the static field there is no change in the magnetization with respect to time. This means that the magnetization must be put in the transverse, or x-y, plane for any change to be detected.

The magnetization is placed in the transverse plane with the application of a radio frequency (RF) pulse (B_1) applied on-resonance with the Larmor frequency of the nuclei, as shown in figure 5.

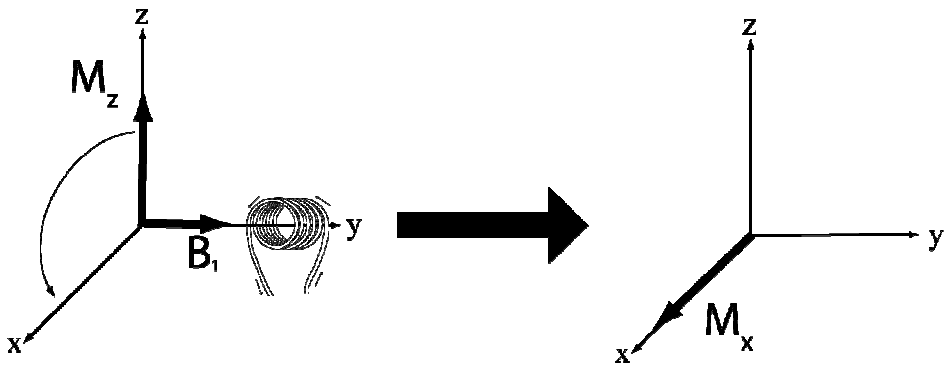

Figure 5 The application of a 90 degree B_1 pulse and its effect on the net magnetization.

This RF pulse is generated by a coil which has its winding axis placed along the x-y plane. Once the magnetization is in the transverse plane it will precess at the Larmor frequency as shown in figure 6a.

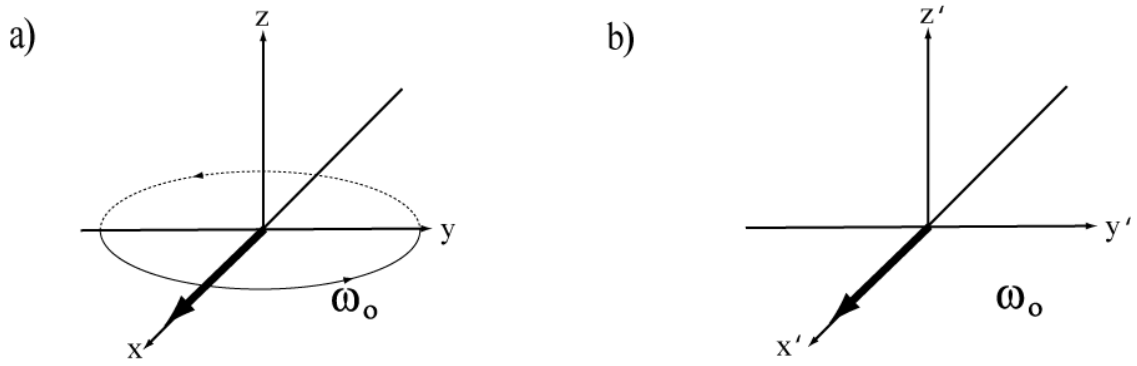

Figure 6 a) Precession of the transverse magnetization at the Larmor frequency in the laboratory frame of reference. b) Transverse magnetization in the Rotating frame of reference.

At this point it is much easier to describe the magnetization in terms of a rotating frame of reference in which the frame is rotating at the Larmor frequency. In this frame the magnetization appears static as shown in figure 6b. Precession in the x-y plane leads to an oscillating magnetic field, which in turn induces a current that can now be detected in the same coil that was used to apply the B_1 pulse, due to the principle of reciprocity.[21-22] However, once the RF pulse is turned off the spins do not continue to precess in a perpetual manner, but instead return back to the equilibrium state over time through a process known as relaxation.

1.2.4 Relaxation and the Bloch Equations

Spins in a bulk sample are not isolated and interact with both their surroundings and each other. It is these interactions which lead bulk matter to relax back to a distribution of thermal equilibrium. There are two types of relaxation known as longitudinal (T_1) and transverse (T_2) relaxation. Longitudinal relaxation, also known as spin-lattice relaxation, is the process by which a longitudinally polarized state, prepared by the application of an RF pulse, returns back to thermal equilibrium. Figure 7

illustrates this process by following M_z as a function of time during the NMR experiment.

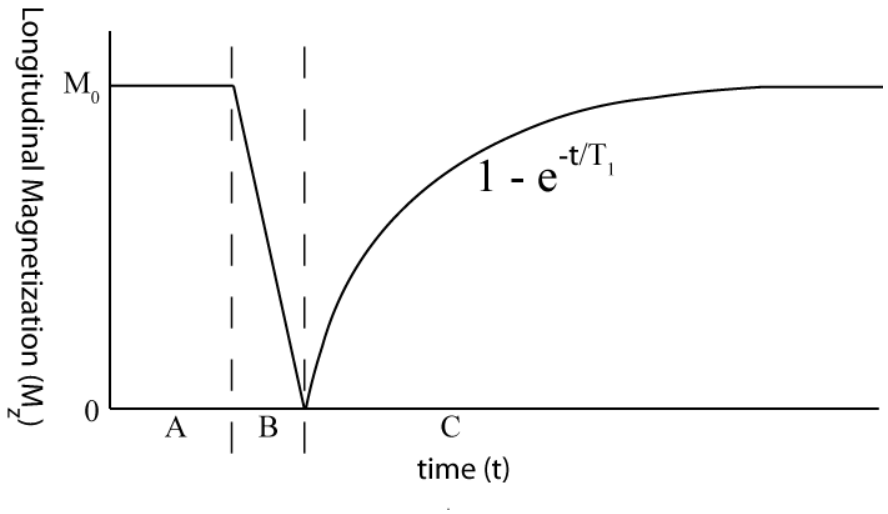

Figure 7 Recovery of the equilibrium magnetization according to the longitudinal relaxation rate T_1. The time periods A, B, and C correspond to the equilibrium state, the application of a 90 degree pulse, and the recycle delay, respectively.

All spins experience small fluctuating magnetic fields which are random in nature and caused by molecular motion of neighboring spins. In the absence of a static magnetic field these fluctuations lead to the isotropic distribution of spins as shown in figure 1a. The presence of a static magnetic field creates a bias in these fluctuations and leads to the eventual recovery of the net magnetization along the direction of the static field. This recovery process is facilitated by an energy exchange between the spins and their surrounding environment. The return to equilibrium is attributed to an exponential recovery characterized by the longitudinal relaxation rate constant (T_1).

$$M_z = M_0(1-e^{-t/T_1}) \tag{11}$$

The time scale of T_1 will be dependent on the factors which influence the fluctuating magnetic fields, such as temperature and viscosity, and can range from ms to days.

As mentioned above**,** an RF pulse can be used to rotate the longitudinal magnetization into the transverse plane. The ensemble of spins is rotated together resulting in in-phase, or coherent, transverse magnetization. Over time individual spins will experience small fluctuations in the local magnetic field which are caused by local time dependent magnetic fields. These fluctuations cause the spins to precess at slightly different speeds from one another and results in the loss of coherence, or magnetization, in the transverse plane. Figure 8 illustrates this process by following the transverse magnetization (M_{xy}) as a function of time during the NMR experiment.

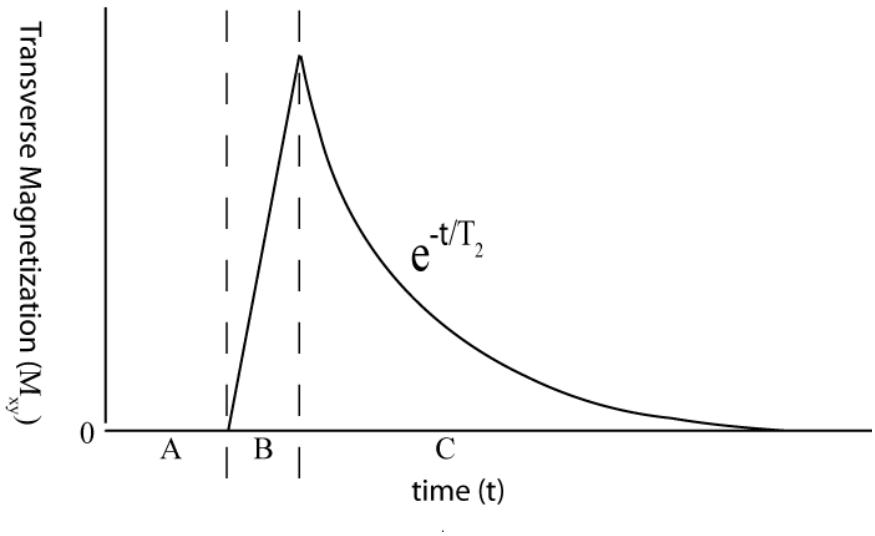

Figure 8 Decay of the transverse magnetization according to the transverse relaxation rate T_2. The time periods A, B, and C correspond to the non excited state, the application of a 90 degree pulse, and the acquisition time, respectively.

The loss of transverse magnetization does not represent any exchange of energy with the surrounding environment and is characterized by an exponential decay associated with the transverse relaxation rate constant (T_2), as given by equation 12.

$$M_{xy} = M_0 e^{-t/T_2} \tag{12}$$

In solution-state experiments the spin-spin interactions are modulated in time by molecular motion and this gives rise to the randomly fluctuating magnetic fields mentioned earlier. Consequently, both T_2 and T_1 are related to a Brownian process that is random in nature and are therefore incoherent. Section 1.3.3 will cover the internal interactions of the Hamiltonian and these interactions are coherent processes.

The Bloch equation (equation 13) describes the change in magnetization with respect to time and takes into account the effects of relaxation.

$$\frac{d\mathbf{M}}{dt} = \gamma\mathbf{M}\times\mathbf{B} + \frac{1}{T_1}(M_0 - \mathbf{M}_Z) - \frac{1}{T_2}(\mathbf{M}_x + \mathbf{M}_y) \tag{13}$$

The first term in equation 15 represents the precession term of the magnetization, the second represents the recovery of M_Z magnetization, or return to equilibrium, due to T_1, and the third represents the loss of magnetization in the transverse plane due to T_2. This represents a conical like trajectory for the magnetization as it returns to equilibrium, as seen in figure 9a. The detected NMR signal, which corresponds to the induced current in the transverse plane during this motion, is referred to as the free induction decay (FID) and can be seen in figure 9b.

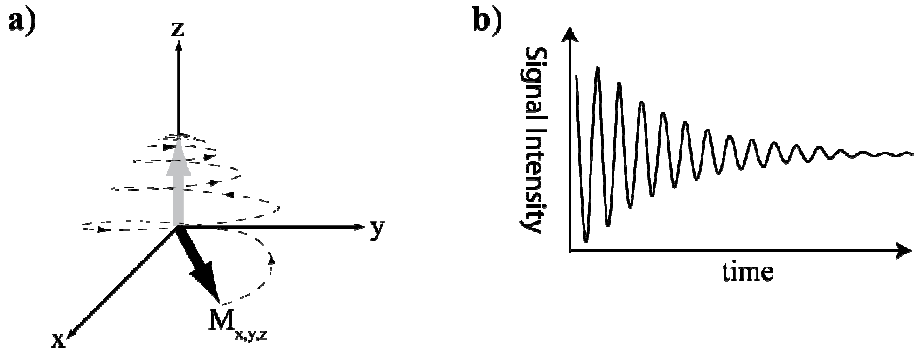

Figure 9 Conical trajectory of the transverse magnetization during the relaxation process (a) and the resulting FID (b).[7]

The mathematical description of the FID, or signal (S), is a complex function as given by equation 14:

$$S(t) = S_0 e^{(i\omega t)} e^{-\frac{t}{T_2}} \tag{14}$$

This first exponential term contains a complex function that can be expanded into the following form:

$$e^{i\omega t} = \cos(\omega t) + i\sin(\omega t) \tag{15}$$

The sign of the exponential determines whether the peak will occur at $+\omega$ or $-\omega$. As a direct result, the signal in terms of both the x and y plane is required in order to determine this sign; however this would require two coils. Alternatively, the signal detected from one coil can be treated as two separate signals. The first is generated from digitizing the original signal and becomes the real, or x, component of the time domain. The second is generated by adding a phase shift of 90 degrees to the original signal before it is subsequently digitized and this becomes the complex, or imaginary, component of the time domain. This method of creating the two orthogonal components of the time domain signal out of one detected signal is known as quadrature detection.[23]

1.2.5 The Fourier Transform

The NMR signal, or FID, is a frequency encoded time dependant signal, meaning that it contains a relationship between time and frequency known as the reciprocal relationship.[24] Therefore, the FID signal can be detected as a function of time, digitized, and subsequently transformed, via a Fourier transformation (FT), into a spectrum as a function of frequency. The FT relationship between the time and frequency domains is given by:

$$S(\omega) = \int_0^\infty S(t)e^{-i\omega t}dt = A(\omega) - iD(\omega) \tag{16}$$

The transformed spectrum now contains a signal as a function of frequency where the real and imaginary components of the signal represent the absorption ($A(\omega)$) and dispersion ($D(\omega)$) line shapes, respectively. Figure 10 illustrates the FT of the real and imaginary time signals into an absorption and dispersion peak, respectively.

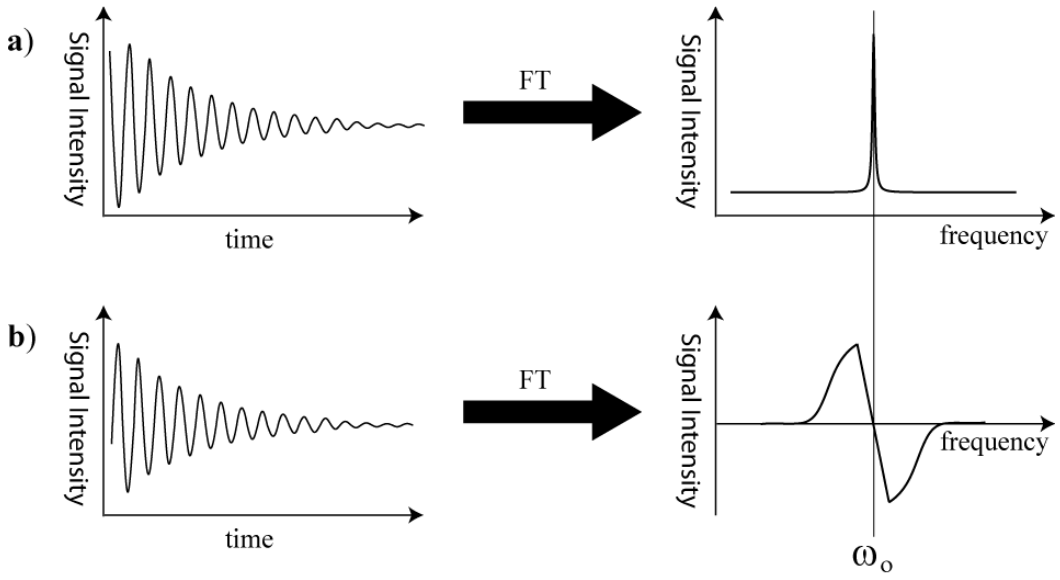

Figure 10 The spectrum produced as a result of the application of a Fourier transform to the (a) real and (b) imaginary components of the FID.

The combination of absorption and dispersion signals in an NMR spectrum can result in phase distortions in the observed line shapes. These can be removed by including a phase correction factor (ϕ) in the time dependant signal and results in the following equation for the signal as a function of frequency:

$$S(\omega) = \int_0^\infty S(t)e^{-i\omega t}e^{i\phi}dt \tag{17}$$

The effects of combining absorption and dispersions lines will be further discussed when examining the effects of a pulse offset in Refocused DIVAM (see section 3.6).

The timing and order of events in an NMR experiment is important when designing an experiment and is depicted in a standard format known as a pulse sequence diagram. The pulse sequence diagram for the basic NMR experiment, as outlined in this chapter, can be seen in figure 11.

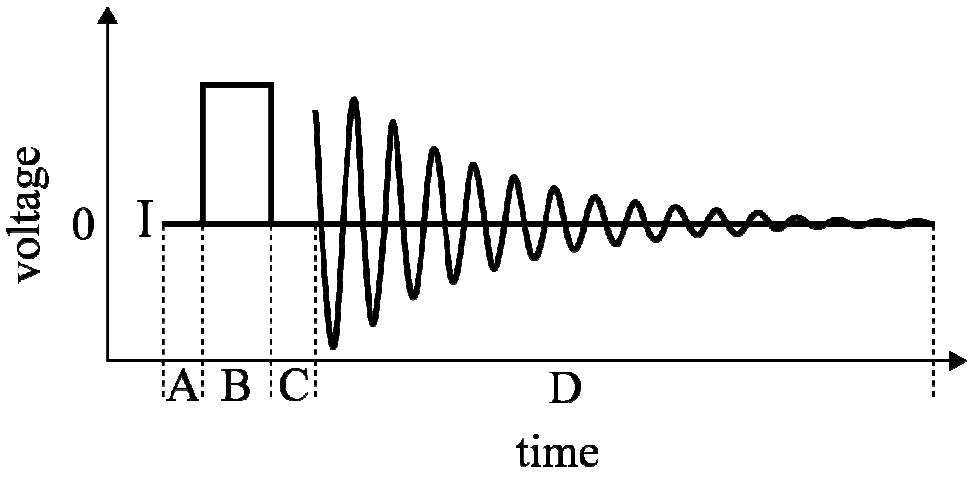

Figure 11 General pulse sequence diagram for the basic NMR experiment on nuclei **I,** where the time delays A, B, C, and D represent the pre-pulse delay, duration of the 90 degree pulse, pre-acquisition delay, and the acquisition time, respectively.

Much more complicated NMR experiments involve use of decoupling schemes during acquisition, as well as multiple channels and nuclei. These more advanced sequences will follow the same scheme as shown here and will be presented and discussed later.

1.3 The NMR Hamiltonian

1.3.1 Quantum Mechanics

It was stated earlier that spin angular momentum is an intrinsic quantum mechanical property of nuclei. Now that the classical mechanics of NMR has been outlined, a quantum mechanical picture describing an ensemble of spins will be presented. The quantum mechanical treatment of an ensemble describes the state of an ensemble of spins at any particular moment of time and how it changes in time. This is an invaluable tool when attempting to explain or predict experimental observations. However, a quick review of some basics concepts in quantum mechanics must be given before discussing its application to NMR.[11-13, 25-28]

The concept of particle-wave duality suggests that matter behaves both as a particle and wave simultaneously. This means that a particle must be described by wave mechanics using a wave function. The wave function gives the amplitude of a particle as a complex function of space and time: $\Psi(x,t)$. The intensity of the wave function can be obtained by taking the modulus squared of the function. This represents the probability that the particle will be found at that position at that time and is given by:

$$P = \left|\Psi(x,t)\right|^2 = \Psi(x,t)^*\Psi(x,t) \tag{18}$$

The asterisk in equation 18 indicates that the function is the complex conjugate of the original function. Since the wave function represents a probability it must be normalized and orthogonal (orthonormal) as seen in equation 19.

$$\int_{-\infty}^{\infty} \Psi_m(x,t)^*\Psi_n(x,t)dx = \delta_{mn} \tag{19}$$

The function at the end of equation 19 is known as the Kronecker delta function (δ_{mn}) and is equal to zero when m ≠ n and one when m = n.

The time-dependant Schrodinger equation can be used to explain how a wave function will evolve as a function of time, as given by:

$$i\hbar \frac{d}{dt}\Psi(x,t) = \widehat{H}\Psi(x,t) \tag{20}$$

The Hamiltonian in Equation 20 ($\widehat{H}$) can be used to determine the state of the system at a later point in time, as long as the initial state is known, in the following manner:

$$\Psi(x,t) = e^{-i\hbar\widehat{H}(t-t_0)}\Psi(x,t_0) = U(t-t_0)\Psi(x,t_0) \tag{21}$$

The operator $U(t-t_0)$ is known as the propagator and it describes how the system will change in time under the evolution of the Hamiltonian. The Schrodinger equation can be further simplified if it has the following separable form:

$$\Psi(x,t) = \psi(x)\phi(t) \tag{22}$$

In this case, the time-independent Schrodinger equation can be obtained from equation 22 in the following manner:

$$\widehat{H}\psi(x) = E\psi(x) \tag{23}$$

The above equation represents a Hamiltonian, given by $\widehat{H}$, acting on the wave function and returning back the same wave function multiplied by a scalar value, where the returned scalar value represents the energy of the system.

The Hamiltonian and the Schrodinger equation are an example of a Hermitian operator and an Eigen-relationship, respectively, where the latter is defined by the following:

$$\hat{A}|n\rangle = a|n\rangle \tag{24}$$

The expectation value represents the weighted average value of an observable, described by an operator $\hat{A}$, if a measurement is performed multiple times on the system and is given by:

$$\left\langle \hat{A} \right\rangle = \int_{-\infty}^{\infty} \hat{A}|\psi(x)|^2 \, dx \tag{25}$$

An expectation value is time independent if and only if the operator commutes with the Hamiltonian of the system according to the following relationship.

$$\left[\hat{A}, \hat{H}\right] = \hat{A}\hat{H} - \hat{H}\hat{A} = 0 \tag{26}$$

If the commutator, shown in equation 26, does not equal zero then the two operators do not commute. The expectation value will be further discussed when examining the density matrix.

The separable time component of the wave function is given by:

$$\phi(t) = e^{i\omega t} \tag{27}$$

The modulous squared of a complex function is always equal to one and as a result the probability of finding the particle at a certain position is now independent of time:

$$P = |\Psi(x,t)|^2 = |\psi(x)|^2 \, |\phi(t)|^2 = |\psi(x)|^2 \tag{28}$$

The time-independent wave function is referred to as a stationary state

Spin is an abstract concept that is not a function of space and must be described in a different manner, known as Dirac notation, where the time-independent orthonormal wave functions are represented in the following manner:

$$\psi_n(x) = |n\rangle \tag{29}$$

$$\psi_m(x)^* = \langle m| \tag{30}$$

Equation 29 is referred to as the "ket" while equation 30 is referred to as the "bra" (bra-ket notation) and the application of a bra followed by a ket implies integration. Now, substituting equations 29 and 30 into equation 19 gives the following form of the orthonormal wave function:

$$\langle m||n\rangle = \delta_{mn} \tag{31}$$

Recall that the presence of a static magnetic field results in Zeeman splitting of the energy levels. In the case of I = ½, these energy levels correspond to the angular momentum values of m = ½ and m = –½. The value of ½ is the low energy state (aligned parallel to the magnetic field), while the value of –½ is the high energy state (aligned anti-parallel to the magnetic field) and these shall now be referred to as the alpha (α) and beta (β) states, respectively. The alpha and beta states can be formulated as vectors in the following manner:

$$|\alpha\rangle = |I,m\rangle = \left|\frac{1}{2},\frac{1}{2}\right\rangle = \begin{pmatrix}1\\0\end{pmatrix} \tag{32}$$

$$|\beta\rangle = |I,m\rangle = \left|\frac{1}{2},-\frac{1}{2}\right\rangle = \begin{pmatrix}0\\1\end{pmatrix} \tag{33}$$

These two states can now be used to describe a single spin ½ system. In order to extract the energy information from a state the Hamiltonian operator must be formed, which can then subsequently act on these states in the following manner:

$$\widehat{H}|n\rangle = E_n|n\rangle \tag{34}$$

Now that the representations of the eigenvectors for spin ½ have been outlined, the common operators which are present in the Hamiltonian and the result of their operations can be presented.

There are two sets of operators that can be present in the Hamiltonian, angular momentum and rotation operators. In the specific case of spin ½ there are several important angular momentum operators which must be considered. Recall that the total angular momentum consists of three components: $\hat{I}_x, \hat{I}_y$, and $\hat{I}_z$. The operators which represent these angular momentum states do not commute and obey the following cyclic commutation relationship:

$$\left[\hat{I}_x, \hat{I}_y\right] = i\hat{I}_z \quad \circlearrowleft \tag{35}$$

As a result of equation 35, no two individual components of angular momentum may be known at the same time; therefore the total angular momentum (***I***) cannot be known. However, the square of the total angular momentum can be calculated by equation 36 and this operator does commute with each of the individual angular momentum operators.

$$\hat{I}^2 = \hat{I}_x^2 + \hat{I}_y^2 + \hat{I}_z^2 \tag{36}$$

Each of the individual angular momentum operators, for the case of I = ½, has a matrix form which is given in equations 37-39.

$$\hat{I}_x = \frac{1}{2}\begin{pmatrix} 0 & 1 \\ 1 & 0 \end{pmatrix} \tag{37}$$

$$\hat{I}_y = \frac{1}{2i}\begin{pmatrix} 0 & 1 \\ -1 & 0 \end{pmatrix} \tag{38}$$

$$\hat{I}_z = \frac{1}{2}\begin{pmatrix} 1 & 0 \\ 0 & -1 \end{pmatrix} \tag{39}$$

The effect of the $\hat{I}_z$ operator on the alpha and beta states is given in equation 40.

$$\hat{I}_z|\alpha\rangle = \frac{1}{2}|\alpha\rangle \quad \textit{and} \quad \hat{I}_z|\beta\rangle = -\frac{1}{2}|\beta\rangle \tag{40}$$

Using equation 39 our Hamiltonian can be given by:

$$\widehat{H}_z = -\gamma \mathbf{J}\cdot\mathbf{B} = -\gamma\hbar B_0 \hat{I}_z \tag{41}$$

We can now apply this Hamiltonian to equation 34 and the resulting eigenvectors will represent the energy of each state:

$$-\gamma\hbar B_0 \hat{I}_z|\alpha\rangle = -\frac{1}{2}\gamma\hbar B_0|\alpha\rangle \quad \textit{and} \quad -\gamma\hbar B_0 \hat{I}_z|\beta\rangle = \frac{1}{2}\gamma\hbar B_0|\beta\rangle \tag{42}$$

Notice that the quantum mechanical picture has now provided the energy of each state in the spin ½ system and these are identical to the values derived earlier in the classical NMR section. The energy level diagram representing a single spin can be seen in figure 12.

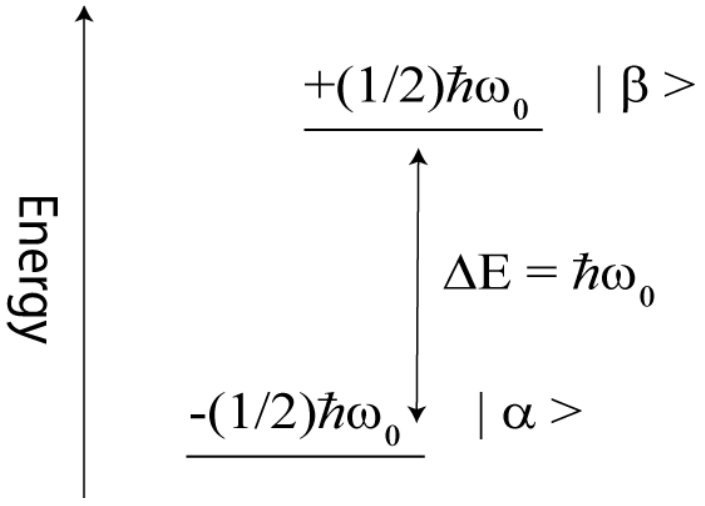

Figure 12 Energy level diagram for a single spin system.

Recall that the matrix forms of $\hat{I}_x$ and $\hat{I}_y$ are not diagonal and this is a direct result of the fact that they do not commute with $\hat{I}_z$. A more convenient way to investigate the effects of these operators is to form the raising and lowering operators (referred to as the ladder operators) in the following manner:

$$\hat{I}^+ = \hat{I}_x + i\hat{I}_y = \begin{pmatrix} 0 & 1 \\ 0 & 0 \end{pmatrix} \quad and \quad \hat{I}^- = \hat{I}_x - i\hat{I}_y = \begin{pmatrix} 0 & 0 \\ 1 & 0 \end{pmatrix} \tag{43}$$

The ladder operators can now be applied to each of the states and have the following effect:

$$\begin{aligned} \hat{I}^+ |\alpha\rangle &= 0 \qquad \hat{I}^+ |\beta\rangle = |\alpha\rangle \\ \hat{I}^- |\alpha\rangle &= |\beta\rangle \qquad \hat{I}^- |\beta\rangle = 0 \end{aligned} \tag{44}$$

It is clear that the raising operator increases the state from beta to alpha state ($\Delta m = +1$) while the lowering operator decreases the state from alpha to beta ($\Delta m = -1$); therefore, the ladder operators represent the transitions between the energy levels shown in figure 12.

The last operators to be discussed are the rotational operators. If three operators follow the rules of cyclic commutation, such as the angular momentum operators, then they must also obey the following sandwich formula for rotations:

$$\hat{R}_A(\theta)\,\hat{B}\,\hat{R}_A(\theta)^{-1} = \mathrm{e}^{-i\theta\hat{A}}\,\hat{B}e^{i\theta\hat{A}} = \hat{B}\cos\theta + \hat{C}\sin\theta \quad \circlearrowleft \tag{45}$$

A summary of the rotation of each angular momentum operator by the other angular momentum operators can be found in Equation 46.[25]

$$
\begin{aligned}
e^{-i\theta\hat{I}_x}\begin{Bmatrix}\hat{I}_x\\ \hat{I}_y\\ \hat{I}_z\end{Bmatrix}e^{i\theta\hat{I}_x} &= \begin{Bmatrix}\hat{I}_x\\ \hat{I}_y\cos\theta+\hat{I}_z\sin\theta\\ \hat{I}_z\cos\theta-\hat{I}_y\sin\theta\end{Bmatrix}\\
e^{-i\theta\hat{I}_y}\begin{Bmatrix}\hat{I}_x\\ \hat{I}_y\\ \hat{I}_z\end{Bmatrix}e^{i\theta\hat{I}_y} &= \begin{Bmatrix}\hat{I}_x\cos\theta-\hat{I}_z\sin\theta\\ \hat{I}_y\\ \hat{I}_z\cos\theta+\hat{I}_x\sin\theta\end{Bmatrix}\\
e^{-i\theta\hat{I}_z}\begin{Bmatrix}\hat{I}_x\\ \hat{I}_y\\ \hat{I}_z\end{Bmatrix}e^{i\theta\hat{I}_z} &= \begin{Bmatrix}\hat{I}_x\cos\theta+\hat{I}_y\sin\theta\\ \hat{I}_y\cos\theta-\hat{I}_x\sin\theta\\ \hat{I}_z\end{Bmatrix}
\end{aligned}
\tag{46}
$$

These rotations will be discussed and further applied when considering the effect of an RF pulse on an ensemble of spins.

Recall that the eigenvectors for spin ½ presented above represent the stationary state, or time-independent state, of the quantum mechanical system. However, any form or combination of these states is possible as long as the total wave function is normalized.

$$
|\psi\rangle = c_\alpha(t)|\alpha\rangle + c_\beta(t)|\beta\rangle \tag{47}
$$

The above wave function represents a combination of the two spin states, where $c_\alpha(t)$ and $c_\beta(t)$ are coefficients that represent time dependent complex numbers. This combination of states is now time dependant and is known as a superposition state, as it generally does not have an eigen-relationship with the Hamiltonian (equation 24). Using the description of the alpha and beta states provided in equations 32 and 33 results in the following form of the superposition state:

$$|\psi\rangle = \begin{pmatrix} c_\alpha(t) \\ c_\beta(t) \end{pmatrix}$$
$$\langle\psi| = \begin{pmatrix} c_\alpha(t)^* & c_\beta(t)^* \end{pmatrix} \tag{48}$$

This newly formed superposition state can now be used to calculate the expectation value of an observable, or function, in the following manner:

$$\left\langle \hat{Q} \right\rangle = \langle\psi|\hat{Q}|\psi\rangle \tag{49}$$

Similarly, the expectation value can also be found with the following equation:

$$\left\langle \hat{Q} \right\rangle = Tr\left\{ |\psi\rangle\langle\psi|\hat{Q} \right\} \tag{50}$$

The above form involves taking the trace, or sum of the diagonal components, of the product between the newly formed projection operator ($|\psi\rangle\langle\psi|$) and the original operator $\hat{Q}$.

Now that the representation of the superposition state for a single spin has been presented it can be used to develop a description for the entire ensemble (or the bulk sample) of spins. First consider the expectation value for two spins:

$$\begin{aligned} \left\langle \hat{Q} \right\rangle &= \langle\psi_1|\hat{Q}|\psi_1\rangle + \langle\psi_2|\hat{Q}|\psi_2\rangle \\ &= Tr\left\{ \left(|\psi_1\rangle\langle\psi_1| + |\psi_2\rangle\langle\psi_2| \right)\hat{Q} \right\} \end{aligned} \tag{51}$$

This description for the expectation operator can very easily be extended to the general problem of N-spins, or an ensemble or spins:

$$\left\langle \hat{Q} \right\rangle = Tr\left\{ \left(|\psi_1\rangle\langle\psi_1| + |\psi_2\rangle\langle\psi_2| + ... + |\psi_N\rangle\langle\psi_N| \right)\hat{Q} \right\} \tag{52}$$

Now we can describe a new operator, referred to as the density operator, which is given by the average of the projection operators for N spins.

$$\begin{aligned}\hat{\rho}(t) &= N^{-1}\left(|\psi_1\rangle\langle\psi_1| + |\psi_2\rangle\langle\psi_2| + \ldots + |\psi_N\rangle\langle\psi_N|\right) \\ &= \overline{|\psi\rangle\langle\psi|}\end{aligned} \tag{53}$$

The average expectation operator for the entire ensemble of spins can now be given by:

$$\langle Q\rangle = Tr\left\{\hat{\rho}(t)\hat{Q}\right\} \tag{54}$$

All that now remains is to develop the density operator for the case of spin ½.

The density operator can be obtained by calculating the projection operator over an average of all spins. Recall that equation 48 gave the superposition state for a single spin ½. This superposition state can now be used to calculate the original projection operator.

$$|\psi\rangle\langle\psi| = \begin{pmatrix} c_\alpha(t) \\ c_\beta(t) \end{pmatrix}\begin{pmatrix} c_\alpha(t)^* & c_\beta(t)^* \end{pmatrix} = \begin{pmatrix} c_\alpha(t)c_\alpha(t)^* & c_\alpha(t)c_\beta(t)^* \\ c_\beta(t)c_\alpha(t)^* & c_\beta(t)c_\beta(t)^* \end{pmatrix} \tag{55}$$

Taking the average of each element in the projection operator gives the final form of the density matrix for an ensemble of spins.

$$\hat{\rho}(t) = \overline{|\psi\rangle\langle\psi|} = \begin{pmatrix} \overline{c_\alpha(t)c_\alpha(t)^*} & \overline{c_\alpha(t)c_\beta(t)^*} \\ \overline{c_\beta(t)c_\alpha(t)^*} & \overline{c_\beta(t)c_\beta(t)^*} \end{pmatrix} \tag{56}$$

Recall that the modulous squared of a complex number is equal to one. This means that the diagonal elements of the density matrix are time-independent; therefore they represent the stationary, or energy, states of the system. In contrast, the off-diagonal elements of the density matrix are time-dependant and represent the coherence order of the spin system. Figure 13 shows how the density matrix elements can now be represented in terms of the energy level diagram presented earlier.

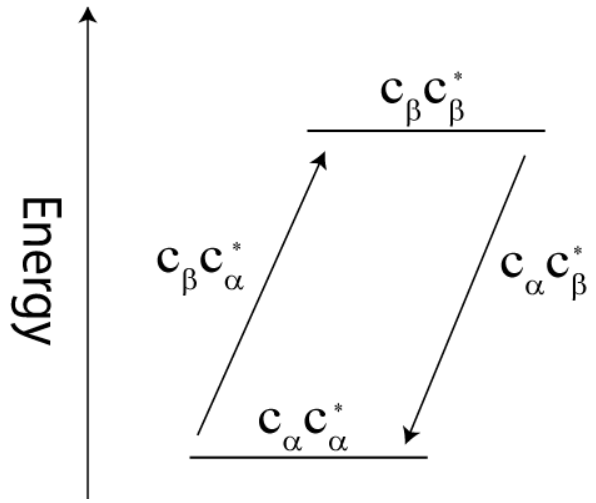

Figure 13 Energy level diagram in terms of the density matrix elements.

Note that the off-diagonal components of the density matrix have the same effect on the spin system as the raising and lowering operators, while the diagonal elements are similar to the I_z operator. This allows the density matrix to be re-written in terms of the spin operators (matrices) in the following manner:

$$\begin{aligned}\hat{\rho}(t) = &\left(\overline{c_\alpha(t)c_\alpha(t)^*} - \overline{c_\beta(t)c_\beta(t)^*}\right)\hat{I}_z + \left(\overline{c_\alpha(t)c_\alpha(t)^*} + \overline{c_\beta(t)c_\beta(t)^*}\right)\frac{1}{2}\hat{1} \\ &+\left(\overline{c_\beta(t)c_\alpha(t)^*}\right)\hat{I}^+ + \left(\overline{c_\alpha(t)c_\beta(t)^*}\right)\hat{I}^-\end{aligned} \tag{57}$$

An interaction in a spin system is given by a Hamiltonian and the effect that this has on the density matrix can be obtained from the time-dependant Schrodinger equation:

$$\frac{d\hat{\rho}(t)}{dt} = -i\left[\hat{H}(t), \hat{\rho}(t)\right] \tag{58}$$

Equation 58 is also known as the Liouville-von Neumann equation of motion and, as long as the initial density matrix describing the system ($\hat{\rho}(0)$) is known, it can be solved for a given time (t) in the following manner:

$$\hat{\rho}(t) = e^{-i\hat{H}t}\,\hat{\rho}(0)e^{i\hat{H}t} \tag{59}$$

The exponential term ($e^{-i\hat{H}t}$) is more commonly referred to as the propagator (explained earlier), as it governs the propagation of the system through time.

Earlier, equation 57 illustrated that the density matrix can be represented in a form corresponding to the spin matrices. The density matrix can now be represented by a vector of the following form:

$$\hat{\rho}(t) = \begin{pmatrix} \hat{I}_z \\ \hat{I}^+ \\ \hat{I}^- \\ \hat{E} \end{pmatrix} \tag{60}$$

This vector can now be transformed into Liouville space where the Liouvillian superoperator is given by:

$$\hat{\hat{L}} = \left(H \otimes E - E \otimes H\right) \tag{61}$$

The Liouvillian can now be used to simplify the time-dependent Schrodinger equation (equation 58) in the following manner:

$$\frac{d\hat{\rho}(t)}{dt} = -i\hat{\hat{L}}(t), \hat{\rho}(t) \tag{62}$$

Equation 62 can now be solved for a given time in a similar fashion to equation 59:

$$\hat{\rho}(t) = e^{-i\hat{\hat{L}}t - \hat{\hat{R}}t}\,\hat{\rho}(0) \tag{63}$$

$\hat{\hat{R}}$ and $\hat{\hat{L}}$ are the Relaxation and Liouvillian superoperators, respectively, and are given by the following:

$$\hat{\hat{L}} = \begin{pmatrix} 0 & 0 & 0 & 0 \\ 0 & \hbar\omega & 0 & 0 \\ 0 & 0 & -\hbar\omega & 0 \\ 0 & 0 & 0 & 0 \end{pmatrix}$$

$$\hat{\hat{R}} = \begin{pmatrix} \frac{1}{T_1} & 0 & 0 & 0 \\ 0 & \frac{1}{T_2} & 0 & 0 \\ 0 & 0 & \frac{1}{T_2} & 0 \\ 0 & 0 & 0 & 0 \end{pmatrix} \quad (64)$$

The transformation of the system to Liouville space allows for the inclusion of relaxation effects in the propagator. This now provides a form of describing the system that is similar to the Bloch Equations presented in the classical NMR section, where $\hat{I}^+, \hat{I}^-, \hat{I}_z$, can be related directly to the components of the magnetization. Unfortunately, moving the system to Liouville space takes the calculation of the propogator to a much larger scale. This increased scale creates numerous computational difficulties when dealing with large spin systems and these will be discussed later in section 1.4.7. Now that a full quantum mechanical description for an ensemble of spins has been described each of the external and internal terms of the Hamiltonian can be discussed.

1.3.2 The External Interactions of the Hamiltonian

The two most important external terms in the Hamiltonian are the interaction with the static field and an applied RF pulse. The Hamiltonian representing the interaction between the static field and each spin is given in equation 65 and is known as the Zeeman interaction.

$$\widehat{H}_j^{static} = -\gamma_j B_0 \hat{I}_{j,z} \tag{65}$$

The indices in the $\hat{I}_{j,z}$ term represent the spin index (j) and the spatial index in terms of Cartesian coordinates (z). The interaction of the static field with the entire ensemble of spins can easily be represented by summing up all of the individual interactions resulting from equation 65. It is important to note that the Zeeman interaction, under most circumstances, is the largest and most dominate term in the Hamiltonian, with an interaction strength on the order of hundreds of MHz.

As mentioned earlier, the magnetization is rotated into the transverse plane through the application of an RF pulse (B_1) that is on-resonance with the Larmor frequency. This pulse is actually the sum of two counter rotating components of B_1 in the transverse plane, where one component is on-resonance and the other is off-resonance. In most cases, the off-resonance component has no effect on the spins and can be neglected, leaving the following form for an RF pulse:

$$B_{RF} = B_{res}^{RF} = \frac{1}{2} B_{RF} \sin\theta_{RF} \left\{ \cos\left(\omega_{ref} t + \phi_p\right) \hat{I}_{j,x} + \sin\left(\omega_{ref} t + \phi_p\right) \hat{I}_{j,y} \right\} \tag{66}$$

Equation 66 can now be put into the original Hamiltonian:

$$\widehat{H}_j^{RF} = -\gamma \cdot B_{RF} = -\frac{1}{2} \gamma_j B_{RF} \sin\theta_{RF} \left\{ \cos\left(\omega_{ref} t + \phi_p\right) \hat{I}_{j,x} + \sin\left(\omega_{ref} t + \phi_p\right) \hat{I}_{j,y} \right\} \tag{67}$$

The θ_{RF} term in equation 67 represents the angle between the static field and the RF coil; therefore with the coil located in the transverse plane this term is equal to one. The reference frequency of the pulse is given by ω_{ref} and corresponds to the Larmor frequency of the nuclei being excited by the pulse. The phase of the pulse is given by ϕ_p and allows

for the pulse to be located on any of the four directions in the transverse plane (x, -x, y, -y).

The current form of the Hamiltonian for an RF pulse is in the laboratory frame of reference, resulting in a time-dependant Hamiltonian. A time-dependant system is much more difficult to work with than a time-independent one. For this reason the Hamiltonian is transformed to the rotating frame of reference (explained earlier) where it becomes time independent and has the following form:

$$\widehat{\widehat{H}}_j^{RF} = \frac{1}{2}\gamma_j B_{RF} \sin\theta_{RF} (\hat{I}_x \cos\phi_p + \hat{I}_y \sin\phi_p) \tag{68}$$

Now that the time dependence has been removed the effect of an RF pulse and the role its phase (ϕ_p) plays can be easily examined.

An RF pulse with a phase of zero ($\phi_p = 0$) corresponds to an x-pulse given by the following Hamiltonian:

$$\widehat{\widehat{H}}_j^{RF} = \frac{1}{2}\gamma_j B_{RF} \sin\theta_{RF} \widehat{I}_x \tag{69}$$

Likewise, a phase of π/2, π, and 3π/2 corresponds to a y,-x, and –y pulse respectively. Equation 69 can be thought of as a rotation about the x-axis, or $\widehat{I}_x$ operator, by an angle known as the excitation angle (θ_p). The excitation angle is given by the following:

$$\theta_p = \omega_{nut}\tau_p \quad where \quad \omega_{nut} = \left|\frac{1}{2}\gamma B_{RF} \sin\theta_{RF}\right| \tag{70}$$

The excitation angle is always positive and is given by both the amplitude of the pulse (ω_{nut}) and the duration of the pulse (τ_p). The result of the rotation caused by an RF pulse along the x, y, -x, -z axis can be given by the propagators shown in equation 46 where θ

$= \theta_p$. For example, the application of a rotation along the x-axis ($\widehat{I_x}$) with a flip angle (θ_p) of 90 degrees ($\frac{\pi}{2}$) when applied to the static magnetization (I_z) is given by:

$$\widehat{\rho}(t) = e^{-i\frac{\pi}{2}\hat{I}_x}\hat{I}_z e^{i\frac{\pi}{2}\hat{I}_x} = \hat{I}_z \cos\frac{\pi}{2} - \hat{I}_y \sin\frac{\pi}{2} = -\hat{I}_y \tag{71}$$

The result of the rotation in equation 71 is the magnetization being aligned on the –y-axis, or a $-I_y$ magnetization.

1.3.3 The Internal Interactions of the Hamiltonian

Now that the external interactions of the Hamiltonian have been explained an understanding of the sources of magnetic field fluctuations internal to the sample can be presented. As mentioned earlier, the internal interactions are not random and represent coherent processes within the system. The internal Hamiltonian can be greatly simplified if we consider the presence of a strong external magnetic field (secular approximation) and molecular motion.

In general, the internal interactions presented below are small when compared to the Zeeman interaction, therefore each interaction is formulated in a manner such that it is quantized along the z-axis, or the B_0 field. All of the internal interactions can be thought of as a sum of two terms in the following manner:

$$\widehat{H} = \hat{A} + \hat{B} \tag{72}$$

Consider $\hat{A}$ to be a large term, such as the Zeeman interaction, and $\hat{B}$ to be a small term, when compared to $\hat{A}$. Any of the individual elements of $\hat{B}$ which are small compared to the eigenvalues of $\hat{A}$ can be neglected. This occurs when the commutator (equation 26)

between the two operators does not equal zero. This approach, known as the secular approximation, leads to a much simpler Hamiltonian and will be applied in all of the following text.

Rapid molecular motion, which is common in both the liquid and gas state, can be used to further simplify the Hamiltonian. If the molecular motion is sufficiently fast then an internal interaction can be replaced by its motionally averaged value ($\overline{\overline{H}}$). This simplification allows for the removal of any terms in the Hamiltonian which average to zero, as will be the case when discussing the dipolar Hamiltonian in solution-state NMR. The terms which have been removed due to both the secular approximation and motional averaging are responsible for the relaxation, or incoherent processes, of the system and can now be studied separately from the internal (coherent) interactions, or spin dynamics, of the system. This separation of time scales will be applied when discussing the results presented in chapters 2 and 3.

I. The Chemical Shift

Earlier it was mentioned that the Fourier transform of an FID gives rise to the signal as a function of frequency, with a peak occurring at the Larmor frequency of the nuclei of interest. The electrons of a sample are charged particles and in the presence of a magnetic field they begin to circulate and produce a current. The induced current has two components which contribute to the total current: the diamagnetic and paramagnetic terms. The diamagnetic and paramagnetic current is produced by the circulation of electrons in their ground state and in an excited state, respectively. The paramagnetic term leads to rapid relaxation of the NMR signal and this makes the study of

paramagnetic systems by NMR spectroscopy very difficult to implement.[29-30] Most NMR spectroscopy is carried out on diamagnetic systems and from this point forward only diamagnetic contributions will be considered. The diamagnetic current produces an induced magnetic field which can either add to or subtract from the static magnetic field experienced by a spin as seen in figure 14.

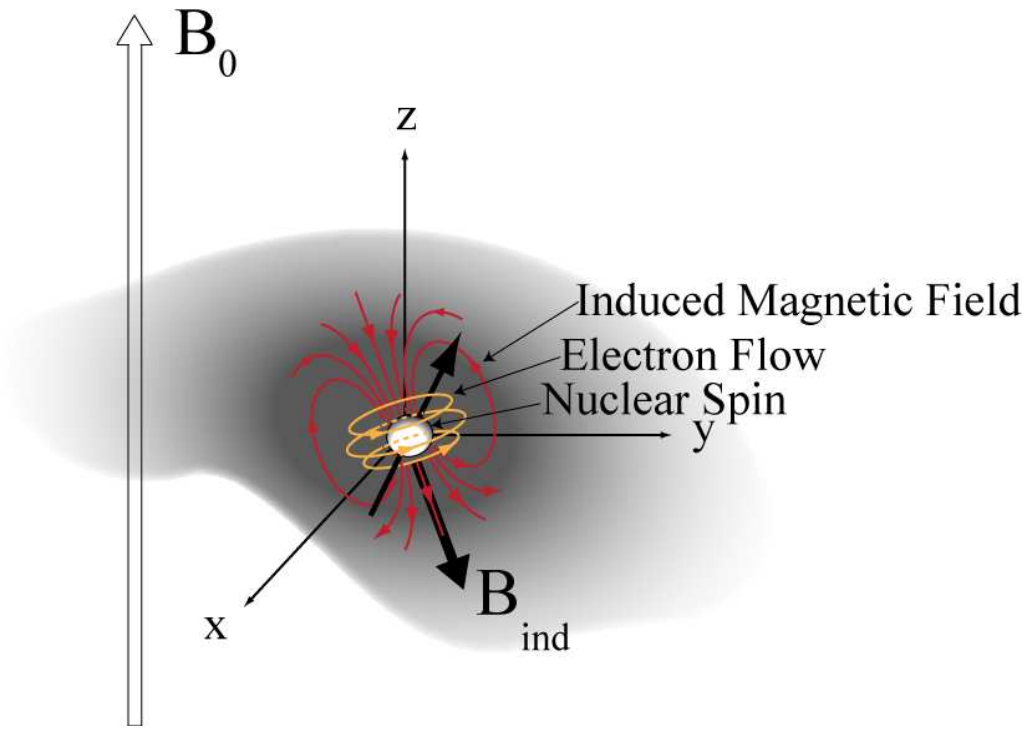

Figure 14 Schematic representation of the induced magnetic field produced by electron circulation in the presence of a static magnetic field.[18]

The local magnetic field experienced by a spin ($\mathbf{B}_j^{loc}$) can now be given by the sum of the induced magnetic field ($\mathbf{B}_j^{induced}$) and the static magnetic field ($\mathbf{B}_0$), and is given by equation 73.

$$\mathbf{B}_j^{loc} = \mathbf{B}_0 + \mathbf{B}_j^{induced} \tag{73}$$

The induced magnetic field is small when compared to the static field ($\sim 10^{-4} \cdot B_0$) but does produce a small shift in the Larmor frequency, which is known as the chemical shift. The induced magnetic field is given by:

$$\mathbf{B}_{induced} = \sigma \cdot \mathbf{B}_0 \tag{74}$$

The induced field depends on the molecules' orientation with respect to the static magnetic field. The chemical shielding tensor (σ) is a 3 x 3 matrix that relates the orientation of the static field to the vector of the induced magnetic field.

$$\sigma = \begin{pmatrix} \sigma_{x,x} & \sigma_{x,y} & \sigma_{x,z} \\ \sigma_{y,x} & \sigma_{y,y} & \sigma_{y,z} \\ \sigma_{z,x} & \sigma_{z,y} & \sigma_{z,z} \end{pmatrix} \tag{75}$$

For a specific crystallite orientation the frequency resulting from $\mathbf{B}_{induced}$ can be given by:

$$\omega_{i,i} = \gamma \sigma_{i,i} B_0 \tag{76}$$

This can now be converted into a chemical shift ($\delta_{i,i}$) using the following definition:

$$\delta_{i,i} = \frac{\omega_{i,i} - \omega_{ref}}{\omega_{ref}} \tag{77}$$

Equation 77 can then be used to construct the chemical shift tensor as shown below:

$$\delta = \begin{pmatrix} \delta_{x,x} & \delta_{x,y} & \delta_{x,z} \\ \delta_{y,x} & \delta_{y,y} & \delta_{y,z} \\ \delta_{z,x} & \delta_{z,y} & \delta_{z,z} \end{pmatrix} \tag{78}$$

The chemical shift tensor is currently being represented in the laboratory frame and it is much easier to work with in the diagonalized form.

The diagonalized form of the chemical shift tensor ($\boldsymbol{\delta}^{PAS}$) is represented in the principal axis system (PAS), where the transformation into this frame is given by the following rotation:

$$\boldsymbol{\delta} = \mathbf{u}^{-1}\boldsymbol{\delta}^{PAS}\mathbf{u} \tag{79}$$

$$\textit{where} \quad \boldsymbol{\delta}^{PAS} = \begin{pmatrix} \delta_{XX}^{PAS} & 0 & 0 \\ 0 & \delta_{YY}^{PAS} & 0 \\ 0 & 0 & \delta_{ZZ}^{PAS} \end{pmatrix} \tag{80}$$

The diagonal components of $\boldsymbol{\delta}^{PAS}$ are known as the principal components and they correspond to the eigenvalues of the system, while the eigenvectors ($\mathbf{u}$) represent the corresponding rotation that relates the PAS frame ($\boldsymbol{\delta}^{PAS}$) tensor to the original laboratory frame tensor ($\boldsymbol{\delta}$).

If all three principal components of the chemical shift tensor in the PAS frame are equal then the Larmor frequency is independent of orientation and is characterized by the isotropic chemical shift as given by equation 81.

$$\delta_{iso} = \frac{\left(\delta_{XX}^{PAS} + \delta_{YY}^{PAS} + \delta_{ZZ}^{PAS}\right)}{3} \tag{81}$$

However, if all three components are not equal the Larmor frequency is now dependent on orientation and this dependency needs to be characterized by additional parameters. There are many different conventions that can be used to describe this dependence; however, this text will use the convention presented by Ulrich Haeberlen.[31]

The three principal components of the chemical shift tensor in the PAS are assigned by the following rules:

1. The δ_{ZZ}^{PAS} component is chosen such that it is the eigenvalue that is the furthest from δ_{iso}.

2. The δ_{YY}^{PAS} component is chosen such that it is the eigenvalue closest to δ_{iso}.

3. The remaining eigenvalue is assigned to the δ_{XX}^{PAS} component.

Based on the above convention, the chemical shift anisotropy (CSA) can be defined by finding the largest deviation from the isotropic value.

$$\delta_{aniso} = \delta_{ZZ}^{PAS} - \delta_{iso} \tag{82}$$

The difference between the other two principle components, δ_{XX}^{PAS} and δ_{YY}^{PAS}, represents the asymmetry (η) of the chemical shift tensor as given by:

$$\eta = \frac{\delta_{YY}^{PAS} - \delta_{XX}^{PAS}}{\delta_{aniso}} \tag{83}$$

Recall that the induced magnetic field caused by electron circulation depends on the molecules' orientation with respect to the static magnetic field and this dependency effects how the Fourier transformed spectrum, which is a function of frequency, will appear.

In solution-state NMR the sample is undergoing rapid molecular motion and as a result the averaged chemical shift tensor becomes isotropic, leaving only a single peak located at the isotropic shift of the sample as seen in figure 15a. Solid-state NMR experiments are carried out on powder samples which lack the rapid molecular motion seen in solution samples. Therefore, these samples contain multiple different crystal orientations of the sample with respect to the magnetic field. As a result, each crystal orientation of the powder has a slightly different shift and the addition of each of these

various shifts leads to what is known as a powder pattern, which is shown in figure 15b. The sharp features, or inflection points, in the powder pattern correspond to the principal components of the chemical shift tensor in the PAS frame of reference, while the shape of the pattern depends upon the value of both the CSA and asymmetry terms. A second example of a powder pattern with slightly different CSA and asymmetry values can be seen in figure 15c. In this case, rapid motion along one of the axis causes the two principal components (δ_{XX}^{PAS} and δ_{YY}^{PAS}) to be equivalent and results in a tensor that is cylindrically symmetric. There is a solid-state NMR method, known as magic angle spinning (MAS), that is designed to reduce the line broadening caused by the CSA and this method will be discussed later.

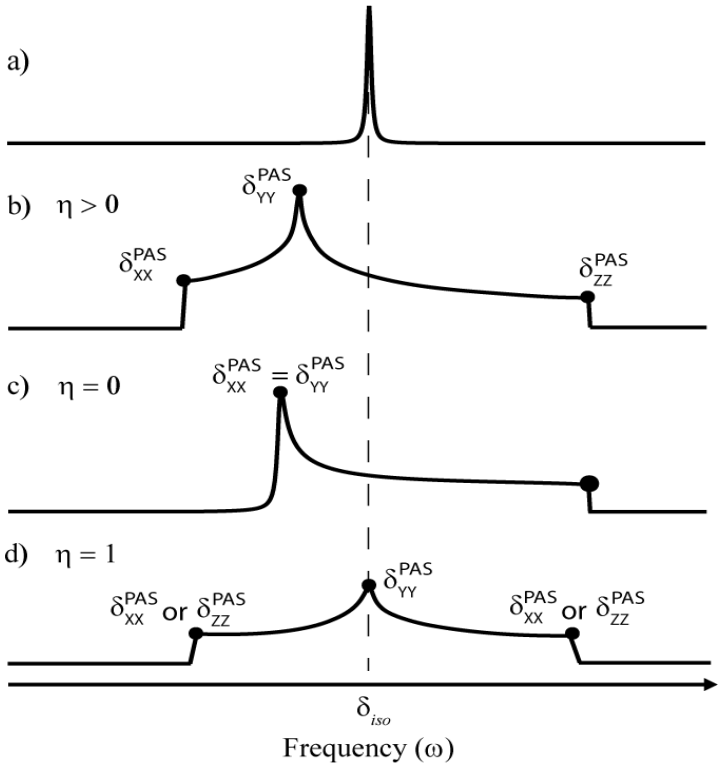

Figure 15 The broadening effect in NMR spectra of solids caused by the CSA interaction. a) The spectrum obtained as a result of fast isotropic motion; b) the powder pattern observed in the case of the asymmetry parameter being greater than zero; c) the powder pattern obtained in the case of the asymmetry parameter being equal to zero (axial symmetry); d) the powder pattern observed in the case of the asymmetry parameter equal to one. [13]

II. Dipolar Coupling

Earlier, when discussing relaxation, it was mentioned that spins are not necessarily isolated from one another. In fact, the magnetic field produced by a nearby spin can interact with the magnetic moment of another spin. This interaction is known as the direct dipole-dipole coupling, or more simply dipolar coupling. In solution-state NMR experiments this interaction is averaged to zero because the matrix which describes the interaction is traceless. However, in the solid state the effects of dipolar coupling are not averaged and can be a major source of line broadening in the spectrum.

The dipolar interaction of two spins can be derived from the classical form for the energy of interaction, or potential, between two magnetic dipoles separated by a distance r [19]:

$$V = \left\{ \frac{\boldsymbol{\mu}_1 \cdot \boldsymbol{\mu}_2}{r^3} - 3\frac{(\boldsymbol{\mu}_1 \cdot \mathbf{r})(\boldsymbol{\mu}_2 \cdot \mathbf{r})}{r^3} \right\} \frac{\mu_0}{4\pi} \tag{84}$$

The vector $\mathbf{r}$ is the vector between the two magnetic dipoles. The quantum mechanical operator for the magnetic moment of spin I_j can be given by equation 85.

$$\hat{\boldsymbol{\mu}} = \gamma \hbar \hat{\mathbf{I}}_j \tag{85}$$

If each magnetic dipole is treated as a spin we can substitute equation 85 into equation 84 and obtain the Hamiltonian for the dipolar interaction between two spins *j* and *k.*

$$\widehat{H}_{j,k}^{Dip} = -\left(\frac{\mu_0}{4\pi}\right)\gamma_j \gamma_k \hbar \left(\frac{\mathbf{I}_j \cdot \mathbf{S}_k}{r^3} - 3\frac{\left(\mathbf{I}_j \cdot \mathbf{r}\right)\left(\mathbf{S}_k \cdot \mathbf{r}\right)}{r^5} \right) \tag{86}$$

Note that spins *j* and *k* are represented by the angular momentum operators I and S, respectively, and this indicates that the interacting spins can be any two nuclei. The dipolar interactions represented by equation 86 can be expressed in spherical polar coordinates as seen in figure 16, where θ is the polar angle and ϕ is the azimuthal angle.

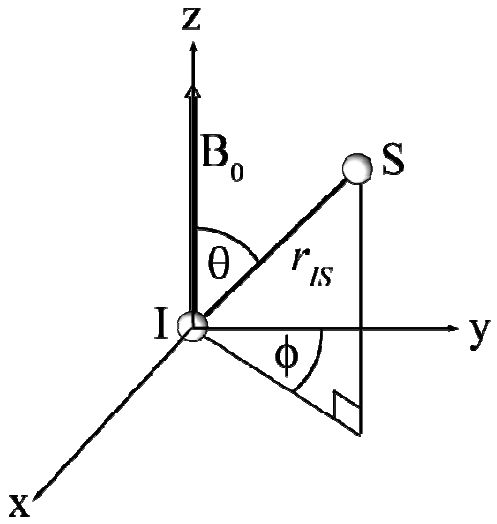

Figure 16 A vector representation of the direct dipolar coupling between two spins in the presence of a static magnetic field using the spherical polar coordinate system.

In this form the scalar products can be evaluated and result in the following form of the Hamiltonian for dipolar coupling:

$$\widehat{H}_{j,k}^{Dip} = -\left(\frac{\mu_0}{4\pi}\right)\frac{\gamma_j\gamma_k\hbar}{r^3}\left[A+B+C+D+E+F\right] \qquad (87)$$

Where:

$$
\begin{aligned}
A &= \widehat{I}_z \widehat{S}_z \left(3\cos^2\theta - 1\right) \\
B &= -\frac{1}{4}\left[\widehat{I}_+ \widehat{S}_- + \widehat{I}_- \widehat{S}_+\right]\left(3\cos^2\theta - 1\right) \\
C &= -\frac{3}{2}\left[\widehat{I}_z \widehat{S}_+ + \widehat{I}_+ \widehat{S}_z\right]\sin\theta\cos\theta e^{-i\theta} \\
D &= -\frac{3}{2}\left[\widehat{I}_z \widehat{S}_- + \widehat{I}_- \widehat{S}_z\right]\sin\theta\cos\theta e^{+i\theta} \\
E &= -\frac{3}{4}\left[\widehat{I}_+ \widehat{S}_+\right]\sin^2\theta e^{-2i\theta} \\
F &= -\frac{3}{4}\left[\widehat{I}_- \widehat{S}_-\right]\sin^2\theta e^{+2i\theta}
\end{aligned}
\tag{88}
$$

The A, B, C, D, E, and F terms comprise what is known as the dipolar alphabet. It can be shown that the energy transitions resulting from the last four terms in the alphabet (C, D, E, and F) have very little effect on the spin system and, according to the secular approximation, will be dropped from this point forward.[14] The B term of the alphabet is currently represented in terms of the raising and lowering angular momentum operators and must be re-expressed in terms of the Cartesian angular momentum operators, as shown in equation 89.

$$
B = -\frac{1}{2}\left[\widehat{I}_x \widehat{S}_x + \widehat{I}_y \widehat{S}_y\right]\left(3\cos^2\theta - 1\right) \tag{89}
$$

The effect of the dipolar Hamiltonian can be considered in two separate cases, that of homo-nuclear and hetero-nuclear dipolar couplings.

In the case of Homo-nuclear dipolar couplings, both the A and B terms are present and result in the following Hamiltonian:

$$
\widehat{H}_{j,k}^{dip} = d_{j,k}\frac{1}{2}\left(3\cos^2\theta - 1\right)\left(3\hat{I}_{j,z}\hat{I}_{k,z} - \hat{\mathbf{I}}_j \cdot \hat{\mathbf{I}}_k\right) \tag{90}
$$

The constant d_{jk} is known as the dipolar coupling constant and is given by:

$$d_{jk} = -\frac{\mu_0}{4\pi}\frac{\gamma_j \gamma_k \hbar}{r_{j,k}^3} \tag{91}$$

Note that both spins *j* and *k* are now being represented by the angular momentum operator (**I**); therefore the spin index has been re-introduced to the operators. The homo-nuclear dipolar coupling, in the case of a multiple spin system, results in a line broadening effect that can be seen in figure 17 and this can be attributed to the B term of the dipolar alphabet.[15]

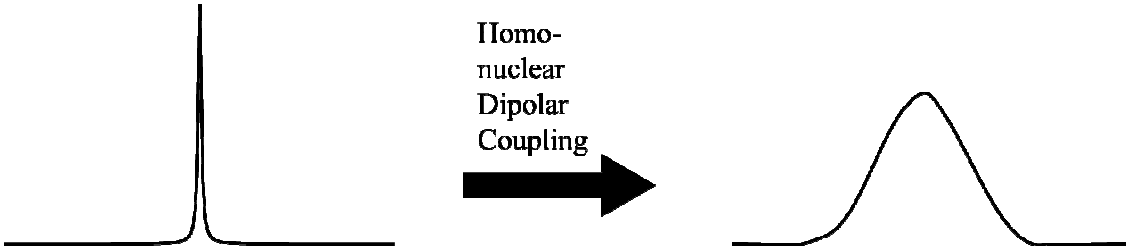

Figure 17 The effect of homo-nuclear dipolar couplings on the observed NMR spectrum.[32]

This line broadening is quite prominent in spin systems that have a high natural abundance and a large gyromagnetic ratio, such as the ^{19}F and ^{1}H isotopes, and can result in a line width on the order of several kHz. Spin systems that have either a low natural abundance or gyromagnetic ratio will not experience strong homo-nuclear dipolar couplings and in these cases only the effect of hetero-nuclear dipolar coupling needs to be considered.

The hetero-nuclear dipolar Hamiltonian contains only the A term of the alphabet and is given by the following:

$$\widehat{H}_{jk}^{dip} = d_{jk}\frac{1}{2}\left(3\cos^2\theta - 1\right)\left(2\hat{I}_z\hat{S}_z\right) \tag{92}$$

The B term of the alphabet disappears because it contains a transverse term, known as the flip flop term ($\hat{I}_x\hat{S}_x + \hat{I}_y\hat{S}_y$), that is only significant when the Larmor frequency of spin *I* and *S* are equivalent; therefore the line broadening due to the B term will no longer be present. In this case the hetero-nuclear dipolar couplings lead to a Pake pattern,[33] shown in figure 18, where the separation between the most intense features of the pattern (known as the horns) is given by the dipolar coupling constant (d_{jk}).

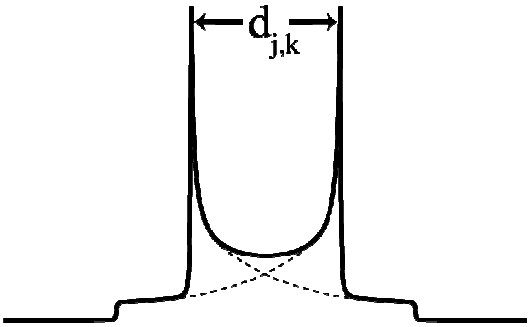

Figure 18 NMR spectrum of a Pake pattern resulting from the hetero-nuclear dipolar coupling of an isolated spin pair.

Each side of the pake pattern corresponds to a powder pattern similar to the one shown for the chemical shift anisotropy with axial symmetry ($\eta = 0$). This is because the dipolar couplings cause a shift in the transition frequency of each nuclei involved in the coupling that has an orientation dependency given by: $3\cos^2\theta - 1$. However, the dipolar couplings cause both a positive and negative shift, where both shifts are equal in magnitude. This results in the superposition of two symmetric powder patterns, as seen in figure 18. It is important to note that the homo-nuclear dipolar couplings for a spin system containing four or less spin pairs results in a Pake pattern similar to the one shown in figure 18; however, in this case the splitting between the horns is given by 3/2 d_{jk}.[34]

III. J-Coupling

Earlier it was mentioned that the direct spin-spin coupling tensor (dipolar coupling) is traceless and therefore averages to zero in solution-state NMR experiments. Indirect spin-spin coupling, better known as J-coupling, is present in solution state NMR and is mediated through the electron density of the sample. The J-coupling is given by the following Hamiltonian:

$$\widehat{H}^{J}_{j,k} = 2\pi \hat{\mathbf{I}}_j \cdot \hat{\mathbf{J}}_{j,k} \cdot \hat{\mathbf{I}}_k \tag{93}$$

The 2π term is present because the J-coupling is generally specified in hertz and the $\hat{J}_{j,k}$ term is the J-coupling tensor given by:

$$\hat{\mathbf{J}}_{j,k} = \begin{pmatrix} J^{jk}_{xx} & J^{jk}_{xy} & J^{jk}_{xz} \\ J^{jk}_{yx} & J^{jk}_{yy} & J^{jk}_{yz} \\ J^{jk}_{zx} & J^{jk}_{zy} & J^{jk}_{zz} \end{pmatrix} \tag{94}$$

The J-coupling interaction is isotropic in solution and results in the multiplet structures commonly seen in solution-state NMR spectroscopy. These structures depend on the scalar coupling, or isotropic J-coupling, the value of which is specified by:

$$\widehat{H}^{J,iso}_{j,k} = 2\pi J_{j,k} \hat{\mathbf{I}}_j \cdot \hat{\mathbf{I}}_k = 2\pi J_{j,k} (\hat{I}_{j,x} \hat{I}_{k,x} + \hat{I}_{j,y} \hat{I}_{k,y} + \hat{I}_{j,z} \hat{I}_{k,z}) \tag{95}$$

Where:

$$J_{j,k} = \frac{1}{3} (J^{j,k}_{xx} + J^{j,k}_{yy} + J^{j,k}_{zz}) \tag{96}$$

These multiplet structures provide direct information about the bonding geometry of the system. It is important to point out that J-coupling is also present in solids and can be anisotropic; however, J-coupling in solids will not be discussed any further in this work.

IV. Quadrupolar Coupling

To this point only the very specific case of spin ½ has been discussed. Nuclei with a spin greater than ½, referred to as quadrupolar nuclei, possess an electric quadrupole moment. This quadrupole moment interacts with the electric field gradient (EFG) of the nucleus created by the surrounding electron density. The orientation of the electric field gradient with respect to the static magnetic field can be represented by a tensor, in a similar manner to the CSA, and also has a corresponding PAS frame. The quadrupolar interaction causes a large shift in the Larmor frequency and results in a powder pattern that is very similar to the Pake patterns, as seen for the hetero-nuclear dipolar couplings. These powder patterns cover a range of frequencies that is much larger than those due to hetero-nuclear dipolar couplings and are on the order of tens of kHz to several MHz wide. For this reason, the study of quadrupolar nuclei is a rather large and very specialized sub-discipline of NMR spectroscopy.[35] The quadrupolar interaction is beyond the scope of this work and will not be discussed any further.

1.3.4 Overall NMR Hamiltonian in Solution- vs. Solid-state

The spectra in solution-state and solid-state NMR (SSNMR) spectroscopy are quite different because the internal interactions present in the overall Hamiltonian differ in each case. In solution-state NMR spectroscopy isotropic motion averages the dipolar interaction to zero, as well as any anisotropy in the chemical shift tensor, and leaves only the isotropic chemical shift and J-coupling to dominate the internal interactions. Therefore, high resolution is easily obtained in solution-state NMR spectroscopy and is characterized by narrow line widths and well resolved multiplet structures. In the solid-

state both the dipolar interaction and chemical shift anisotropy are present in the Hamiltonian and lead to significant line broadening, as indicated in the dipolar coupling and chemical shift sections above. For this reason many specialized techniques have been developed in the solid-state in order to reduce the line broadening caused by CSA and dipolar coupling interactions.

1.4 Specialized NMR Techniques

There are numerous specialized techniques employed in the SSNMR experiments presented in chapters 2 and 3. These have been developed to improve the quality of solid state NMR spectroscopy by increasing the resolution and signal to noise ratio of spectra. The next section will explain the theory and principles behind some of these common methods.

1.4.1 Magic-Angle Spinning

Earlier it was mentioned that SSNMR spectroscopy is carried out on powder samples which contain multiple crystal orientations with respect to the static magnetic field. Each crystal orientation gives rise to a slightly different chemical shift and the superposition of these shifts gives rise to a powder pattern. This powder pattern appears again in the form of a Pake pattern when considering the effect of hetero-nuclear dipolar couplings (see figure18). Both the CSA and hetero-nuclear dipolar coupling Hamiltonians contain a dominant leading term that defines the orientation of the interaction with respect to the static magnetic field and this is given by:

$$3\cos^2\theta - 1 \tag{97}$$

In fact, it can be shown that all of the internal interactions of the Hamiltonian with a non-isotropic tensor contain a dominant leading term equivalent to equation 94.[31] The line broadening effects of these terms in the Hamiltonian can be removed if each crystallite could be placed at an angle θ_m with respect to the static field, where θ_m is chosen such that equation 97 is equal to zero. This specific angle is known as the magic angle and is given by:

$$\theta_m = \arccos\frac{1}{\sqrt{3}} \cong 54.74° \tag{98}$$

After the sample is placed at the magic angle it is spun about this angle at a speed given by ν_r. This rotation mimics the isotropic motion seen in solution-state NMR by equally sampling all of the directions of motion (x, y, and z). The act of spinning a sample about the magic angle, as illustrated in figure 19, is referred to as magic angle spinning (MAS).

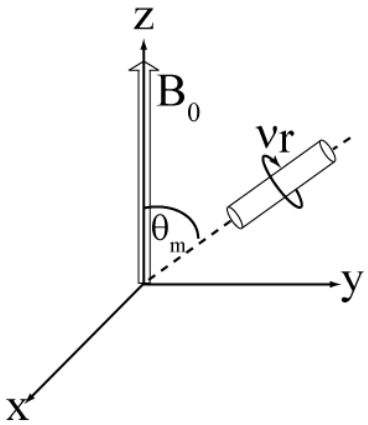

Figure 19 Schematic representation of sample rotation at the magic angle.

The sample spinning speed (ν_r) determines how efficiently each term in the Hamiltonian will be suppressed. The CSA and hetero-nuclear dipolar couplings can be

removed by using spinning speeds slightly larger than the interaction strength and results in an isotropic line as seen in figure 20a.[36-38] When the spinning speed is less than the interaction strength of the Hamiltonian the orientation dependence is not completely removed. The incomplete removal of the CSA and hetero-nuclear dipolar terms results in a spinning side band pattern like the one shown in figure 20b. The observed sideband pattern resembles the powder pattern (figure 20c) that is acquired without the use of MAS and can be directly related to the remaining chemical shift anisotropy tensor. It is important to note that the isotropic peak is not necessarily the most intense line; however the isotropic peak will not shift with spinning speed and can be easily identified by carrying out the same experiment at two different speeds.

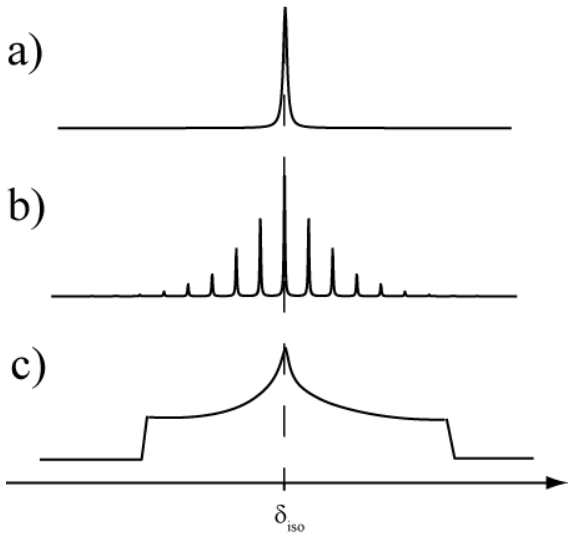

Figure 20 MAS NMR spectrum obtained at a spinning speed larger than (a) and smaller than (b) the line broadening interaction; MAS NMR spectrum obtained under static conditions (c).

The homo-nuclear dipolar couplings give rise to a line broadening that can also be reduced, or removed, by the use of MAS; however, not quite as easily as the aforementioned interactions. Nuclei with high natural abundance and a large

gyromagnetic ratio possess rather large homo-nuclear couplings and as a result spinning speeds in the range of 30-75 kHz are required to remove these interactions. Recently, NMR probes capable of reaching these speeds have become available and this has resulted in the development of new fast spinning techniques for obtaining high resolution spectra.[39]

The spinning of a sample at the magic angle results in a phenomenon known as the rotational echo. Recall that the FID is detected in real-time and contains an evolution term defined by the static field, chemical shift anisotropy, and dipolar coupling. As the sample is spun, each crystallite undergoes multiple different orientations with respect to the magnetic field; therefore, the evolutionary frequency of the FID will reflect these orientations. As the sample completes one full rotation the frequency of evolution will return to its starting value and then undergo the cycle again. As a result, the FID will be composed of a sequence of repeating patterns known as rotational-echoes (figure 21).

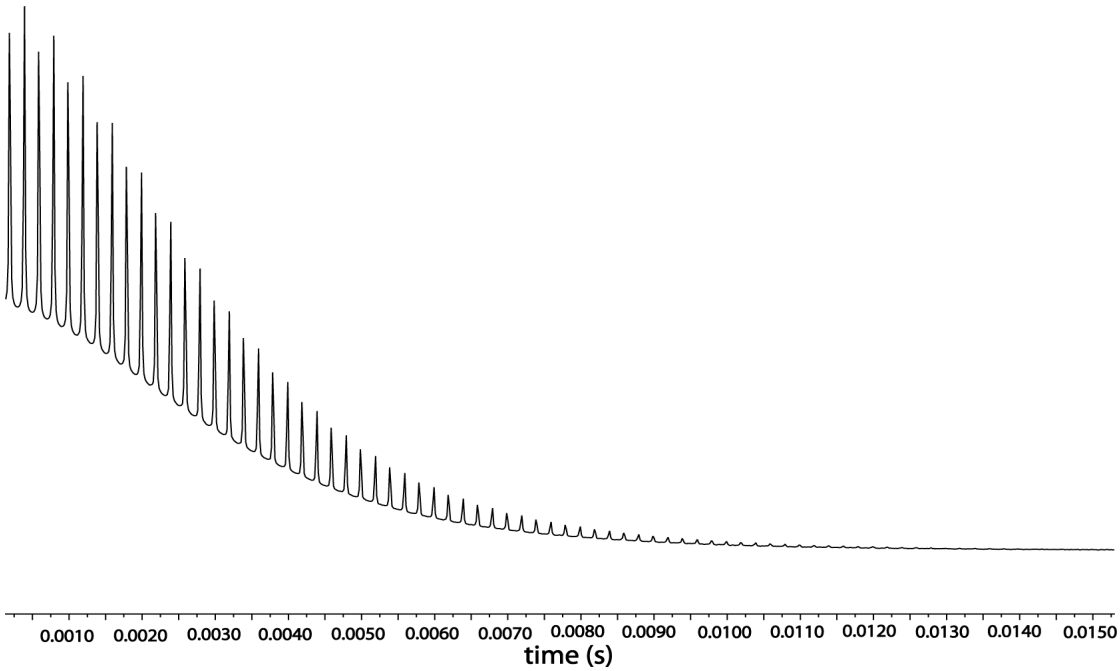

Figure 21 The ^{79}Br FID of KBr spinning at an MAS rate of 5 kHz.

A time series that is composed of only the maximum value of each rotor echo will result in an isotropic spectrum as seen in figure 20a; therefore it is important to consider the effect of synchronizing the acquisition period of a pulse sequence with the rotor period of MAS (rotor-synchronization). The rotor period (τ_r) of MAS can be defined by the following:

$$\tau_r = \frac{1}{\nu_r} \tag{99}$$

The effects of rotor-synchronization on a pulse sequence will be explored further in chapters 2 and 3.

1.4.2 Decoupling

Magic angle spinning is a useful way to remove the line broadening effects of the CSA and dipolar terms in the Hamiltonian. However, MAS may not completely remove hetero-nuclear dipolar couplings and in these cases MAS is combined with a technique known as decoupling.[40] Decoupling is commonly used in both solution- and solid-state NMR spectroscopy to remove any hetero-nuclear couplings that are present, including J-coupling. Multiple different decoupling schemes have been developed and each is tailored towards the specific requirements of a particular NMR experiment and spectrometer.

The most basic form of decoupling is known as continuous wave (CW) decoupling and consists of the application of continuous RF irradiation to a hetero-nucleus during acquisition (see figure 22).

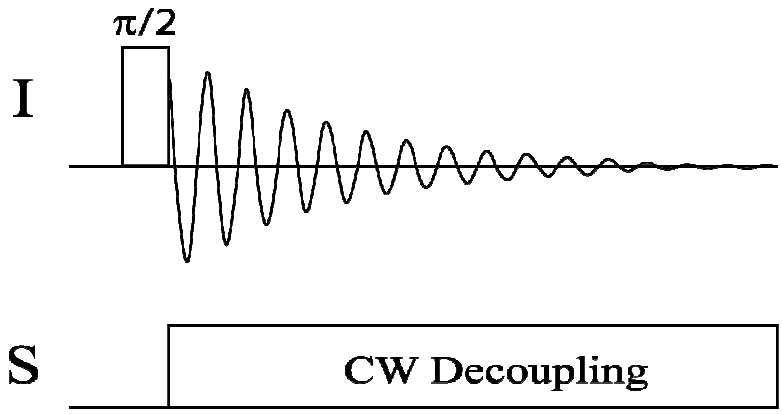

Figure 22 The basic continuous wave (CW) decoupling sequence.

However, this technique is limited because the RF irradiation must remain on throughout the entire acquisition period and this restricts the strength of the RF field used. This restriction corresponds to a limit in the frequency range over which the decoupling is effective. This is not a problem for decoupling nuclei that have a very small chemical shift range, such as the ^{1}H nuclei, but is when attempting to decouple the effect of nuclei with a large chemical shift range, such as the ^{13}C and ^{19}F nuclei. More specialized decoupling techniques have been developed to deal with the situation of decoupling nuclei with large chemical shift ranges.

The most common modification of CW decoupling is known as two pulse phase modulated (TPPM) decoupling.[41] TPPM is still a form of continuous decoupling but alters the basic CW scheme by applying a series of back to back RF pulses. Each pulse is applied for an entire rotor period and has the opposite phase of the previous pulse, as shown in figure 23.

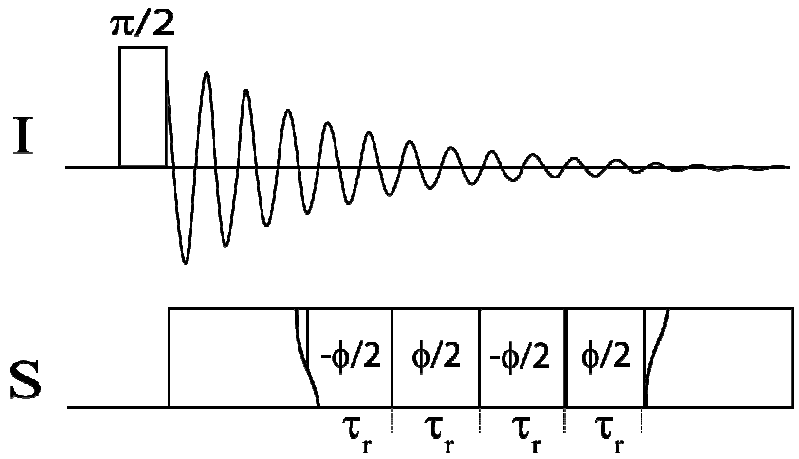

Figure 23 The TPPM decoupling sequence.

This phase alternating scheme is designed to increase the effective frequency range over which the CW decoupling occurs, and therefore increases decoupling performance. There are many modifications of TPPM decoupling,[42-47] but the most common one employs a phase shift where the two pulses are exactly 180 degrees out of phase with each other and is known as X inverse-X (XiX) decoupling.[48] TPPM and its numerous modifications greatly increase the efficiency of decoupling; however, a multiple-pulse decoupling sequence, where the RF pulses no longer remain on for the entire duration of the acquisition period, would allow for the use of much higher RF powers.

The use of multiple-pulse decoupling has been around for a long time in solution-state NMR spectroscopy and was originally used in solid-state NMR to decouple the homo-nuclear dipolar interaction.[31-32] One of the more specialized multiple-pulse decoupling schemes used in solid-state NMR is the XY-16 sequence (figure 24) and it is designed to decouple nuclei with a very large chemical shift anisotropy.[49]

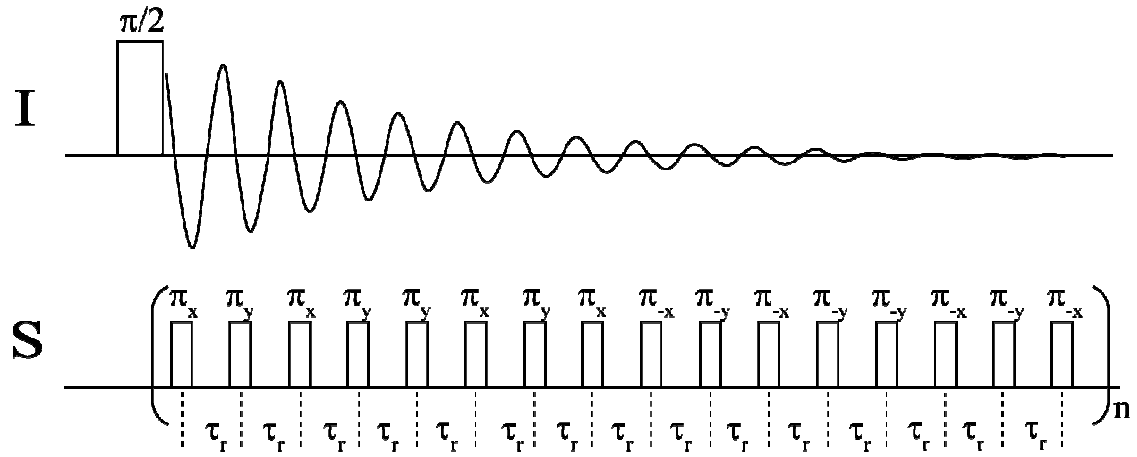

Figure 24 The XY-16 decoupling sequence.

This sequence consists of a train of 16 individual rotor-synchronized 180 degree pulses with each pulse having a phase (ϕ) that follows the XY-16 phase cycle.[50] The term rotor-synchronized implies that each pulse is applied at the end of a rotor period (τ_r). This decoupling scheme does not require continuous RF irradiation and therefore permits the use of much stronger RF powers. These powers can be anywhere from 100 to 125 kHz and allow for the decoupling of nuclei over a chemical shift range of the same order. More advanced multiple-pulse decoupling schemes based on symmetry principles have been developed and allow for the selective removal or re-introduction of specific terms in the Hamiltonian. These sequences, known as C or R sequences, not only allow the user to control which terms of the Hamiltonian will be decoupled during acquisition, but also allow for the re-introduction of terms which have been removed by MAS.[51-58]

1.4.3 The Hahn Echo

The presence of a large CSA and dipolar coupling can cause the FID to dephase very rapidly; therefore, the FID must be detected as quickly as possible after the excitation pulse has been applied. This is not always possible due to distortions caused by turning off the excitation pulse (pulse ring-down effects).[21] In this case it is ideal to have a method capable of letting one observe the magnetization created directly after a pulse without having to detect the FID immediately after the pulse. This can be achieved by using a common technique known as the Hahn-echo.

Figure 25a gives the pulse sequence for a Hahn-echo while figure 25b indicates the state of the magnetization after each step in the sequence. The initial transverse magnetization is created by a 90 degree pulse and then begins to lose coherence, or fan out in the transverse plane, during a fixed interval of time (τ). This is caused by small fluctuations in the local magnetic field experienced by a spin and as a direct result some spins experience a slightly larger field while others experience a slightly smaller field. Therefore, some of the spins will precess more quickly and others less so, both with respect to the Larmor frequency. The application of a 180 degree pulse reverses the placement of the magnetization in the transverse plane such that the components with slightly faster precession are now behind the rotating frame and the ones with slightly slower precession are ahead of the frame. After the second delay period, also equal to τ, the spins have refocused in the transverse plane and return to a state that is almost identical to the original excited state. The magnetization can now be detected without having to worry about the effects of pulse ring down.

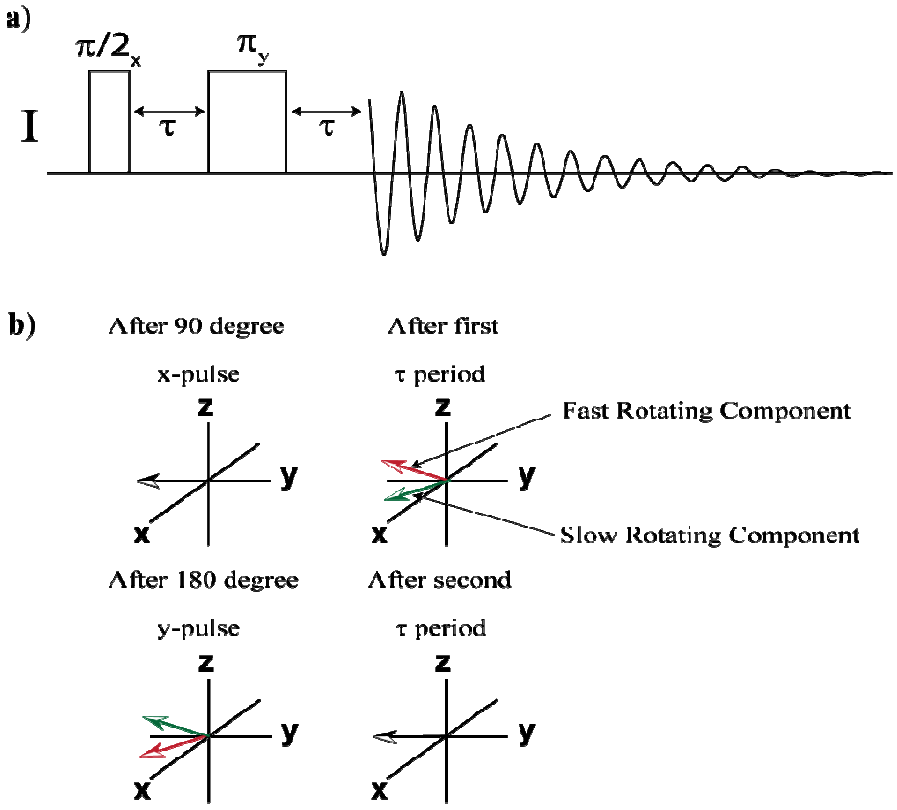

Figure 25 a) The pulse sequence for the Hahn-echo; b) a magnetization diagram illustrating the state of the magnetization throughout various steps of the Hahn-echo.

The efficiency of the Hahn-echo relies on carefully setting both the 90 and 180 degree pulses such that the magnetization is accurately refocused. When either the 90 or 180 degree pulse is not carefully set it can result in residual incoherent, or non-refocused, transverse magnetization which leads to phase distortions in the observed spectrum. This problem can be circumvented by running the sequence more that once with the phase of the 90 and 180 degree pulses varied in each successive run (known as a phase cycle). A very specific phase cycling method, known as an EXORCYCLE, can be implemented and makes the Hahn-echo far less sensitive to errors in the setting of both the 90 and 180 degree pulses.[59] The EXORCYLE phase cycle requires 16 steps and is given in table 1.

Table 1 Phase cycle of EXORCYCLE

$\pi/2_\phi$	π_ϕ	$\pi/2_\phi$	π_ϕ
X	Y	Y	Y
X	(-Y)	Y	(-Y)
X	X	Y	X
X	(-X)	Y	(-X)
(-X)	X	(-Y)	Y
(-X)	(-X)	(-Y)	(-Y)
(-X)	Y	(-Y)	X
(-X)	(-Y)	(-Y)	(-X)

EXORCYCLE ensures that any of the remaining incoherent transverse magnetization is produced equally in all directions and will therefore cancel out by co-adding all 16 spectra. The use of EXORCYCLE will be revisited when discussing the results presented in Chapter 3.

1.4.4 Cross-Polarization

The NMR signal of dilute spins, or spins with low natural abundance and receptivity, can be very hard to detect because the NMR signal has a very low signal to noise ratio. This problem can be circumvented by carrying out multiple scans, or transients, of the same experiment. The time between these transients, known as the recycle delay, is dependent on T_1. Dilute spins tend to have very long T_1 values, making the acquisition of multiple scans a lengthy process. Cross-polarization (CP) is a method in which dilute spins can use a nearby ensemble of abundant nuclei to enhance their spin polarization. Polarization transfer during CP relies upon a spin-lock, where the maximum length of this lock is dependent upon a parameter known as the spin-lattice relaxation in

the rotating frame ($T_{1\rho}$).[16, 32] Both the effect of the spin-lock and the $T_{1\rho}$ parameter will be explained in the following text.

The $T_{1\rho}$ parameter is measured by placing the static magnetization into the transverse plane with a 90 degree pulse and then locking it in the plane with a spin-lock (figure 26a).

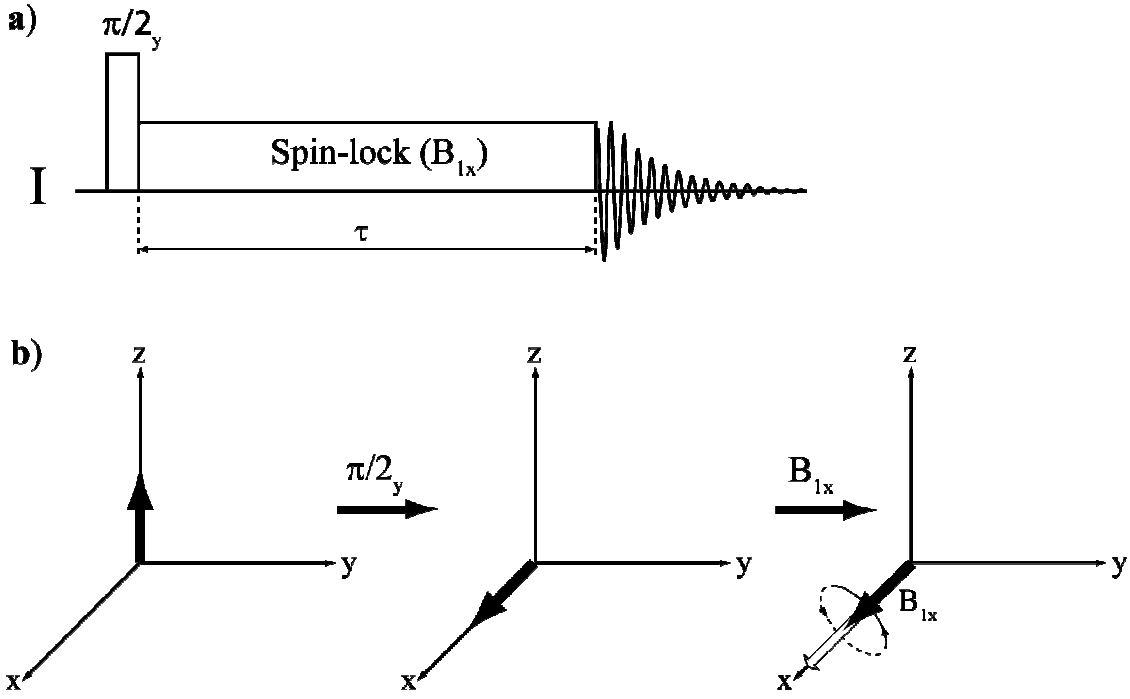

Figure 26 a) The pulse sequence for a spin-lock experiment; b) a magnetization diagram illustrating the state of the magnetization throughout various steps of the spin-lock sequence.

The spin-lock is a low power pulse applied along the plane that coincides with the transverse magnetization and remains on for a time τ. Figure 26b shows a magnetization diagram which illustrates the effect of both the initial 90 degree y-pulse and the subsequent spin-lock. If the power of the spin-lock is sufficient it will cause the magnetization to remain along the x-axis where it will precess according to the frequency

of the applied pulse. Therefore, the magnetization will decay during the spin-lock on a time scale determined by the power of the locking pulse and not the Larmor frequency. This decay is determined by both the length of the spin-lock and $T_{1\rho}$ as given by:

$$M_x = M_0 e^{-\frac{\tau}{T_{1\rho}}} \tag{100}$$

After the spin-lock is turned off the magnetization is free to precess and decay according to the Larmor frequency and transverse relaxation (T_2), respectively. The value of $T_{1\rho}$ can be easily obtained by repeating this experiment multiple times, each with different spin-lock times. It is important to note that the value of $T_{1\rho}$ is usually on the millisecond time-scale and allows for the probing of motion and dynamics on this scale. Now that the spin-lock and $T_{1\rho}$ have been introduced the basic CP experiment can be presented and explained.

The polarization transfer that occurs during CP (figure 27) is dependent upon two main factors: the contact time (τ_{cntct}) and the Hartmann-Hahn match.

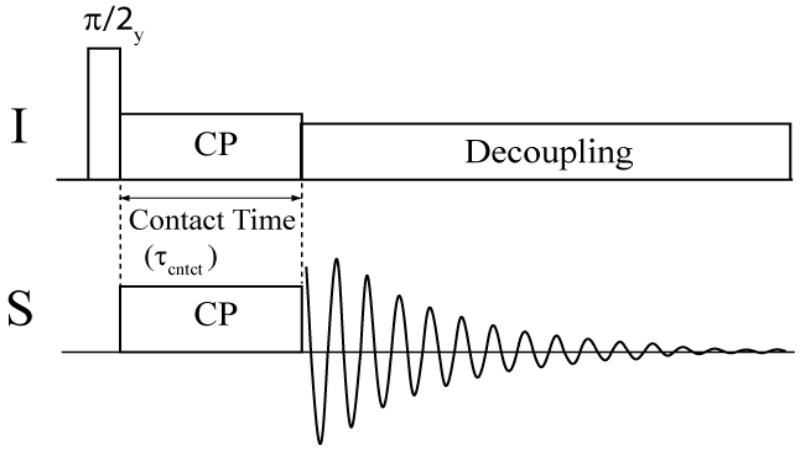

Figure 27 The pulse sequence for cross-polarization.

Recall that the hetero-nuclear dipolar interaction does not contain the B term (flip-flop term) of the dipolar alphabet because the Larmor frequencies of the spins involved are quite different. During a spin-lock period the frequency of precession is determined by the applied RF power of the lock and not the Larmor frequency of the spins. This means that the RF powers of a spin lock applied to both nuclei simultaneously can be manipulated in order to equalize the following equation:

$$\omega_I = \gamma_I B_{1,I} = \gamma_S B_{1,S} = \omega_S \tag{101}$$

Now that the frequencies of spin I and S are equivalent the flip-flop term is re-introduced to the hetero-nuclear dipolar Hamiltonian, which allows for the exchange of magnetization between the two spins. The condition given in equation 101 is known as the Hartmann-Hahn match.[60] Hence, magnetization can be created on an abundant spin (*I*), with a 90 degree excitation pulse, and effectively transferred to the dilute spin (*S*), via a simultaneous spin-lock on both channels, for subsequent detection.

The polarization transfer during the spin-lock can be further explained by examining the Hamiltonian in the presence and absence of a spin-lock. Prior to the spin-lock period the Hamiltonian consists of the Zeeman term of each nucleus and the A term of the hetero-nuclear dipolar interaction, as given by:

$$\widehat{H} = H_i^Z + H_j^Z + H_{ij}^{Dip(A)} \tag{102}$$

During the spin-lock period the Zeeman term for each nucleus is no longer present in the Hamiltonian of the RF pulse and the magnetization is evolving according to the homo-nuclear dipolar Hamiltonian.

$$\widehat{H} = H_{ij}^{Dip(A+B)} \tag{103}$$

The rate of magnetization transfer between the spins depends on the average dipolar interaction between them. Therefore, the time over which the Hartmann-Hahn match occurs (contact time) must be carefully chosen so that this transfer is optimal (figure 28).

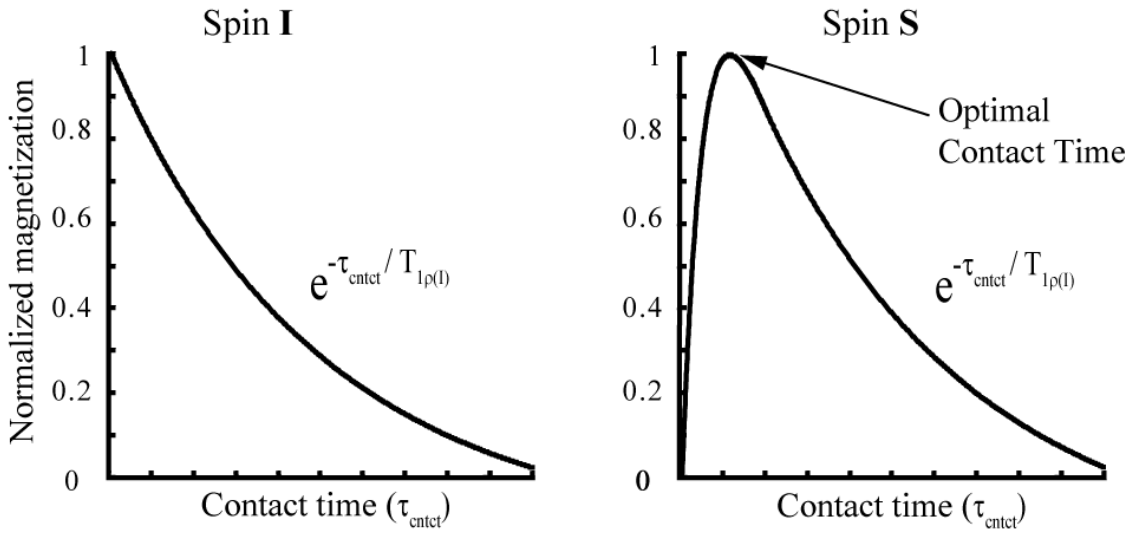

Figure 28 A general CP build up and decay curve for a transfer from an abundant spin **I** to a rare spin **S.**[18]

It is important to note that the magnetization decays in both channels at a rate governed by $T_{1\rho}$ of the abundant spin and as a result, the recycle delay of the experiment is also governed by the T_1 of the abundant spin. In general, an abundant spin has a much shorter T_1 than a dilute spin and this allows for the repetition of more experiments in less time. The combination of both effective polarization transfer via CP and a short recycle delay allows for the acquisition of high signal to noise spectra of dilute spins in much less time.

The signal-to-noise enhancement in a CP experiment can be considered in two cases: transfer between an abundant and dilute spin and the transfer between two abundant spins. The enhancement factor for the first case is directly related to the

difference between the gyromagnetic ratio of the two nuclei. In the latter case, the difference between the gyromagnetic ratios of each nucleus is very small and the enhancement now depends upon the ratio of the product of the gyromagnetic ratios and the relative populations of each spin.[61]

The Hartmann-Hahn match condition is very sensitive to fluctuations in both power and spinning speed and this leads to a loss in the efficiency of CP. For this reason many different forms of CP have been developed in order to increase its efficiency.[62-63] The above outlined method, known as constant CP, is the most sensitive form and is usually only employed when quantitative data is needed. Another form, known as ramped CP, varies the power on one of the channels in a linear fashion. This allows for a broader power range that can account for fluctuations in the match condition; however, longer contact times are usually required. Adiabatic CP is used for cases where fast MAS must be used and the dipolar interactions are scaled down. In this case, the power is varied such that the magnetization undergoes an adiabatic passageway[64] in which, for a period of time, the only term remaining in the Hamiltonian is the dipolar term and during this time the magnetization is effectively transferred between two nuclei.

1.4.5 Multi-dimensional NMR

All of the NMR experiments that have been presented up to this point are one-dimensional (1D) techniques where the detected signal is a function of only one time variable. This results in a spectrum that gives the signal intensity as a function of only one frequency axis as seen in figure 29.

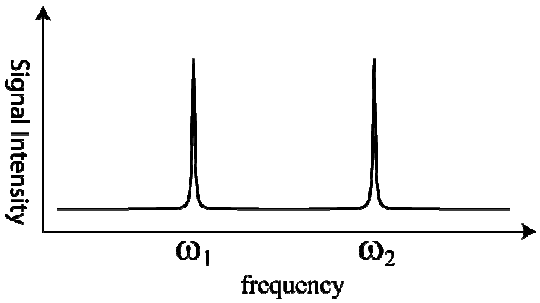

Figure 29 A 1D NMR spectra containing to isotropic lines.

In complex molecules a 1D spectrum can become very crowded, due to multiple chemical shifts, and difficult to interpret; therefore, it is difficult to extract information about the connectivity, or interactions, of the various spin networks. In multi-dimensional NMR spectroscopy the detected signal is a function of several time variables and this provides a tool for analyzing the connectivity of these complex systems.

In two-dimensional (2D) NMR spectroscopy[65-66] the signal is detected as a function of two time variables, thus providing a way to make observations of the spin-spin interactions directly. The general pulse sequence for a 2D NMR experiment is shown in figure 30 and is composed of four time periods known as preparation, evolution, mixing, and detection.

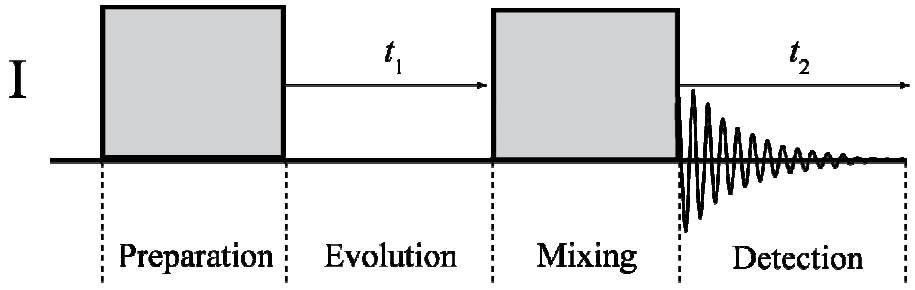

Figure 30 The general pulse sequence of a 2D NMR experiment.

The preparation period uses RF pulses to carefully manipulate the spin system and create a desired state, or coherence order, of the spin system. This state then evolves freely for

the duration of the evolution period (t_1). It is important to note that the magnetization is not directly detected during the evolution period. The mixing period then uses RF pulses to re-convert the state of the spin system to a form in which it can be detected during the detection period (t_2). The resulting FID is now a function of both the evolution (t_1) and detection (t_2) time periods. The application of a Fourier transform in both time variables results in a 2D spectrum (figure 31) that contains the signal as a function of frequency along two axes, F_1 and F_2, and these axes correspond to evolution during the time periods of t_1 and t_2, respectively.

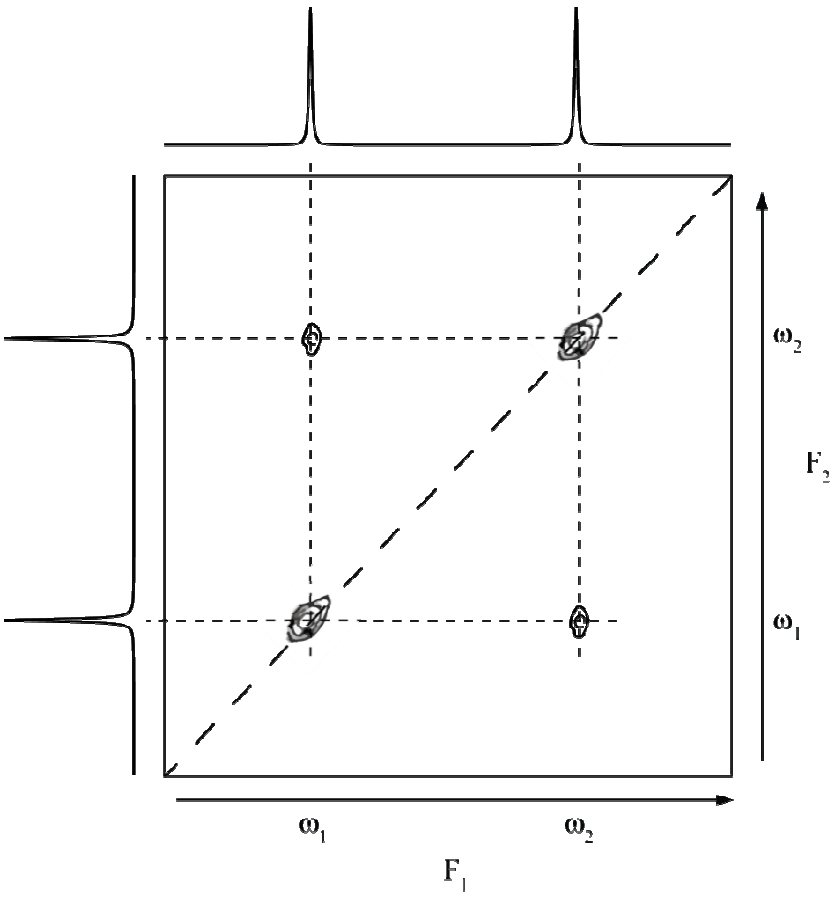

Figure 31 A general 2D NMR spectra.

The cross-peaks in figure 28 indicate correlations between spins due to coupling. Specific examples of 2D NMR techniques will be given later when discussing the application of SSNMR to polymers.

1.4.6 ^{19}F Solid-State NMR

Fluorine SSNMR is an ideal tool to study fluorine containing polymers and provides several advantages over other nuclei.[67-68] Firstly, it is 100% abundant and has the second largest gyromagnetic ratio amongst stable nuclei; hence, its sensitivity is similar to that of ^{1}H. As a consequence, it is common for fluorine to have strong homo- and hetero-nuclear dipolar couplings as long as no rapid motion is present. These can be exploited in 2D techniques to provide information about the connectivity and spatial proximity of the nuclei involved. For non-perfluorinated systems, hetero-nuclear couplings to protons can be easily removed by using multi-pulse decoupling sequences.[41-42] Secondly, fluorine is very sensitive to its local environment owing to its large chemical shift range, similar to ^{13}C, making it a useful structural probe.

There are no inherent problems in carrying out SSNMR experiments on non-hydrogen containing fluoropolymers, since only a single high-band channel is required. This leaves out a large class of materials that contain both ^{1}H and ^{19}F nuclei. Study of these systems requires probes that are capable of being tuned close in frequency (~ 30 MHz for a 500 MHz magnet), while still operating at high power (around 1 kW). Probes with this capability became commercially available in the last decade and have sparked interest in the study of these materials.

1.4.7 Simulation of SSNMR

SSNMR is a vast and quickly evolving field in which new and more sophisticated techniques are continuously being developed; therefore, an efficient method of simulating the spin dynamics during pulse sequences is essential in the development and understanding of these techniques. This is not an easy task, as the SSNMR Hamiltonian contains multiple terms which are orientationally dependent with respect to the static magnetic field (see section 1.3.3). Many different software suites, such as SIMPSON[69] and GAMMA,[70] have been developed and are implemented for two purposes: (1) the accurate simulation of NMR line shapes and powder patterns, such that structural information can be extracted, and (2) understanding how the interactions present within the Hamiltonian effect the outcome of NMR experiments. The DIVAM simulations presented in chapters 2 and 3 were performed using the SIMPSON[69] simulation program.

The SIMPSON program is optimized for the fast calculation of multiple-pulse MAS NMR experiments and is coded in the Tcl scripting language.[71] SIMPSON is unique because it was the first software package to be completely modular in design, making it the ideal platform for a virtual spectrometer. The modularity is achieved by creating four different sections in the code of an input file. The first section (spinsys section) allows the user to set the nuclei which are present and control the internal interactions of the spin system. This gives the user control over spin-spin interactions, such as J and dipolar coupling, as well as single spin interactions, such as the isotropic chemical shift, CSA, and quadrupolar coupling. The chemical shift tensor convention used in SIMPSON is the Haeberlen convention presented earlier in section 1.3.3.[31] The second section (par section) allows for careful control over the various parameters in the

simulations. These include the setup and acquisition parameters such as the MAS rate, static field strength (B_0), number of points, sweep width, the initial state of the magnetization, and the detection operator, as well as advanced computational parameters, such as the type of powder averaging. The third section (pulseq section) gives the user direct control over both the application of RF pulses and the delays that occur during the pulse sequence. This is analogous to the pulse sequence coding used when implementing experiments on a real spectrometer and is the key element that makes SIMPSON an ideal virtual spectrometer. One distinct advantage of the pulse sequence section is that the propagator for the application of various pulses and delays can be stored and re-used at a later point. This can be a very powerful capability when studying both two-dimensional NMR, and the application of various decoupling techniques in solid-state NMR.[72] The last section (main section) is used both to start the simulation, and process the simulated data. The *fsimpson* command starts a simulation and stores the resulting data in an array named by the user. This data can then be processed with zero-filling, line broadening, and phasing and subsequently Fourier transformed into a spectrum for interpretation. More importantly, SIMPSON allows the user to save the data at any point during the manipulation process; hence, the data can be saved as an FID and spectrum before and after the application of processing. Also, the robust use of data arrays in SIMPSON provides a method by which advanced multi-dimensional NMR experiments can be simulated.

SIMPSON calculates the density matrix at any given point in time by a direct time integration of the Louiville-von Neumann equation (see equation 58). The Hamiltonian used in the propagator and the initial density matrix of the system are

composed of the various internal interactions which are set in the spin system and parameter sections of the input file. The NMR signal is obtained by calculating the expectation value of the detect operator, defined in the parameter section of the input file, as given in equation 54. In order to obtain the signal for the entire powder sample a process known as powder averaging must be carried out.

Powder averaging in SIMPSON is carried out by calculating the signal over a discrete sum of pre-defined Euler angles (α, β, γ), where each set of Euler angles represents a different crystal orientation with respect to the static magnetic field. There are multiple different types of averaging schemes available, each of which is designed to more efficiently sample the various crystallite orientations in the unit sphere; however, SIMPSON uses two of the more common schemes known as the Lebedev[73] and REPULSION[74] methods. As mentioned earlier, sample rotation (MAS) creates a periodically time dependent Hamiltonian (figure 21, page 50). The Euler angle given by gamma represents rotation about the magic angle or rotor axis; therefore, the *gamma_angles* parameter determines how many points will be sampled inside one complete rotation of the rotor. The *crystal_file* parameter then specifies a set of alpha and beta angles that will be varied for each of the gamma angle points in one complete rotation of the sample.

SIMPSON gives the user control over the external interactions of the Hamiltonian (Section 1.3.2). The strength of the static magnetic field is defined in the parameters section of the input file; conversely, control of the applied RF pulses is not quite as simple. An applied RF pulse can be defined as either ideal or real. An ideal (hard) pulse is considered to be infinitely sharp and excites all of the chemical shifts equivalently

while a real (soft) pulse takes into account the duration and strength of the pulse when exciting the spin system. All of the simulations used in chapters 2 and 3 were carried out using real pulses.

SIMPSON presents a very robust way to simulate solid-state NMR experiments but, it does have a few key shortcomings. The simulation of the Hamiltonian uses the secular approximation and does not take into account the effects of non-secular terms. Furthermore, SIMPSON does not take into account the effects of relaxation and dynamics (motion). As a direct result, the SIMPSON analysis presented in chapters 2 and 3 considers only the effects of spin dynamics. A set of analytical expressions had to be developed in order to consider the combined effects of relaxation and spin dynamics.

1.5 Solid-state NMR of Polymers

1.5.1 Overview

Polymer science aims at creating novel polymer materials that possess an ideal set of properties and functions for specific applications in the everyday world. In order to achieve this, the relationship between the macroscopic properties and the molecular structure and dynamics of the molecule must be understood. Single-crystal X-ray crystallography is not possible for polymeric materials and powder X-ray diffraction can only be used to obtain the unit cell information. Furthermore, X-ray crystallography cannot provide any structural information of the non-crystalline region of polymers, such as highly mobile (amorphous) chain segments. SSNMR spectroscopy has been an invaluable tool in the study of polymers because it can provide structural and dynamic

information on both the mobile and rigid regions of a polymer, regardless of the overall crystallinity.

1.5.2 Polymers

A polymer is a long chain macromolecule that is composed of repeating structural units. The elements that compose the repeating units of a polymer determine whether it is classified as organic, inorganic, or biological. Furthermore, a polymer can be composed entirely of the same repeating unit or it can contain several different repeating units. These are known as homo- and co-polymers, respectively.[75-76]

Earlier it was mentioned that polymers do not necessarily have high crystallinity. A certain class of polymers are semi-crystalline in nature and contain both crystalline (rigid) and amorphous (mobile) phases,[77] as seen in figure 32. The semi-crystalline nature of these polymers is a direct result of the crystallization process. During crystallization it is possible for a segment from one crystalline segment to be incorporated, or intertwined, with another crystalline segment and this leads to regions of the polymer that are disordered, or entangled. These entangled regions do not crystallize, forming the amorphous phase of the polymer. The percent crystallinity of a polymer depends greatly on the regularity of the repeating unit in the chain structure; therefore, polymers that possess either very large functional groups or defect units, due to improper addition of monomers, tend to have lower crystallinity.

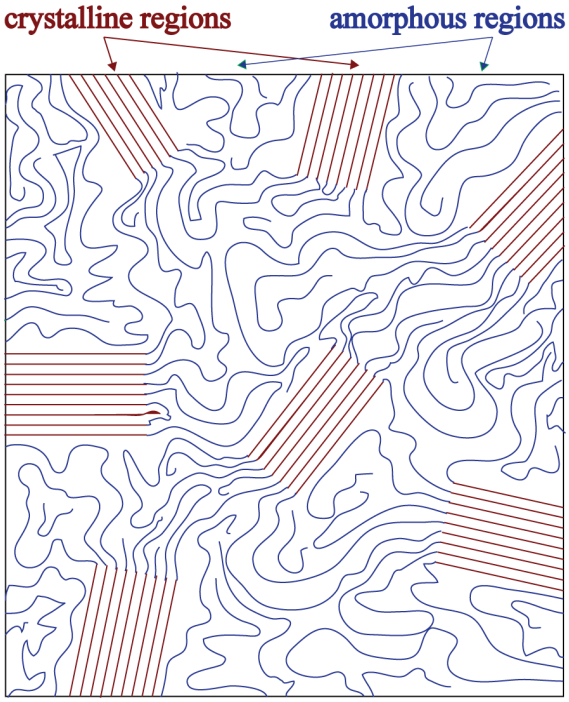

Figure 32 A schematic representation of the phase structure of semi-crystalline polymers.[18]

The crystalline and amorphous phases in a polymer have unique and useful macroscopic properties. The crystalline regions give rise to the rigid properties of the polymer, such as strength and thermal stability, while the mobile amorphous phase leads to properties such as flexibility and permeability.[75] A semi-crystalline polymer is therefore much more versatile than a purely crystalline polymer; therefore, it can be processed in many different ways for use in varying applications. This processing ranges from heat treatment of the polymer (annealing), to mechanical treatments, such as stretching the polymer. An understanding of the microscopic structure and dynamics of both the crystalline and amorphous phases is essential in developing the potential macroscopic properties of these polymers.

1.5.3 High Resolution SSNMR Techniques

SSNMR provides information on both the structure and dynamics of the amorphous and crystalline phases of polymers. The crystalline phase of a polymer is highly ordered and the spins in adjacent chains interact in a very structured manner. In contrast, the amorphous phase of a polymer is highly mobile and the spins from various chains interact in a random manner. As a result, the CSA and dipolar terms, as well as the relaxation times, of each phase (domain) will be different. Crystalline domains are usually characterized by short transverse relaxation times and large chemical shift anisotropies due to the presence of large dipolar interactions and the orientation dependence of the crystalline unit. In contrast, amorphous domains have much longer transverse relaxation times and smaller chemical shift anisotropies due to averaging of the tenors, or scaling, caused by molecular motion. The rest of this text will discuss the application of SSNMR to a very specific type of semi-crystalline inorganic polymers, known as fluoropolymers.

Fluoropolymers see widespread commercial application, such as non-stick coatings (Teflon™), textiles (Gore-tex™), fuel cell membranes (Nafion™), and electronic devices (poly(vinylidene fluoride)).[78-80] Poly(vinylidene fluoride) (PVDF) is a semi-crystalline fluoropolymer that is exploited for its piezo- and pyro-electric properties in actuators, transducers, and coatings. The general structure of PVDF is given in figure 33 and has 4 common crystal polymorphs (α, β, γ, and δ) that can be formed based upon the processing conditions.[81]

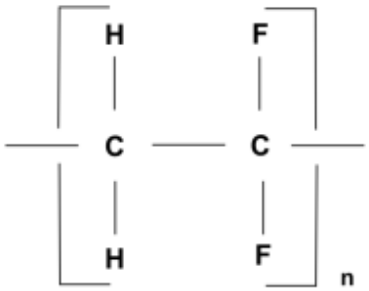

Figure 33 The polymer structure of PVDF.

The β polymorph of PVDF is highly polar as it consists of an all trans chain alignment in which the dipole moments of fluorine point in the same direction (figure 34a). This polymorph is commonly applied in the electronic devices mentioned above. The α polymorph of PVDF is non-polar and consists of a unit cell composed of a $tg^{+}tg^{-}$ conformation (figure 34b); therefore, the fluorines in the crystalline unit cell of the β polymorph are equivalent, while those in the α polymorph are not.

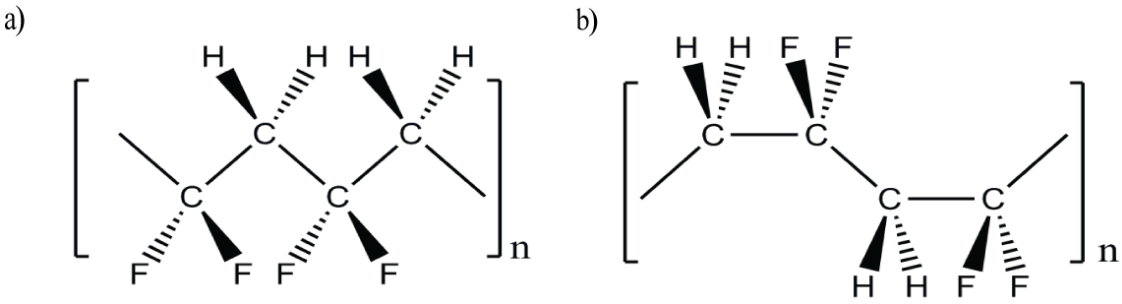

Figure 34 The a) β and b) α polymorphs of PVDF.

The structure of the various polymorphs of PVDF has been studied extensively using NMR spectroscopy;[82-87] however, only the α polymorph of PVDF will be presented and discussed here.

The ^{19}F MAS SSNMR spectrum of a PVDF sample that is primarily α-PVDF (figure 35) contains two broad signals at –82.1 and –95.6 ppm corresponding to the two non-equivalent crystalline domains and one narrow peak at –91.2 ppm that represents the amorphous domain.[88-92]

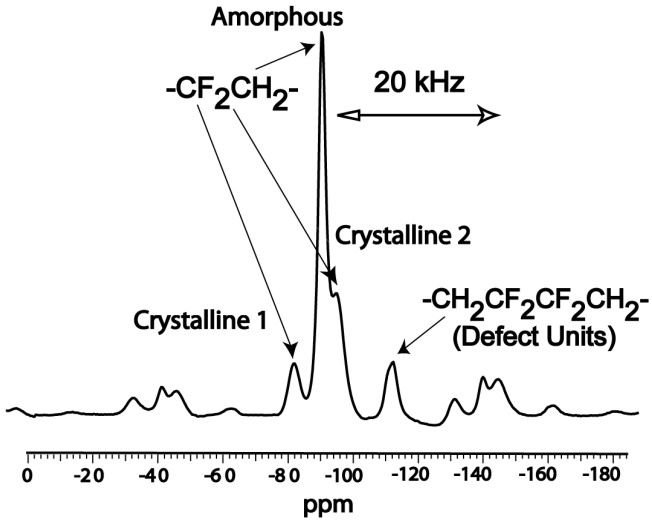

Figure 35 The ^{19}F MAS SSNMR spectra of α-PVDF acquired at an MAS rate of 20 kHz with proton decoupling and its structural assignment. The spectra was referenced with respect to C_6F_6.

As mentioned above, the crystalline signal is characterized by a short T_2 and large CSA, while the amorphous signal has a much longer T_2 and a smaller CSA, due to molecular motion. A broad peak of low intensity is composed of two peaks at –118.3 and –114.9 ppm from the two adjacent CF_2 groups of the defect unit, which is formed due to the occasional reverse addition of the monomer units during polymerization. Furthermore, a low intensity signal is present at –115 ppm and has been observed elsewhere and shown to be the CF_2H end chain signal.[88]

SSNMR gives valuable insight into the structure and dynamics of the various phases of a polymer that cannot necessarily be obtained through X-ray crystallography

studies. The study of polymers by SSNMR spectroscopy can be broken down into 3 main categories: polymer connectivity, polymer dynamics, and domain selection methods.

Polymer connectivity can be studied through various 1D and 2D NMR techniques. The 1D spectrum of a polymer can contain signals corresponding to the chemical shift of the various structurally unique environments in the polymer in their respective phases. Provided that sufficient resolution is achieved, the 1D spectrum gives the chemical shift, line width, intensity, and area (composition can be determined through de-convolution studies). Also, if the signal from the end-chain of the polymer can be resolved its area can be used to determine the relative length of the polymer chain. 2D NMR techniques are applied to determine the through bond connectivity and spatial proximity within a polymer. Several through space 2D SSNMR techniques that are based on correlation via the dipolar coupling are routinely used in the study of polymers.[51, 54-55, 57, 93-94] These include both hetero-nuclear and homo-nuclear techniques, such as HETeronuclear CORrelation (HETCOR) [95-96] and Radio Frequency Driven Recoupling (RFDR),[97-98] respectively. The application of through-bond 2D SSNMR techniques are not as common in the study of polymers and these include homo- and hetero-nuclear methods such as: Incredible Natural Abundance Double QUAntum Transfer (INADEQUATE),[99-100] Hetero-nuclear Multiple-Quantum Correlation (HMQC),[101] and Hetero-nuclear Single-Quantum Correlation (MAS-J-HSQC).[102] These techniques provide the necessary information to obtain the average local atomic structure of a polymer; however, polymers are not static in nature.

SSNMR is a powerful tool for investigating the dynamic behavior of both the crystalline and amorphous phases within a polymer. As mentioned before, dynamics in a

polymer leads to its elasticity and renders it permeable. The most common way to investigate dynamics in a polymer is through its relaxation parameters (T_1, $T_{1\rho}$, and T_2). By measuring the relaxation parameters at various temperatures the rate of motion of a specific process can be determined and this information can be used to determine the corresponding energy. Cross-polarization dynamics is also very useful in investigating motion as it provides useful information on the average dipolar interaction of the motion. There are several 2D NMR techniques available to study the dynamics of a polymer; two common techniques are 2D EXchange SpectroscopY (EXSY)[103] and Centerband-Only Detection of EXchange (CODEX).[3] Both techniques allow longitudinal magnetization to be exchanged between two nuclei via chemical exchange rather than polarization transfer. These methods allow for the study of slow dynamics (~10^{-1} – 10^4 Hz), such as those seen near the glass transition temperature of polymers.

1.5.4 Domain Selection Methods

The amorphous and crystalline phases, or domains, tend to have different chemical shielding and relaxation parameters; however, the chemical shift difference is not always large enough to distinguish between the signals from both domains. Most often this occurs when similar chemical groups, such as a CF_3 group, are present in both the amorphous and crystalline phases. This can be particularly problematic when dealing with spins that undergo strong homo-nuclear dipolar couplings, such as the ^{19}F nuclei in fluoropolymers, where the line width for both domains is very broad and their spectral lines overlap. A method must be developed to separate the line shapes of each phase so that their structure and dynamics can be studied separately. This capability is extremely

important when measuring the sizes of polymer domains, which has a tremendous influence on the macroscopic properties of a polymer.[104]

Domain selection is achieved through a suite of methods that separate signals via differences in the relaxation, CSA, and dipolar couplings of each domain.[105] Relaxation methods are applied mainly to abundant nuclei and differentiate signals on the basis of the T_1, $T_{1\rho}$, and T_2 times in each domain.[106] The most basic form of selection is the CP sequence outlined earlier.[107] The dipolar interaction is much stronger in a crystalline domain than in an amorphous domain, and as a result, its optimum contact time is much shorter. Hence, by selecting a short contact time the signal from the amorphous domain does not have sufficient time to cross-polarize, leaving only signal from the crystalline domain. This is the simplest way to select for the signal from the crystalline domain. CP is also incorporated in other methods that are used to discriminate between domains based on the T_1, $T_{1\rho}$, and T_2.

The pulse sequences for the pre- and post-CP inversion recovery experiments are given in figure 36a and 36b, respectively. In both of these experiments the magnetization from each domain is placed on the –z-axis (inverted) and is then allowed to relax back to equilibrium during the delay period (τ). The domain with a shorter T_1 can be effectively removed by setting the delay period to approximately 70 percent of the T_1 value. The pre-CP sequence applies the filter on the *I* nucleus and achieves inversion with the application of a 180 degree pulse, while the post-CP sequence applies the filter on the second nuclei (*S*) and uses a 90 degree pulse before and after CP to effectively place the magnetization along the –z-axis. It is important to note that the presence of strong homo-nuclear dipolar couplings can remove the differences between T_1's as a result of

averaging. Consequently, these experiments are not commonly used in studying semi-crystalline fluoropolymers;[108] however, experiments based upon both $T_{1\rho}$ and T_2 are common.

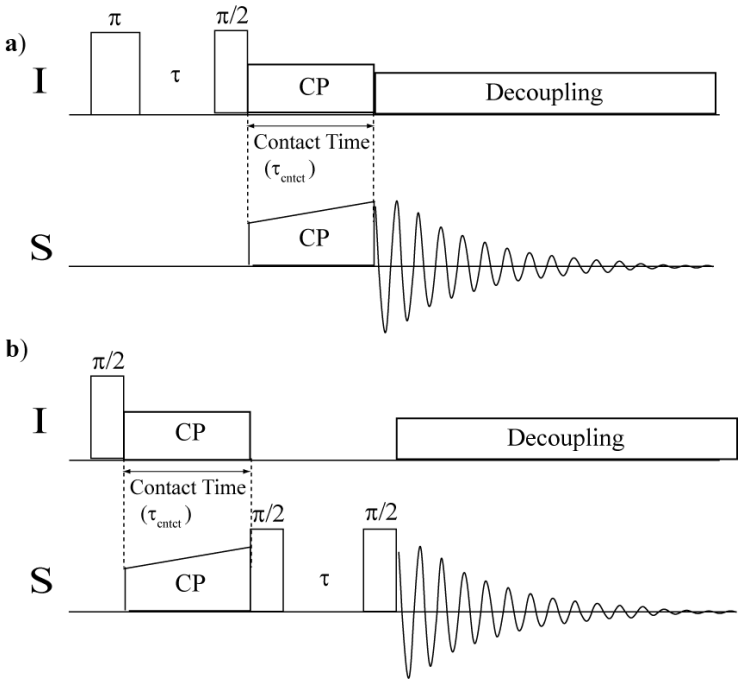

Figure 36 The a) pre-CP and b) post-CP inversion recovery sequences.

Domains in a polymer can have significantly different $T_{1\rho}$ times; hence a spin-lock can be used to remove the signal from the domain with the shortest $T_{1\rho}$. This spin-lock can be applied either before or after CP resulting in selection based on $T_{1\rho}$ of either the *I* or *S* nuclei, respectively (see figure 37).

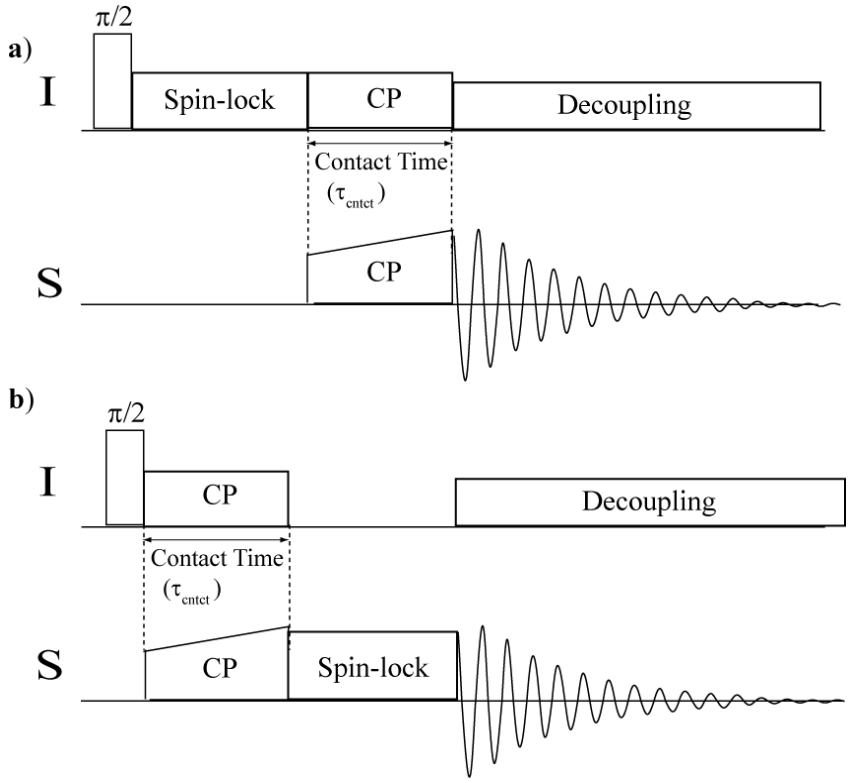

Figure 37 The a) pre-CP and b) post-CP spin-lock sequences.

The domain selection techniques outlined above can be used to remove signals from the amorphous domain of a polymer because it typically has much shorter T_1 and $T_{1\rho}$ times then the corresponding crystalline domain. In contrast, amorphous domains typically have a much longer T_2 than crystalline domains; hence allowing for selection.

There are several sequences that select on the basis of differences in the transverse relaxation rates, three of which are given in figure 38. The dipolar dephasing sequence (figure 38a)[109-111] is similar to the basic CP experiment but adds an extra delay time (τ) before CP occurs. Crystalline domains have much shorter T_2 times than amorphous domains; therefore, this delay can be set such that the signal from the crystalline domain dephases, leaving only the signal from the amorphous domain to undergo CP. Unfortunately, the dipolar dephasing sequence also allows for evolution

under both the chemical shift and dipolar terms of the Hamiltonian and this can lead to significant phase distortions in the observed amorphous spectra. The addition of a Hahn-echo in the middle of the dephasing period refocuses the chemical shift hetero-nuclear dipolar coupling terms and reduces the phase distortions. The Hahn-echo can be applied either before or after CP resulting in the selection of the amorphous signal based upon the T_2 of the crystalline domain for the *I* or *S* nuclei, respectively (figure 38b and 38c).

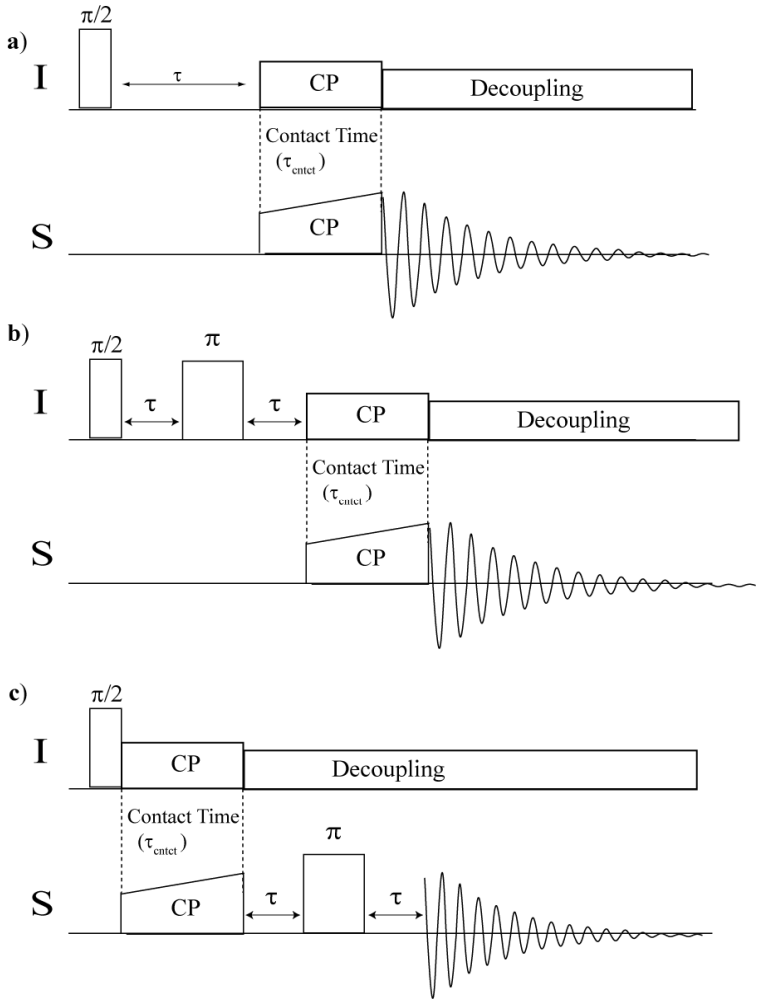

Figure 38 The a) Dipolar dephasing, b) pre-CP Hahn-echo, and c) post-CP Hahn-echo sequences.

Domain selection can also be achieved by manipulating the internal interactions of the Hamiltonian. This discussion will focus primarily on techniques designed to select on differences in the dipolar interaction. As mentioned previously, CP is the most common form of dipolar selection. The Dipolar filter[112-113] is a multiple pulse sequence used to select the amorphous domain of a polymer (figure 39) by allowing the crystalline signals to dephase under evolutions due to the dipolar interaction. The filter consists of 12 90 degree pulses that follow the phase cycle shown below and are separated by an inter-pulse delay (τ).

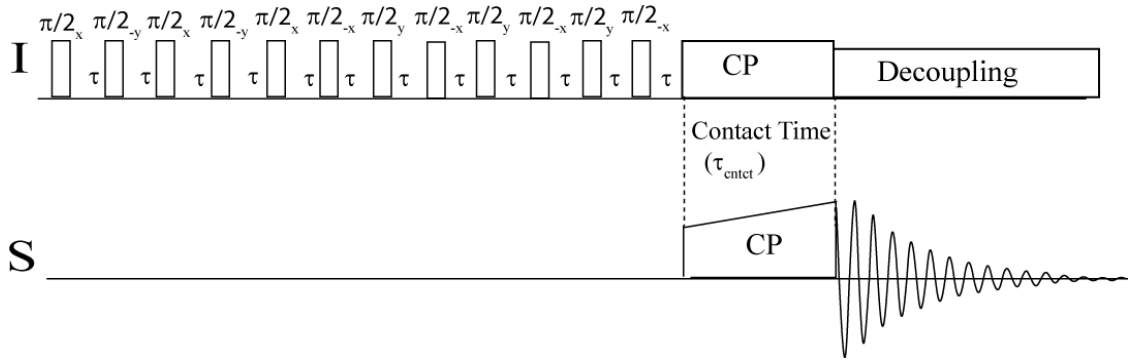

Figure 39 The Dipolar Filter pulse sequence.

The combination of an appropriate phase cycle and inter-pulse delay refocuses only weak dipolar couplings. As a result the signal from crystalline domains will dephase during the pulse train, while the signal from the amorphous domain will not, leaving only the signal from the amorphous domain to be cross-polarized following the train. All of techniques outlined above have one thing in common, they select for the signal from a specific domain; therefore, multiple pulse sequences must be used in order to select for both domains. The Discrimination Induced by Variable Amplitude Mini-pulses (DIVAM)

sequence[91, 114] allows for the selection of both domains with the use of only one pulse sequence.

2. THE DISCRIMINATION INDUCED BY VARIABLE AMPLITUDE MINI-PULSES (DIVAM) SEQUENCE

2.1 Overview

The DIVAM sequence (figure 40a) can be fine tuned to select for the signal from a particular structural domain in a polymer. In this manner it is possible to obtain signals specific to different domains using only one experiment. The DIVAM sequence is similar to the Dipolar filter sequence (DF) (figure 39) as it is composed of 12 pulses separated by an inter-pulse delay (τ). However, unlike the DF, the flip angle of the pulses, referred to as the excitation angle (θ), is no longer fixed at 90 degrees and their phases remain constant. The DIVAM sequence is repeated n-times with the excitation angle varied from 0º to 90º in n-steps. The excitation angle is varied by changing the pulse field (RF) strength while keeping the pulse duration constant.

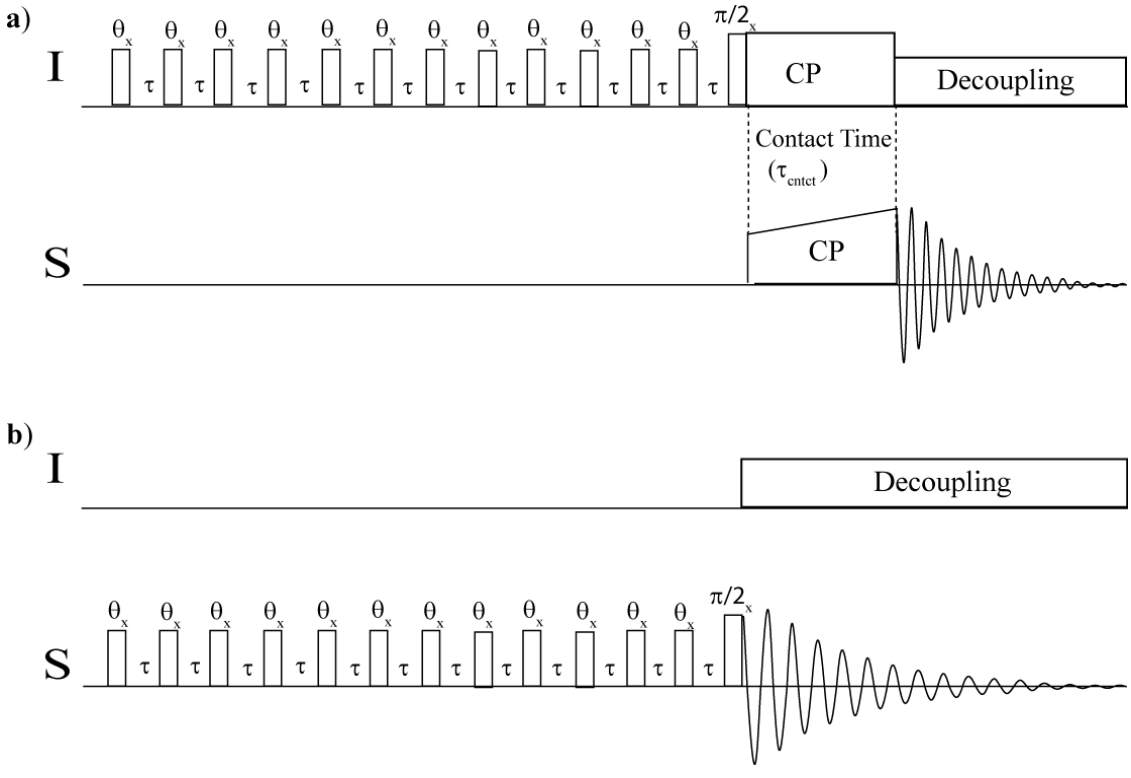

Figure 40 The **a)** CP and **b)** Direct DIVAM pulse sequences.

Originally, the DIVAM sequence was applied to an abundant nucleus, *i.e.* ^{1}H, and subsequently cross-polarized to the nuclei of interest, *i.e.* ^{19}F (referred to as CP DIVAM). In the case where CP is not possible from proton, *i.e.* for perfluorinated or high mobility materials, the DIVAM sequence is applied directly to the nucleus of interest (referred to as Direct DIVAM[115-117]), as shown in figure 40b. The domain selection in PVDF for both sequences will be presented and explained in this chapter.

2.2 Experimental

The α-PVDF sample had a molecular weight of $1x10^{6}D$ as determined by gel permeation chromatography (GPC), crystallinity of ~28% and reverse unit content of 4.7% as determined by NMR, and a melting point of 158 ^{o}C as determined by differential scanning calorimetry (DSC).[118-119] The sample of α-PVDF was supplied by Atofina, France. All measurements were made on a VARIAN INOVA 500 MHz NMR spectrometer operating at a carrier frequency of 470.18 MHz for fluorine and 500.00 MHz for proton. A Varian 2.5mm four channel HFXY probe operating at 21 ^{o}C and capable of MAS speeds up to 30 kHz was used. The 90^{o} pulse was calibrated at 2.5 μs for both the fluorine and proton nuclei which corresponds to an RF field strength of 100 kHz. The RF resonance frequency during acquisition was set to the amorphous peak of PVDF at –91.2 ppm. TPPM decoupling was applied to ^{1}H during fluorine acquisition and also during spectral referencing so that the Bloch-Siegert shift could be neglected.[67-68] Spectral referencing was done using C_6F_6 (δ_F = –166.4 ppm with respect to $CFCl_3$) as an external reference. Zirconium oxide rotors with Vespel drive caps were used in order to avoid unwanted fluorine background signal.

The CP and Direct DIVAM sequences were performed using twelve 2.5 μs excitation pulses (pulse width (pw) = 2.5μs), with the RF frequency centered on the amorphous signal of PVDF, each separated by an inter-pulse delay (τ), and were terminated by a 90^o observation pulse. Measurements for the nutation series were made with the pulse excitation angle (θ) varied from 0^o to 90^o in 2.5^o steps with the inter-pulse delay fixed at 1.67 μs (τ =1.67 μs). The variance of the pulse excitation angle (θ) was accomplished by altering the strength of the B_1 field, while keeping the pulse duration constant in order to attain rotor synchronization. The signal from the CP DIVAM pulse train was cross-polarized to fluorine using ramped CP with a contact time of 1 ms. Measurements of Direct DIVAM were also made for a series of fixed excitation angles, whilst varying the inter-pulse delay. The inter-pulse delays were chosen such that the total filtering time (T_F) was varied over different orders of magnitude of the rotor period and relaxation time. Throughout this work rotor synchronization is always with respect to T_F, where $T_F = (12 \times \tau) + (12 \times pw)$. All experimental measurements used an MAS rate between 20 and 25 kHz and the rate used for each experiment is indicated in the figure captions.

All simulations were carried out using SIMPSON 1.1.0[69] with an Intel Core 2 Duo 7200 processor. The Direct DIVAM simulations were run separately for three different terms in the Hamiltonian corresponding to the isotropic chemical shift, chemical shift anisotropy (CSA), and the dipolar coupling. For each of these terms the pulse sequence was simulated using real (soft) pulses and the strength of the Hamiltonian terms was varied in size from 0-50 kHz. These simulations were also run under timing

conditions in which the total duration of the pulse train was or was not synchronized with the rotor period.

The CSA and Isotropic terms of the Hamiltonian were simulated as a 1-spin system with the initial density matrix set as $\mathbf{I}_z$. The dipolar coupling term of the Hamiltonian was simulated as a 2-spin system with the initial density matrix set as $\mathbf{I}_z^{(1)} + \mathbf{I}_z^{(2)}$. At the end of the sequence the $\mathbf{I}_z$ component of the density matrix was reported as a function of the pulse excitation angle (θ). For the dipolar coupling simulations, only the $\mathbf{I}_z^{(1)}$ term of the density matrix was reported.

Simulations of the Direct DIVAM sequence were implemented using the same pulse values as in the solid state NMR measurements (pw_{90} = 2.5μs and τ = 1.67μs). The rotor-synchronized and non-rotor synchronized simulations used a spinning speed of 20 and 25 kHz, respectively. All simulations used the direct method of calculation and were powder averaged using 30 gamma angles and 168 crystal orientations. An example of the SIMPSON input file used to simulate Direct DIVAM can be found in Appendix 1.

All NMR spectra were processed using the MatNMR[120] 3.9 processing toolbox (© Jakko van Beek) for MathWorks™ MATLAB® 6.5. The polymer chemical structure representations were created in CambridgeSoft® ChemDraw© Ultra 11.0.1. All figures were created with a combination of Adobe® Illustrator© CS4, Microsoft® Office Excel© 2007, and SigmaPlot® 2000 software.

2.3 The Original CP DIVAM Sequence

2.3.1 Experimental Results

The CP DIVAM nutation array of the ^{19}F MAS NMR spectra of PVDF is shown in figure 41.

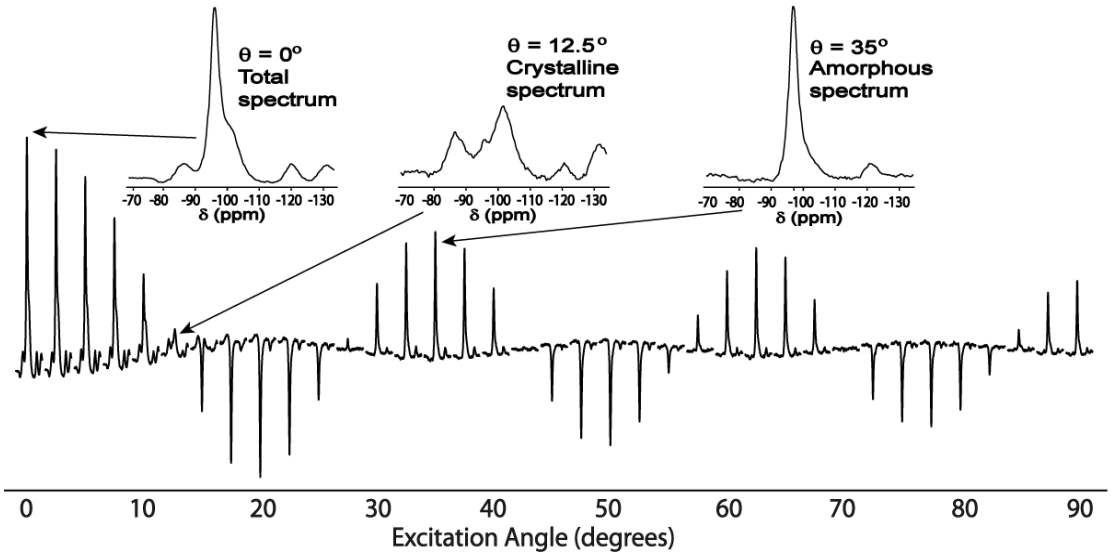

Figure 41 The CP DIVAM nutation array of the ^{19}F MAS NMR spectra of PVDF over a series of excitation angles with an inter-pulse delay of 1.67 μs and a pulse width of 2.5 μs (T_F = 50 μs). The nutation array ranges over excitation angles of 0^o-90^o in steps of 2.5^0 and was acquired at a spinning speed of 20 kHz. Enlargements of the ^{19}F MAS NMR spectra of PVDF for selected excitation angles are shown above the array.

All of the signals in the ^{19}F NMR spectra of PVDF nutate with respect to excitation angle; however, there are some important differences in the nutation behaviour of the various signals of PVDF. Firstly, the amorphous signal nutates at a rate much faster than the signals from the crystalline domain. This is particularly noticeable at the excitation angle of 12.5^o where the amorphous signal has no transverse component (null state) and only the crystalline signals remain. Later, at an excitation angle of 35^o, the crystalline signals pass through a null state leaving only the amorphous signal in the spectrum.

Lastly, the defect signals appear to nutate at a rate very similar to that of the amorphous signal. This would indicate that the defect units are in a similar chemical environment to the amorphous domain. In fact, other studies have used 2D NMR spectroscopy to show that the defect units are indeed coincident with those of the amorphous regions of the polymer.[88]

Previous work on CP DIVAM has shown that no transient behavior is seen on a time scale determined by the rotor period when incrementing the inter-pulse delay.[114] This would indicate that the spin dynamic terms (coherent terms) that have an orientation dependence, such as the CSA and dipolar coupling, are not dominate in the selection mechanism of CP DIVAM; therefore, the mechanism of domain selection in CP DIVAM can be explained using a simple on-resonance one-spin-relaxation model.

2.3.2 Selection Mechanism

The DIVAM sequence can be thought of selecting on the basis of differences in transverse relaxation between domains, which was demonstrated using a one-spin relaxation model (Figure 42). Each pulse in the DIVAM train rotates the longitudinal component of the magnetization from each signal into the transverse plane. During the inter-pulse delay the transverse components from each signal dephase at differing rates, resulting in a difference in their net angle of rotation from the z-axis. Upon each pulse-delay cycle this phase difference accumulates resulting in a significant net difference in their nutation rates with respect to the excitation angle. At a given excitation angle (θ) one of the components will be perpendicular to the z-axis (or static field) and the signal is

effectively placed in a null state upon the application of the terminal 90^{o} pulse. As a result the signal from the remaining domains is observed.

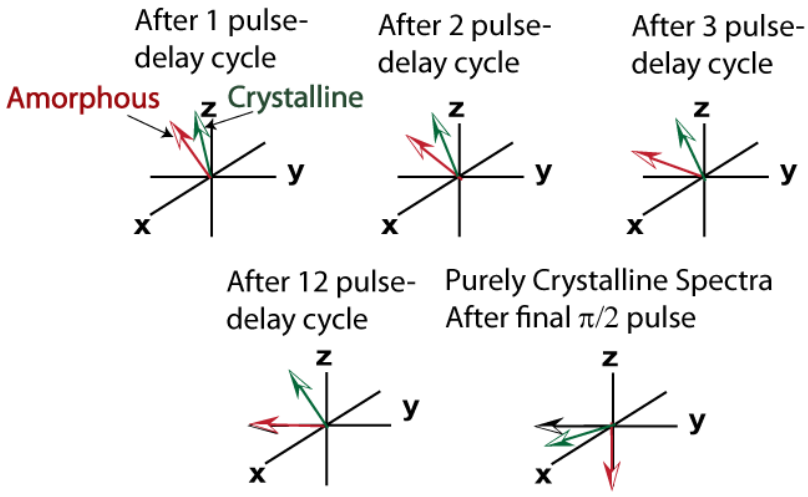

Figure 42 A vector diagram of magnetization from the two domains, with differing T_2 relaxation times, under the operation of the CP DIVAM pulse train.

2.4 The Direct DIVAM Sequence[1]

2.4.1 Experimental Results

The Direct DIVAM nutation array of the ^{19}F MAS NMR spectra of PVDF is shown in figure 43. In this case, not every signal in the ^{19}F NMR spectrum of PVDF is seen to nutate with respect to excitation angle and some important differences in the behaviour between signals can be seen. Firstly, the amorphous signal nutates for small angles and passes through a null state at 17.5^{o}, resulting in the selection of the crystalline signal; however, the amorphous signal stops nutating for excitation angles greater than

[1] Reproduced in part with permission from Hazendonk, P.; Wormald, P.; Montina, T. The Direct DIVAM Experiment: A Spin Dynamics Analysis. *Journal of Physical Chemistry A* **2008,** *112,* 6262-6274.Copyright 2008 American Chemical Society

60^{o}. Secondly, the crystalline signals are not seen to nutate for any excitation angle; however they do appear to pass through a null state at an excitation angle of 42.5^{o}. This state is most likely due to coherent dephasing of the crystalline signals in the transverse plane and allows for the selection of the amorphous signal. Thirdly, the signals from the defect units do not appear to nutate at all. Lastly, significant phase distortions are present at excitation angles greater than 60^{o} and the surviving transverse components indicate that the spin dynamics of the system are an important part of the selection mechanism.

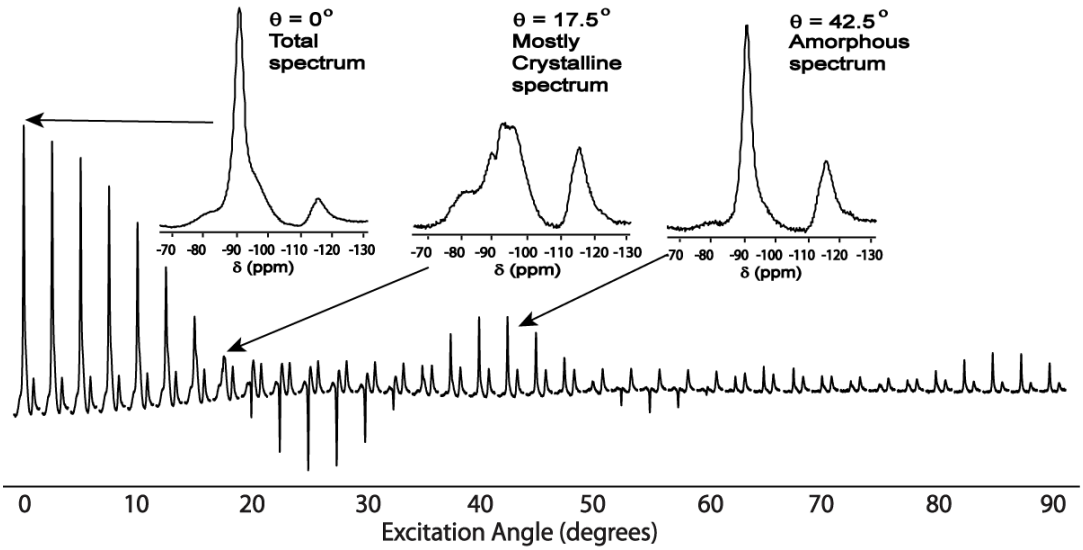

Figure 43 The Direct DIVAM nutation array of the ^{19}F MAS NMR spectra of PVDF over a series of excitation angles with an inter-pulse delay of 1.67 μs and a pulse width of 2.5 μs (T_F = 50 μs). The nutation array ranges over excitation angles of 0^{o}-90^{o} in steps of 2.5^{0} and was acquired with a spinning speed of 20 kHz. Enlargements of the ^{19}F MAS NMR spectra of PVDF for selected excitation angles are shown above the array.

The involvement of spin dynamics in the selection mechanism of Direct DIVAM is not surprising, as the filter is being applied directly to the fluorine nucleus. Fluorine is an abundant nucleus that experiences strong dipolar couplings and has a very large CSA, in contrast to the ^{1}H nucleus which has a very small CSA. The involvement of the CSA

and Dipolar terms in the selection mechanism of Direct DIVAM should lead to observable transient behavior on a time scale determined by the rotor period. This is because the CSA and Dipolar terms contain an orientationally dependant term that is sensitive to the phase of the rotor. Therefore, detecting the spectra under varying rotor synchronization conditions should lead to an observable difference in the detected spectra. A series of experiments were carried out in which the excitation angle was fixed while varying the inter-pulse delay such that the total filtering time (T_F) was varied over different time scales representative of the rotor period and spin-spin relaxation time (T_2).

Figure 44 illustrates the change in the spectra for each of the selected excitation angles as the inter-pulse delay is varied such that the T_F ranges over approximately two rotor periods (T_R) in steps of 3/40 T_R (henceforth referred to as the short time series). Little to no variation is seen in the signal intensity with respect to the T_F for small excitation angles. For example, in the 2.5^o series (Fig. 43 bottom row) the signal intensity does not vary with delay time. Also note in the 15^o series (Fig. 43 second from bottom) the amorphous signal is near its first null state, with its intensity being mostly suppressed, and this clearly indicates that the crystalline signals do not appear to change with respect to inter-pulse delay used. Variations in signal intensities with respect to the T_F, or alternatively with rotor phase, become evident when excitation angles larger than 30^o are used. When considering excitation angles of 45^o and higher the amorphous signal passes through at least one complete oscillation. Similar oscillations can be seen in the crystalline signals; however, they are less dramatic.

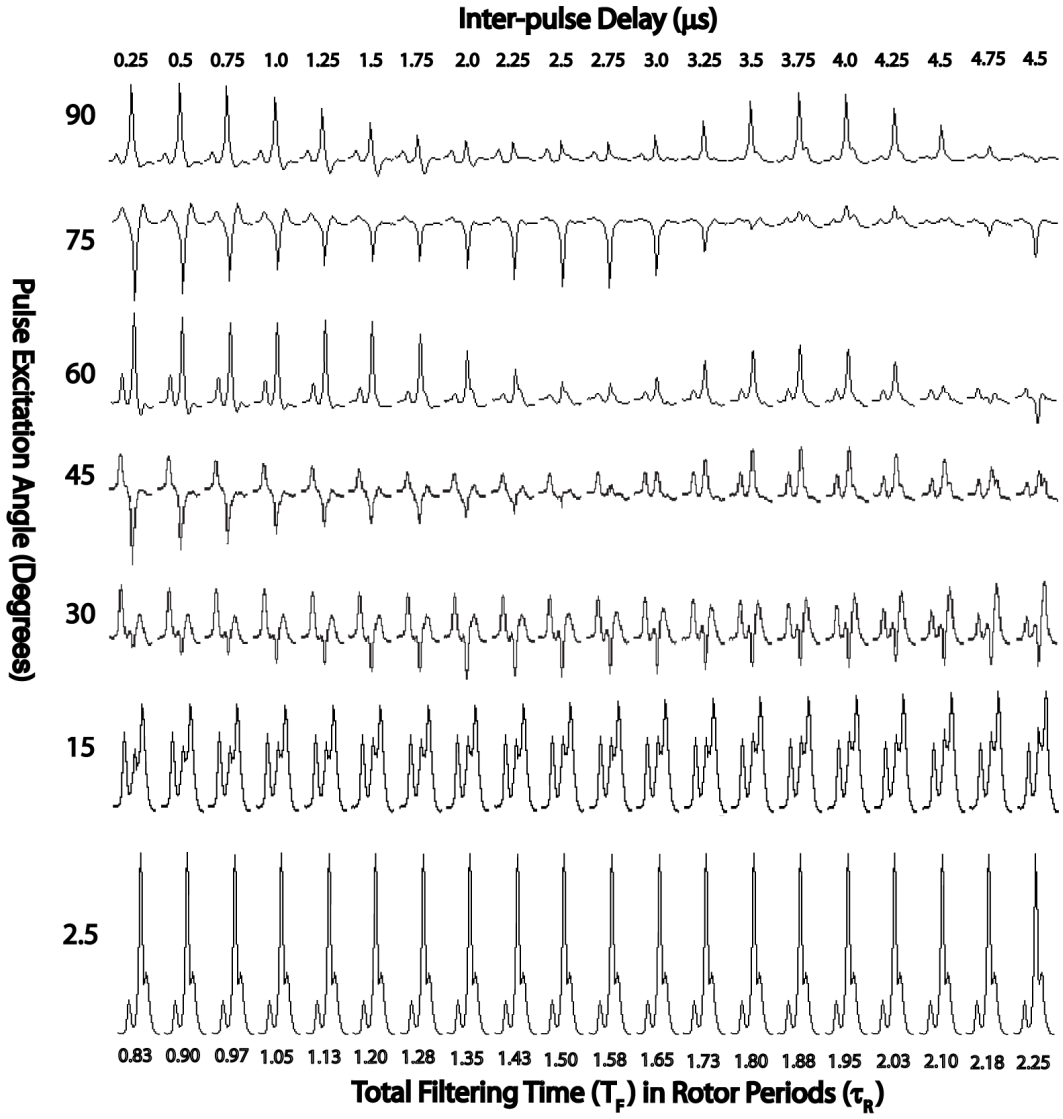

Figure 44 ^{19}F Direct DIVAM spectra of PVDF over a series of inter-pulse delays, calibrated such that T_F covers 0 to 2 rotor periods (T_R). This array is shown for selected excitation angles from 2.5 to 90 degrees using a MAS rate of 25 kHz and a pulse width of 2.5 μs.

Figure 45 illustrates the change in the spectra for each of the selected excitation angles as the inter-pulse delay is varied such that the T_F covers 2400 rotor periods in a non-linear fashion, somewhat logarithmic in nature, with the spacing increasing from 3, 6, 15, 150, 300 to 600 T_R (henceforth referred to as the long time series). The long time

series reflects the time scale of T_2 for PVDF, which along with their corresponding T_1 values are tabulated in table 2, where the inter-pulse delay ranges from 0.12 to 32 times T_2 for the amorphous signal, and from 0.40 to 100 times T_2 for the crystalline signals. For the small excitation angles, *ca.* 2.5°, the amorphous and crystalline signals remain unchanged as they experience little net rotation. For short delay times, as the excitation angles increases, their net rotation increases reducing their intensity until they reach their first null condition; however, as the delay time increases they recover intensity when exceeding the T_2 time scale. Beyond 45° each pulse significantly rotates the longitudinal magnetization into the transverse plane and this allows for dephasing of the signals due to transverse relaxation between each of the pulses (saturation effect). This effect becomes increasingly pronounced as both the excitation angle and inter-pulse delay are increased and eventually reaches a point at which the signal does not recover over the entire time range. The saturation effect will be further discussed and illustrated in the analytical expressions section.

Table 2 ^{19}F SSNMR Relaxation measurements of PVDF

Time Constant	T (°C)	Crystalline$_1$	Crystalline$_2$	Amorphous	Defect$_1$	Defect$_2$
T_1 (s)	60	0.63 ± 0.02	N/A	0.57 ± 0.02	0.59 ± 0.02	0.59 ± 0.02
T_2 (μs)	60	79.7 ± 2.39	135.6 ± 4.07	250.6 ± 7.52	251.0 ± 7.53	289.1 ± 8.67

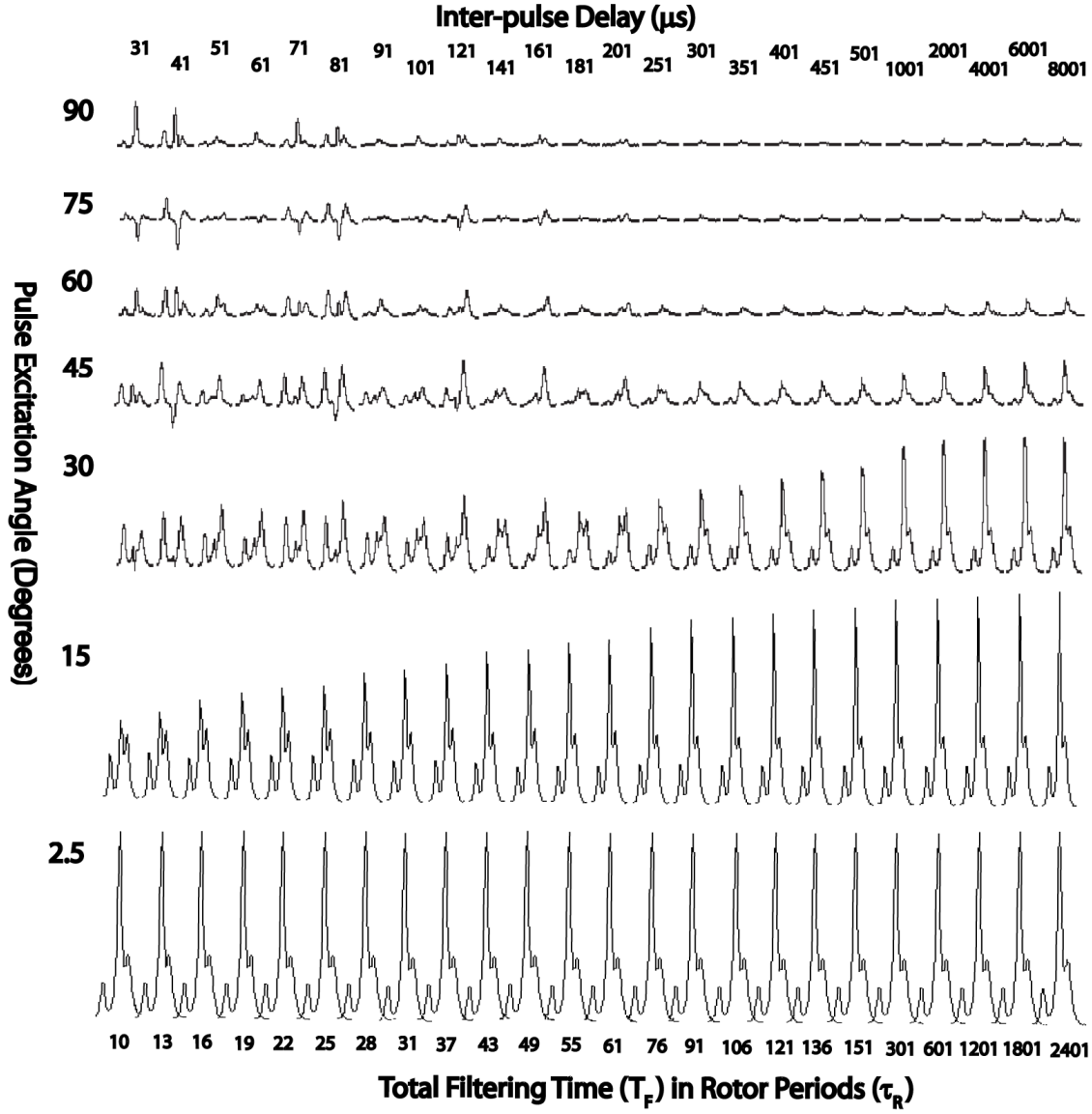

Figure 45 ^{19}F Direct DIVAM spectra of PVDF over a series of inter-pulse delays, calibrated such that T_F covers 3 to 2400 rotor periods (T_R). This array is shown for selected excitation angles from 2.5 to 90 degrees using a MAS rate of 25 kHz and a pulse width of 2.5 μs.

In summary the long and the short time series illustrate two aspects of the spin dynamics during the DD experiment as the excitation angle is increased. The short time series shows that transient oscillations are observed only for the larger excitation angles, *ca. 30^o or larger*. The long time series illustrates that the saturation effect is more pronounced with increasing excitation angle, which for long delay times recovers on the

T_2 time scale. Both results suggest that spin dynamics play an important role in the observed selection behavior and cannot be ignored.

2.4.2 Spin Dynamics

Simulations of the Direct DIVAM sequence were performed probing the effect of each term in the ^{19}F Hamiltonian separately, namely H^{iso}, H^{aniso}, and H^{dip}. Parallel simulations were performed using real pulses under both rotor-synchronized and non-rotor-synchronized conditions. The nutation behaviour of the longitudinal magnetization (z-magnetization) remaining after the filter sequence will be explained separately for each term in the Hamiltonian. This analysis will focus on examining observed differences in the zero crossings of the various signals representing different interaction strengths. A difference in zero crossings represents the condition in which one signal will be in a null state while the other still has significant z-magnetization; therefore, the application of the terminal 90 degree pulse will result in the selection of the non-zero signal.

I. Isotropic Offset Term

The isotropic offset term (H^{iso}) (figure 46) shows that for small frequencies, *ca* 10 kHz or less, the normal expected nutation behaviour is observed at a rate of 12 times the excitation angle, completing three full cycles by 90^o. As the isotropic term increases the nutation behaviour changes dramatically; the amplitude of the first cycle decreases and its nutation frequency remains essentially unchanged, except for rather large values, *ca* 15 kHz or greater. Furthermore, the first zero crossing, or null state, of the z-

magnetization increases with increasing offset; and hence selection can be achieved via an offset term of 5 kHz or greater. One should note that the DIVAM sequence is used to discriminate between overlapping signals; hence, differences in isotropic frequency are not of particular interest, unless overlap from sideband signals is significant and cannot be avoided. No difference is observed between the rotor synchronized and non-synchronized cases, which is also to be expected as the isotropic term is not modulated by sample rotation.

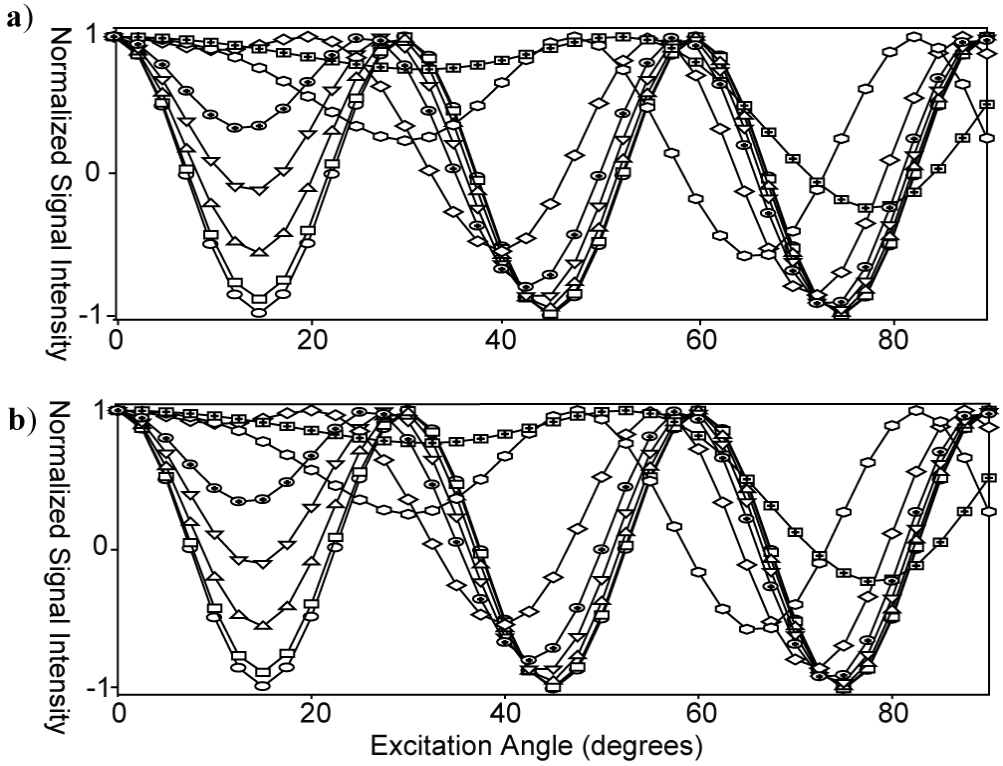

Figure 46 Simulation of the Direct DIVAM sequence illustrating the behaviour of the isotropic offset term in the Hamiltonian using real pulses under a) rotor-synchronized and b) non-rotor synchronized conditions. Each Hamiltonian term was varied between 1 to 50 kHz, where ○ 1000 Hz, □ 2500 Hz, △ 5000 Hz, ▽ 7500 Hz, ⊕ 10000 Hz ◇ 15000 Hz, ⬡ 25000 Hz, and ⊞ 50000 Hz. These simulations used a pulse width of 2.5 μs and an inter-pulse delay of 1.67 μs. The rotor synchronized and non-rotor synchronized simulations used MAS rates of 20 kHz and 25 kHz, respectively.

II. The Chemical Shift Anisotropy Term

Simulations with the CSA term (H^{aniso}) (figure 47) predict very different nutation behaviour than the isotropic term. Most of the first nutation cycle is insensitive to the size of the CSA interaction until the first maximum is reached, at 30^{o}, where the z-magnetization can be seen to be significantly reduced for values greater than 25 kHz. Beyond this point the amplitude of nutation remains attenuated until the end of the third cycle. These nutation curves show that selection is possible by the CSA term for values greater than 25 kHz as the first zero-crossing shifts to larger excitation angles. This implies that for the ^{19}F nucleus a minimum difference in CSA of 50 ppm is required for selection via the CSA term, which is not a severe restriction in many applications.

The long and short time series of Direct DIVAM (figures 44 and 45) illustrate that the observed spectrum is sensitive to the rotor synchronization conditions of the sequence. This behaviour resurfaces when comparing the rotor synchronized and non-rotor synchronized simulations presented in figure 47a and 47b, respectively. The CSA Hamiltonian contains an orientation term which results in signal modulations due to sample rotation, or the rotor phase. In this case, the nutation behaviour of the two figures is similar; however, a few key observations can be made. For selection to occur in the non-rotor synchronized case, a CSA value greater than or equal to 50 kHz is required and the nutation amplitude beyond the first cycle is reduced. Note that at low excitation angles the selection behaviour is undermined, as there is less variation in the zero-crossing point with increasing CSA values; therefore, for optimum selection performance it would be best to employ rotor synchronization.

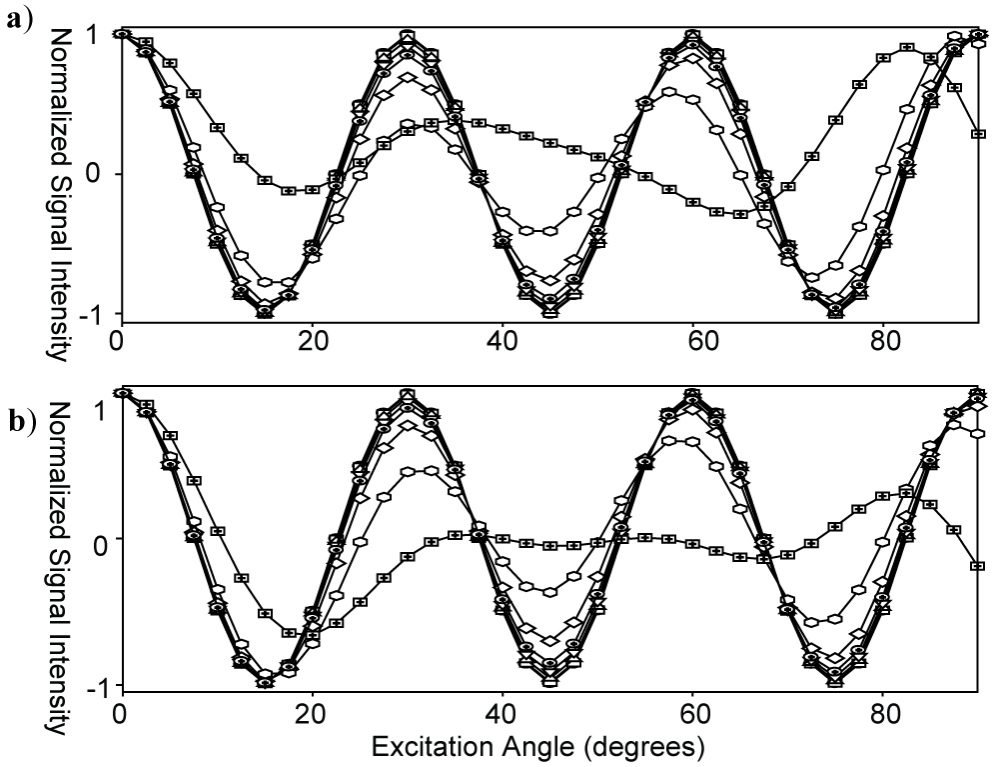

Figure 47 Simulation of the Direct DIVAM sequence illustrating the behaviour of the CSA term in the Hamiltonian using real pulses under a) rotor-synchronized and b) non-rotor synchronized conditions. Each Hamiltonian term was varied between 1 to 50 kHz, where ○ 1000 Hz, □ 2500 Hz, △ 5000 Hz, ▽ 7500 Hz, ⊕ 10000 Hz ◇ 15000 Hz, ⬡ 25000 Hz, and ⊞ 50000 Hz. These simulations used a pulse width of 2.5 μs and an inter-pulse delay of 1.67 μs. The rotor synchronized and non-rotor synchronized simulations used MAS rates of 20 kHz and 25 kHz, respectively.

The rotor synchronization dependency of the nutation behaviour was further explored. SIMPSON simulations were performed using real pulses for a large and a small CSA value over a series of inter-pulse delays at a spinning speed of 20 kHz (Figure 48). Rotor synchronization takes place near $\tau = 3$ μs, which corresponds to a $T_F = 48$ μs. A maximum difference between the signal intensity of the two curves is seen at $\theta = 15^o$; furthermore, a zero crossing for the 25 kHz curve occurs between $\theta = 7.5^o$ and $\theta = 10^o$, indicating the optimum selection conditions. Notice that these initial selection conditions remain favorable for most inter-pulse delays, suggesting that rotor synchronization, with

respect to T_F, is less important for small excitation angles. Later, at an excitation angle of 57.5°, the 90 kHz curve passes through a null state while the 25 kHz curve has significant positive intensity, indicating another important selection condition. This second selection condition shifts to a smaller excitation angle when shorter inter-pulse delays are used, but is not lost. When looking at inter-pulse delays longer than 3μs this selection condition is compromised and selection is no longer achieved. This suggests that rotor synchronization is essential when considering selection conditions at large excitation angles.

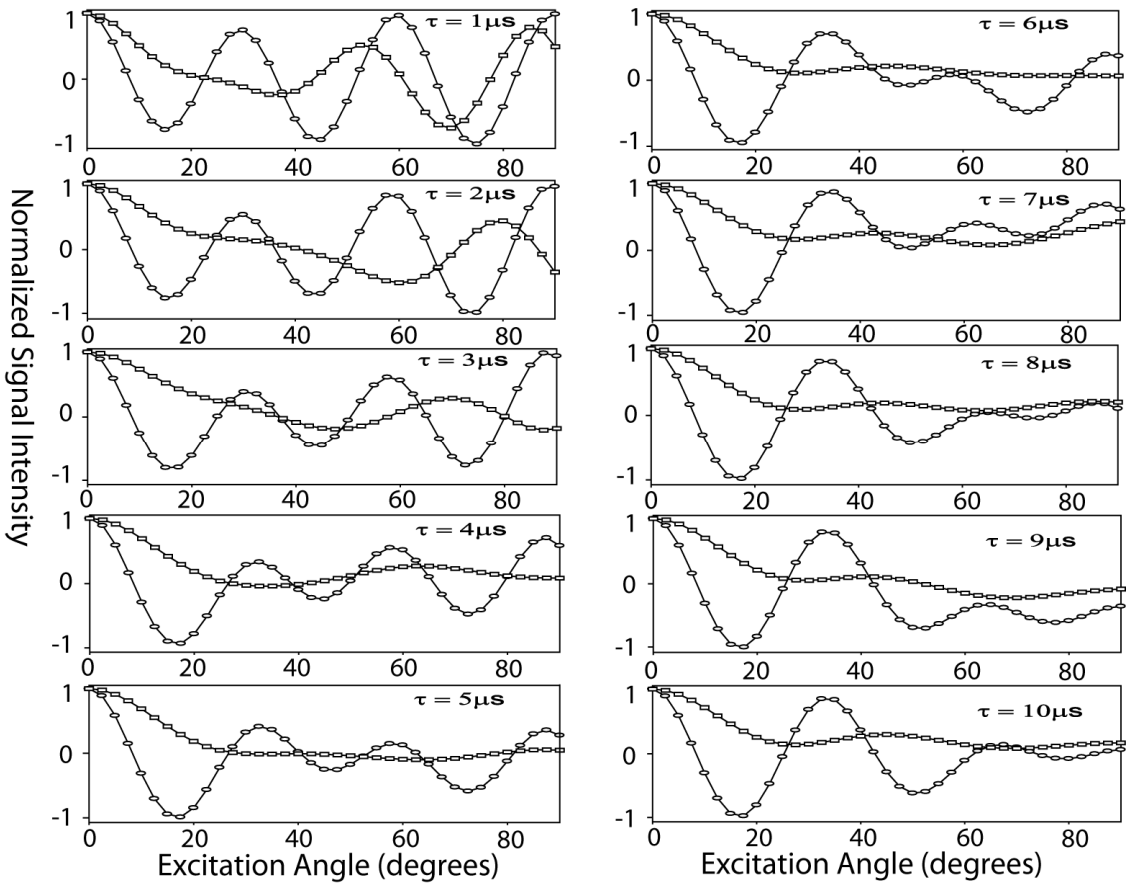

Figure 48 The effect of rotor-synchronization on the selectivity of the Direct DIVAM pulse sequence for various CSA and inter-pulse delay values, using real pulses where ◯= 25 kHz and □ = 90 kHz. A MAS rate of 20 kHz and a pulse width of 1 μs were used.

III. The Dipolar Coupling Term

The nutation curves corresponding to the dipolar term (H^{dip}) (figure 49) have similarities to the curves of both the isotropic and CSA terms; however, when the dipolar interaction reaches 50 kHz the first zero-crossing shifts to an excitation angle much larger than what was seen for the CSA term (figure 47). Furthermore, much like the isotropic term the amplitude of oscillation after the first minimum, at 15^{o}, decreases as the dipole couplings increase. Note that in order to achieve selection a dipolar interaction of at least 25 kHz is required. For fluoropolymer systems dipolar couplings of this size are uncommon, consequently the dipolar term is not expected to have a significant impact on the selection behaviour. Alternatively, the dipolar term can play a significant role in domain selection in materials with much less internal mobility where larger dipolar couplings would be expected between strong abundant spins. When the Direct DIVAM sequence is not rotor synchronized the dipolar term, just like the CSA term, is less likely to cause selection as the zero-crossing points are more closely spaced than for the rotor synchronized case. In this case (figure 49b), a dipolar coupling of at least 50 kHz is required in order to lead to selection.

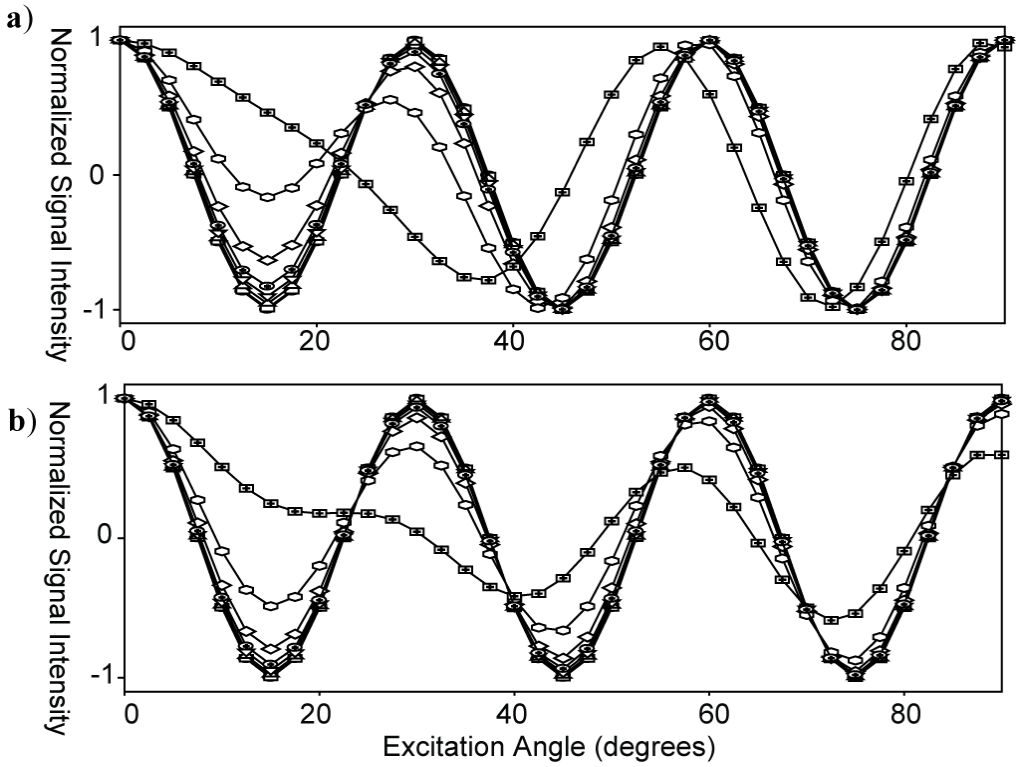

Figure 49 Simulation of the Direct DIVAM sequence illustrating the behaviour of the dipolar coupling term in the Hamiltonian using real pulses under a) rotor-synchronized and b) non-rotor synchronized conditions. Each Hamiltonian term was varied between 1 to 50 kHz, where ○ 1000 Hz, □ 2500 Hz, △ 5000 Hz, ▽ 7500 Hz, ⊕ 10000 Hz ◇ 15000 Hz, ⬡ 25000 Hz, and ⊞ 50000 Hz. These simulations used a pulse width of 2.5 μs and an inter-pulse delay of 1.67 μs. The rotor synchronized and non-rotor synchronized simulations used MAS rates of 20 kHz and 25 kHz, respectively.

Figure 50 shows a series of simulations of the dipole term over a range of inter-pulse delays for three dipole-coupling values. These bare a close resemblance to the corresponding simulations for the CSA term. Rotor synchronization takes place near $\tau = 3$ μs, which corresponds to $T_F = 48$ μs and optimum discrimination is seen for the 10 and 90 kHz curves at the excitation angle of $\theta = 15^o$. Again, rotor synchronization is seen to be less important for a T_F larger than one rotor period. On one hand, for all delay times considered, very little selection could be attained between the 10 and 25 kHz curves at the first zero crossing. One the other hand, these simulations do suggest that selection

between these two curves could take place for larger excitation angles, such as $\theta = 30^o$ and $\theta = 60^o$, and for larger delays, *ca* τ = 7-10 μs. Currently the DIVAM sequence is typically implemented with short delay times, consequently the dipole term cannot be expected to have a significant effect on the selection process.

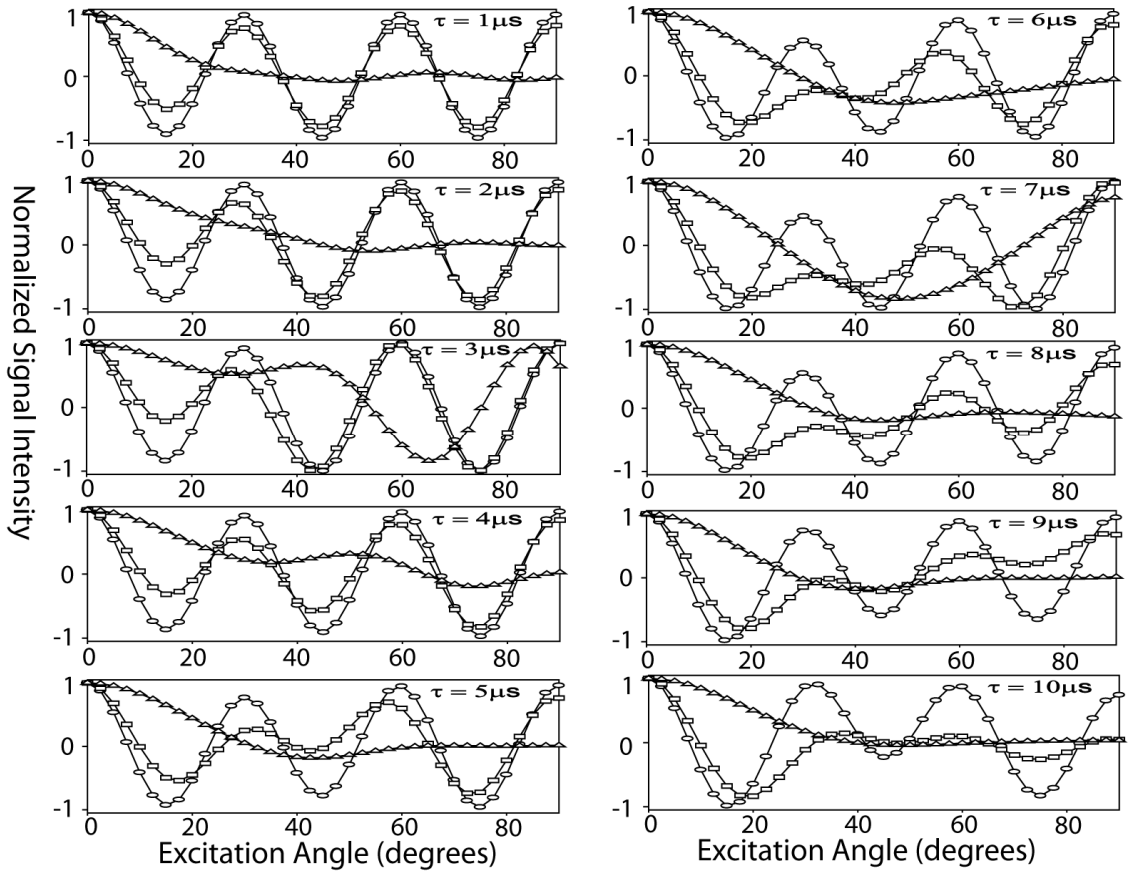

Figure 50 The effect of rotor-synchronization on the selectivity of the Direct DIVAM pulse sequence for various dipolar coupling and inter-pulse delay values, using real pulses where ○ = 10 kHz, □ = 25 kHz, and △ = 90 kHz. A MAS rate of 20 kHz and a pulse width of 1 μs were used.

2.4.3 Analytical Expressions

To describe the nutation behaviour with respect to excitation angle and inter pulse delay time, while including the effects of relaxation, a one-spin-evolution-relaxation model was invoked. In this case a pulse is implemented as a rotation by θ about the x-axis, chemical shift evolution as a rotation about the z-axis by ω, where $\omega = 2\pi\Delta\nu\tau$, and transverse relaxation as a simple exponential decay at a rate of $1/T_2$. The z-components at the end of the N-th pulse-evolve-relax cycle can be shown to be of the form:

$$A(\theta, \omega, T_2, t) = \sum_{n}^{N} A_n^N(\theta, \omega, t) \exp(-n\, t/\, T_2) \tag{104}$$

The coefficients, A, for a pulse train with N pulses are of the form:

$$A_n^N = \begin{cases} C_n^N \cos^{N-2n}\theta \sin^2\theta \left[\sum_{2j \le n} P^{2n-2-j}(\cos\theta) \cos^{n-2j}\omega t \right] & N - 2n \ge 0 \\ C_n^N \theta \sin^2\theta \left[\sum_{2j \le n} P^{2n-2-j}(\cos\theta) \cos^{n-2j}\omega t \right] & N - 2n < 0 \end{cases} \tag{105}$$

where $P^i(\cos\theta)$ refers to an i-th order polynomial in cosθ, and C^N_n is a constant. Similar expressions can be found for the x and y components. For a twelve-pulse sequence (N=12) the coefficients are of the form:

$$
\begin{aligned}
A_0^{12} &= C_0^{12}\cos^{12}\theta\left(P^0(\cos\theta)\right)\\
A_1^{12} &= C_1^{12}\cos^{10}\theta\sin^2\theta\left(P^0(\cos\theta)\cos\omega t\right)\\
A_2^{12} &= C_2^{12}\cos^{8}\theta\sin^2\theta\left(P^1(\cos\theta)+P^2(\cos\theta)\cos^2\omega t\right)\\
A_3^{12} &= C_3^{12}\cos^{6}\theta\sin^2\theta\left(P^3(\cos\theta)\cos\omega t+P^2(\cos\theta)\cos^3\omega t\right)\\
A_4^{12} &= C_4^{12}\cos^{4}\theta\sin^2\theta\left(P^4(\cos\theta)+P^5(\cos\theta)\cos^2\omega t+P^6(\cos\theta)\cos^4\omega t\right)\\
A_5^{12} &= C_5^{12}\cos^{2}\theta\sin^2\theta\left(P^6(\cos\theta)\cos\omega t+P^7(\cos\theta)\cos^3\omega t+P^8(\cos\theta)\cos^5\omega t\right)\\
A_6^{12} &= C_5^{12}\sin^2\theta\left(P^7(\cos\theta)+P^8(\cos\theta)\cos^2\omega t+P^9(\cos\theta)\cos^4\omega t+P^{10}(\cos\theta)\cos^6\omega t\right)\\
&\vdots \qquad \vdots \qquad \vdots \qquad \vdots \qquad \vdots \qquad \vdots\\
A_{12}^{12} &= 0
\end{aligned}
$$

(106)

These expressions were implemented in MAPLE® in order to reproduce the relaxation and the spin dynamics contributions to the nutation of behaviour. Figure 51 shows the nutation curves when considering only the effect of relaxation. The transverse relaxation time was varied from 1 to 10^5 μs and an inter-pulse delay time of 6 μs was employed. Notice that for slow relaxation rates, *ca.* T_2 = 0.1 s, the signal nutates as cos(12θ), which is seen experimentally for the amorphous signal (see Figure 43). As the relaxation rate increases, the amplitude of nutation decreases leading to the eventual loss of the signal at large excitation angles, which is observed for T_2 = 1 μs. This loss of signal is due to the saturation effect mentioned earlier in the long time series of Direct DIVAM. Also note that a difference in relaxation times of 30 μs results in a significantly different nutation curve, as seen between the 30 and 60 μs curves. There is a difference of approximately 170 μs between the relaxation times of the crystalline and amorphous domains; therefore, relaxation can be expected to drive the selection between the two curves for small excitation angles, as seen experimentally in figure 44.

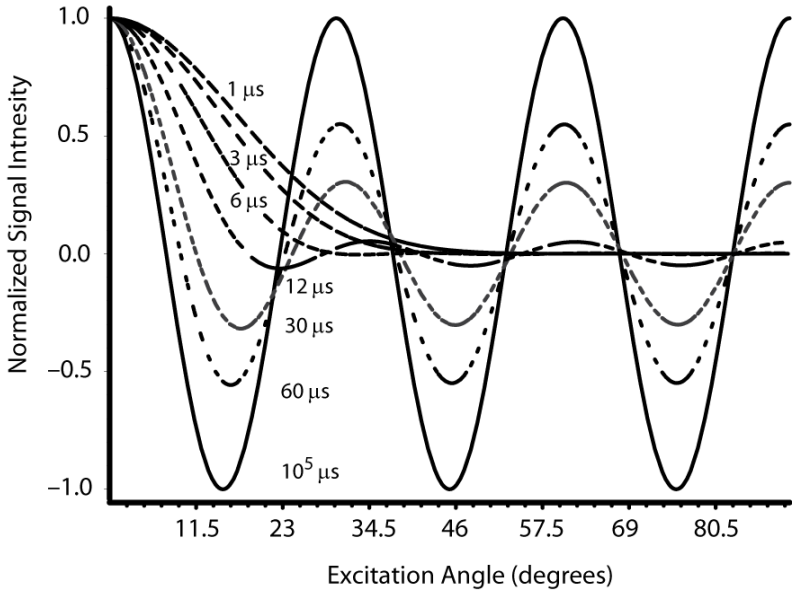

Figure 51 Maple simulations of the direct DIVAM sequence illustrating the effect of transverse relaxation on the nutation behaviour of the z-magnetization at the end of the sequence.

A few of the nutation curves from figure 51 were decomposed into their components, A^{12}_n, and are shown in figure 52. For clarity, only four components were plotted at a time; therefore, the top represents A_0 to A_3; the middle, A_4 to A_7; and the bottom A_8 to A_{11}. As the relaxation rate increases the contribution from the higher order terms decreases. In addition, as the excitation angle increases the saturation effect is more pronounced. Therefore, for very short relaxation times the zero-order term dominates and leads to a $\cos^{12}(\theta)$ dependence in the curve. Also note that the shape of these curves do not change with T_2, only their relative contributions do. These expressions predict that there will be different nutation behaviour between components with differing relaxation rates.

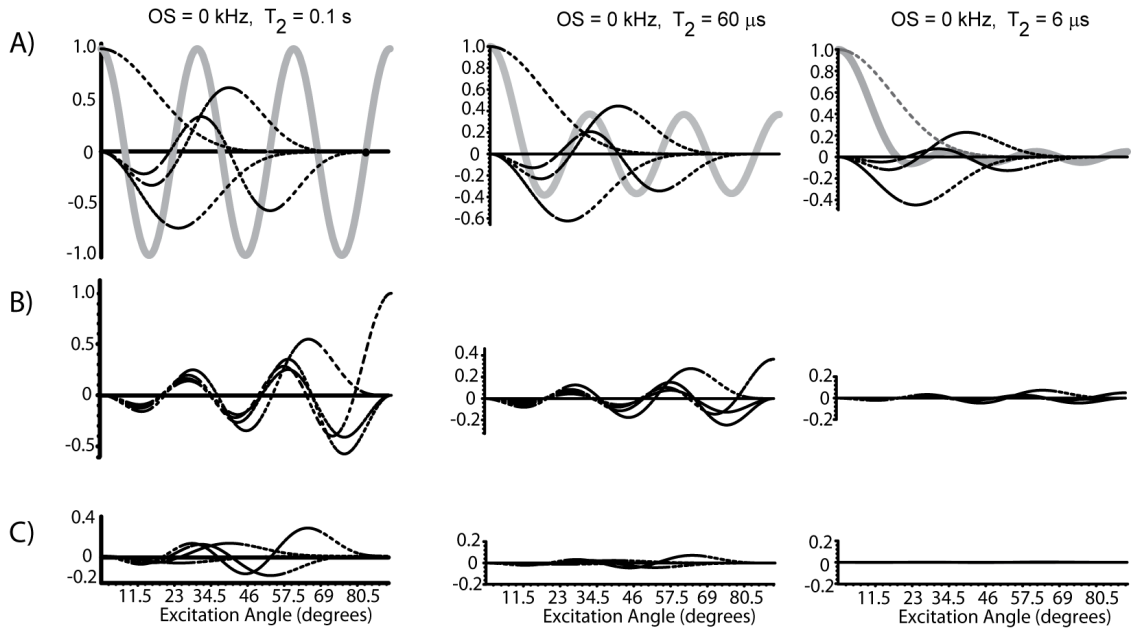

Figure 52 Selected nutation curves from the Maple simulations of the direct DIVAM sequence, considering only transverse relaxation, decomposed into components A) A_0-A_3, B) A_4-A_7, and C) A_8-A_{11} for T_2 = 0.1 s, 60 μs, and 6 μs. The grey curves illustrate the total nutation curve.

Figure 53 shows the results of the analytical expression when considering only the effects of an isotropic chemical shift. The shift was varied from 0 to 50 kHz while the inter-pulse delay was fixed at 6 μs. The behaviour in this case is very different, where both the amplitudes and frequencies of nutation are affected by the chemical shift interaction. Upon increasing the chemical shift, the amplitude of the first nutation cycle decreases, and is eventually lost; however, it recovers at higher excitation angles. As the isotropic chemical shift becomes large the oscillation rate decreases and eventually stops. Notice that these curves are identical to those obtained via the Simpson simulations of the isotropic offset term (see spin dynamics section above).

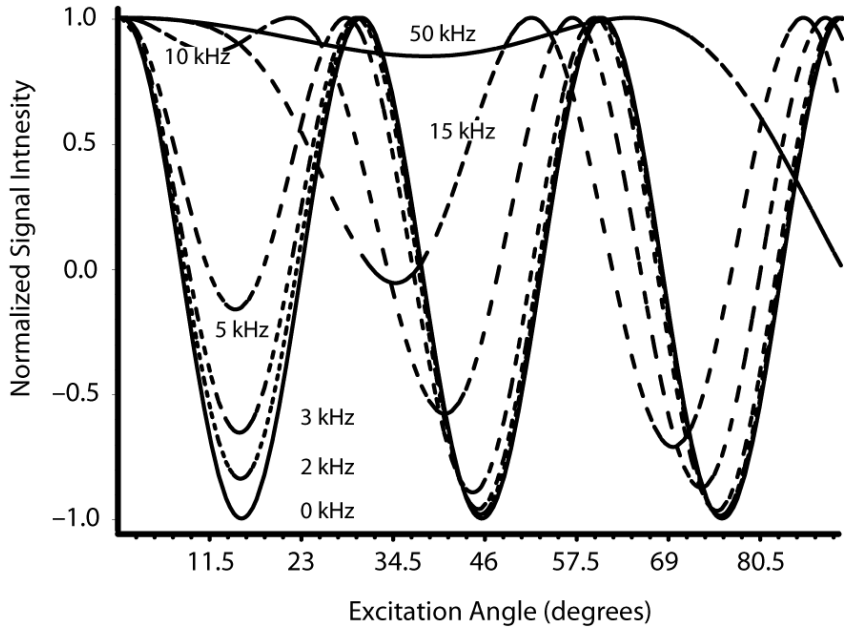

Figure 53 Maple simulations of the direct DIVAM sequence illustrating the effect of an isotropic chemical shift on the nutation behaviour of the z-magnetization at the end of the sequence.

A few of the curves from figure 53 were chosen and decomposed into their components (A_n) (figure 54). Notice that the contribution from each curve does not change substantially upon increasing the chemical shift; however, their shapes change dramatically. This illustrates that with each pulse-delay cycle a new component is added to the z-magnetization that has a unique dependence on the excitation angle. This is a consequence of the chemical shift evolution during the inter-pulse delay. In contrast to the relaxation only case, the higher order terms are essential in reproducing the correct shape of the nutation curves, especially at the higher excitation angles. These terms are the result of residual transverse components which, unless dephased by the end of the sequence, will lead to significant phase distortions in the spectra at larger excitation angles. These phase distortions are observed in the experimental Direct DIVAM arrays

for PVDF when short inter-pulse delays and large excitation angles are used (see figure 43).

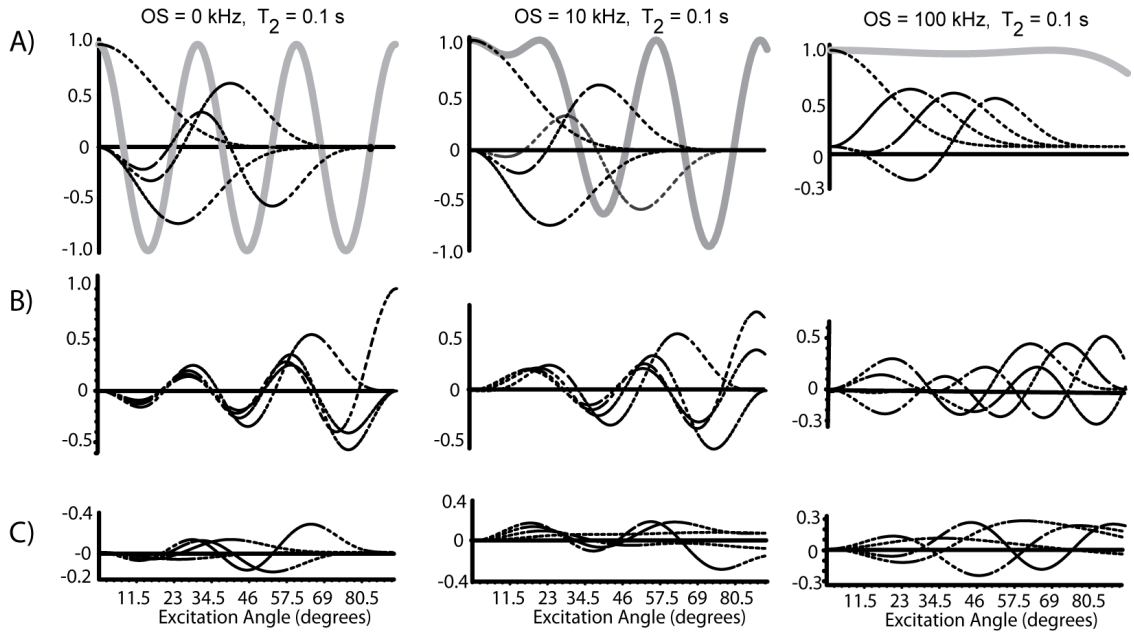

Figure 54 Selected nutation curves from the Maple simulations of the direct DIVAM sequence, considering only the isotropic chemical shift term, decomposed into components A) A_0-A_3, B) A_4-A_7, and C) A_8-A_{11} for $\Delta\upsilon$ = 0, 10, and 100 kHz. The grey curves illustrate the total nutation curve.

It is much easier to explain the role that both spin dynamics and relaxation have on the transverse component of the magnetization if the analytical expression presented in equation 104 is limited to two pulse-delay cycles. In this case $\mathbf{I}_z$ will undergo the following transformation:

$$\begin{aligned}\mathbf{I}_z \xrightarrow{\theta_x-\tau-\theta_x-\tau} & \mathbf{I}_z[\cos^2\theta-\sin^2\theta\cos\omega t\exp(-\tau/T_2)] \\ & +\mathbf{I}_x\sin\theta e\exp(-\tau/T_2)\sin\omega t\{\cos\theta[1+\cos\omega t\exp(-\tau/T_2)]+\cos\omega t\exp(-\tau/T_2)\} \\ & +\mathbf{I}_y\sin\theta e\exp(-\tau/T_2)\{-\cos\theta\cos\omega t[1+\cos\omega t\exp(-\tau/T_2)]+\sin^2\omega t\exp(-\tau/T_2)\}\end{aligned} \quad (107)$$

Recall that ω is a periodic function in time that depends on crystallite orientation with respect to the magnetic field, which can be stated in the general form:

$$\omega(t,\alpha,\beta,\gamma) = \omega_o + \omega_1(\alpha,\beta)\cos(\omega_r t + \gamma) + \omega_2(\alpha,\beta)\cos(2\omega_r t + \gamma) \qquad (108)$$

where: α, β and γ are the Euler angles defining the crystallite orientation; ω_R is the spinning rate; ω_o is the isotropic frequency; and ω_1 and ω_2 are dependent on the chemical shift and dipolar tensors according to expressions given elsewhere[121].

On the extreme end of the long time scale all of the exponential terms disappear, and thus the transverse components can be removed, leaving the following expression for the longitudinal component:

$$\mathbf{I_z} \xrightarrow{\theta_x - \tau - \theta_x - \tau} \mathbf{I_z}\cos^2\theta \qquad (109)$$

This is the expression for the nutation behaviour when relaxation dominates and the signal should be expected to saturate with increasing excitation angle and inter-pulse delay, as is observed experimentally in figure 45. Note that the chemical shift term is no longer present and as a result no transient behaviour is expected on the rotor time scale.

On an intermediate time scale, the first order exponentials are retained while the second order terms are removed, resulting in the following expression:

$$\begin{aligned} \mathbf{I_z} \xrightarrow{\theta_x - \tau - \theta_x - \tau} & \mathbf{I_z}[\cos^2\theta - \sin^2\theta\cos\omega t\exp(-\tau/T_2)] \\ & + \mathbf{I}_x\sin\theta\cos\theta\sin\omega t\exp(-\tau/T_2) \\ & - \mathbf{I}_y\sin\theta\cos\theta\cos\omega t\exp(-\tau/T_2) \end{aligned} \qquad (110)$$

In this case more complex behaviour is predicted and is indeed observed. In the case of small excitation angles, *ca* 15° or less, $\sin^2\theta$ can be considered small enough to be ignored. As a result, the second term of the longitudinal component falls away leaving only a $\cos^2\theta$ dependence, as seen for extremely long delay times. In the vicinity of θ = 15°, the $\sin^2\theta$ term can no longer be considered negligible; however, the second term is further reduced owing to its $\exp(-\tau/T_2)$ dependence. The transverse components of

equation 107 can also be ignored for small excitation angles, as they depend on sinθ, and are also further attenuated by relaxation due to their exp(-τ/T_2) dependence. It appears as though relaxation will dominate the selection mechanism for intermediate inter-pulse delays and small excitation angles. In this case, no transient oscillations are predicted with sample rotation, as the ω term has been reduced greatly, and as a result no phase distortions should be observed. This behaviour is indeed observed experimentally for angles up to 15^o for both time series (figure 44 and 45), as the small angle approximation (outlined above) also holds true in the case of the short time scale.

For excitation angles greater than 15^o, on the intermediate time scale, the approximations outlined above begin to break down and the full expression in equation 109 has to be considered. The resulting longitudinal component is made up of two terms: the first term originates from the initial longitudinal component, which is time independent; and the second term is derived from the transverse magnetization, which has a time dependence determined by both T_2 and the isotropic chemical shift. The second term accounts for the recovery observed in the signal with increasing delay time (figure 45) for intermediate angles where the signal only partially saturates. The second term decreases in magnitude with increasing τ resulting in a net increase in the signal intensity on the time scale determined by the transverse relaxation rate, eventually leading to the form seen in equation 106.

The recovery behaviour, observed experimentally (figure 45), is reproduced using the analytical expressions where the longitudinal component was computed as a function of log τ for a long (L, typical of the amorphous domain) and short (S, typical of the crystalline domain) transverse relaxation time, covering delay times from 1 μs to 10 ms

(figure 55a). As the delay time increases the effects of relaxation emerge, causing the net rotation to appear to decrease by the start of the long time scale. When the relaxation effect becomes more pronounced the signal eventually returns to an intensity reflecting the saturated state, defined by $\cos^{12}\theta$; thus, for larger angles the signal is lost to saturation. For the long relaxation time (L), covering the entire time range, the calculations predict: i) at 2.5^o, there is little net rotation at the start of the long time scale and hence no recovery is expected; ii) at 15^o there is a large net rotation, approaching 120^0 at the start of the long time scale, allowing for significant recovery to an intensity of $\cos^{12}(15^o) = 0.66$; iii) at 30^o, there is a net rotation near 300^o at the start of the long time scale, which by the end reaches an intensity of $\cos^{12}(30^o) = 0.18$, reflecting significant saturation; and iv) at 45^o, it experiences a net rotation near 480^o at the beginning of the long time scale and remains almost completely saturated until the end, with an intensity of 0.015 . For the more rapidly relaxing component the same behaviour is seen but shifted to a time scale commensurate with the difference in relaxation rates. As a result, for relaxation times typical of the crystalline domain and over much of the long time scale, the signal has already recovered to its fullest extent at each excitation angle considered; hence, a less pronounced change in intensity is observed (as seen in figure 45). The saturation effects outlined above can be seen in the shaded region of figure 55a.

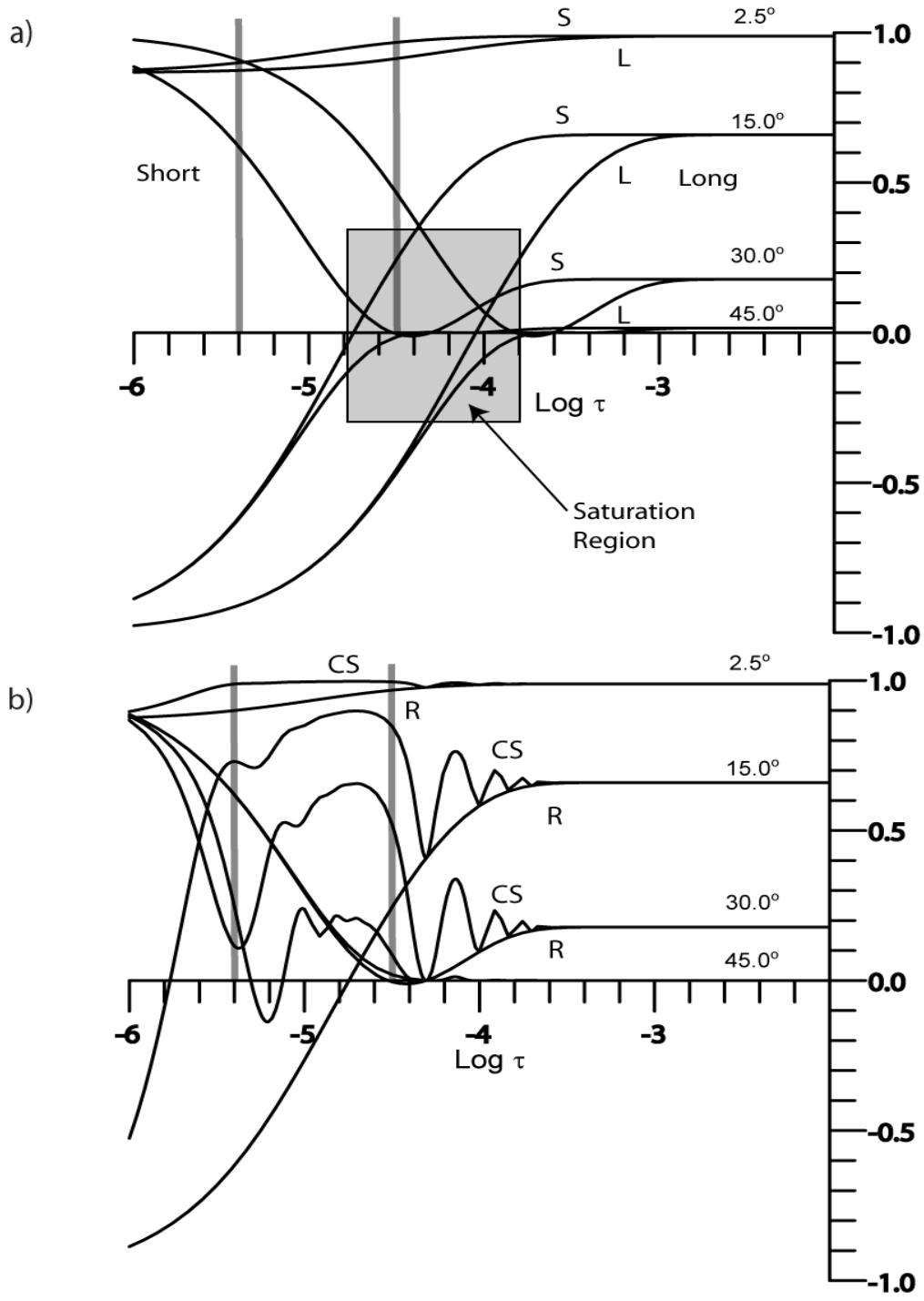

Figure 55 Maple simulations of the direct DIVAM sequence illustrating the effect of spin-spin relaxation rates over the long and the short delay time regimes for selected excitation angles corresponding to figures 43 and 44. The longitudinal magnetization remaining after the DIVAM filter is compared for a long (L), 250 μs, and a short (S), 50 μs, spin-spin relaxation time.

For the short to intermediate time scales, and for angles greater than 15°, equation 104 predicts transient oscillations determined by the rotor period. These are observed on the short time scale (figure 44) where the following expression holds:

$$\begin{aligned}\mathbf{I_z} \xrightarrow{\theta_x-\tau-\theta_x-\tau} & \mathbf{I_z}[\cos^2\theta - \sin^2\theta\cos\omega t] \\ & + \mathbf{I}_x \sin\theta\sin\omega t[\cos\theta(1+\cos\omega t)+\cos\omega t] \\ & + \mathbf{I}_y \sin\theta[-\cos\theta\cos\omega t(1+\cos\omega t)+\sin^2\omega t]\end{aligned} \qquad (111)$$

When the delay period is rotor synchronized normal nutation behaviour is predicted, including the effect of the isotropic frequency, as in figure 46. Otherwise, the intensity of the signal will depend on rotor phase, giving rise to oscillations in the signal intensity as seen in the short time series (figure 44) and illustrated in figures 48 and 50 for the CSA and dipolar simulations, respectively. Figure 55b shows a set of simulations produced from the analytical expressions in which the effect of both the isotropic chemical shift and relaxation are included. The signal modulations observed for the excitation angles of 15° , 30°, and 45° are dominated by the chemical shift term over the short time scale and this behaviour persists into the beginning of the long time scale, *ca.* log τ = –5.5 - –4. The same behaviour is seen experimentally for excitations angles of 30° and larger where the crystalline signal exhibits similar dynamics (figure 45).

It is important to note that equation 110 predicts the emersion of phase distortions in the spectra for angles greater than 15° and short delays. This is the result of the transverse components being neither dampened by the sinθ term nor dephased by transverse relaxation. The phase distortions predicted by these remaining transverse terms are observed experimentally where at large angles the nutation behaviour is seen to be compromised (figure 43). These phase distortions are also seen in the short time series (figure 44) for angles greater than 30°. New methods need to be developed that

will remove these phase distortions such that DIVAM may be utilized for large angles and short delays.

2.4.4 Selection Mechanism

Direct DIVAM experiments performed with varying inter-pulse delays over different time scales show transient behaviour on the sample spinning time scale that was not seen in the CP DIVAM experiment. This combined with the presence of significant phase distortions at large excitation angles indicates that the effects of spin dynamics must be considered when explaining the selection mechanism of Direct DIVAM. Spin dynamic simulations show that all three terms in the Hamiltonian, isotropic offset (H^{iso}), CSA (H^{aniso}), and dipolar coupling (H^{dip}), can give rise to selection behavior. They predict that the isotropic chemical shift term will dominate the selection mechanism; however, in the absence of a significant isotropic chemical shift the selection mechanism will be dominated by the CSA term. The long time scale experiments (figure 45) show that when a large inter-pulse delay is used the selection mechanism is driven by the transverse relaxation, while the short time scale experiments (figure 44) showed no transient behaviour for small excitation angles, *ca. less than 30* ^{o}, indicating that the selection mechanism for these angles must also be driven by relaxation. In the case of large excitation angles, for a short and intermediate inter-pulse delay, the selection mechanism appears to be dominated by spin dynamics. In addition, the set of analytical expressions developed to include the effects of relaxation support all of the above statements. Therefore, the Direct DIVAM sequence appears to have two modes of operation, where the method of selection can be switched between relaxation and spin

dynamics; however, in order to use the later method of selection the aforementioned phase distortions at large excitation angles must be removed. This requires modifications to the Direct DIVAM sequence and the resulting sequence is known as Refocused DIVAM.

3. THE REFOCUSED DIVAM SEQUENCE

3.1 Overview

In section 2.4 it was shown that the nutation of the ^{19}F signals from PVDF during the Direct DIVAM sequence is seen to be strongly dependent on the sample spinning rate. Both relaxation and coherent spin dynamics were seen to participate in the selection process where the degree of each was dependant on the excitation angle and inter-pulse delay used; therefore, it is possible to configure the sequence so that either can be the dominant selection mechanism. The spin dynamics terms were shown to lead to significant phase distortions for large excitation angles (θ). Also, the nutation behaviour depended strongly on the frequency offset from the RF resonance, or carrier frequency, of the excitation pulses (Henceforth, this will be referred to as the offset dependence of Direct DIVAM). Both phase distortions and an offset dependence are undesirable as they can severely compromise effective domain selection by distorting the observed nutation behaviour; therefore, modifications to Direct DIVAM are required in order to remove, or reduce, these effects.

At this stage it is important to point out that although Direct DIVAM bears a strong resemblance to the DANTE sequence[122-123] used in solution-state NMR, it is very different in its application and mode of action. On the one hand, DANTE can be thought of as a discrete version of a soft pulse, where selective excitation is achieved through the offset term. The effects of the remaining terms in the Hamiltonian are usually ignored and have not seen significant attention in potential NMR applications. DIVAM on the other hand is used solely on solids to select between overlapping signals; hence, the offset differences are very small. This means that a combination of relaxation and spin dynamics due to the remaining terms of the solid state NMR hamiltonian (CSA, DC) are

responsible for the selection behaviour. In fact, the intention of Refocused DIVAM is to completely remove any remaining evolution that result from the offset term during the Direct DIVAM sequence.

The Refocused DIVAM experiment (figure 56) is similar to Direct DIVAM, but with the addition of refocusing pulses and an appropriate phase cycle.

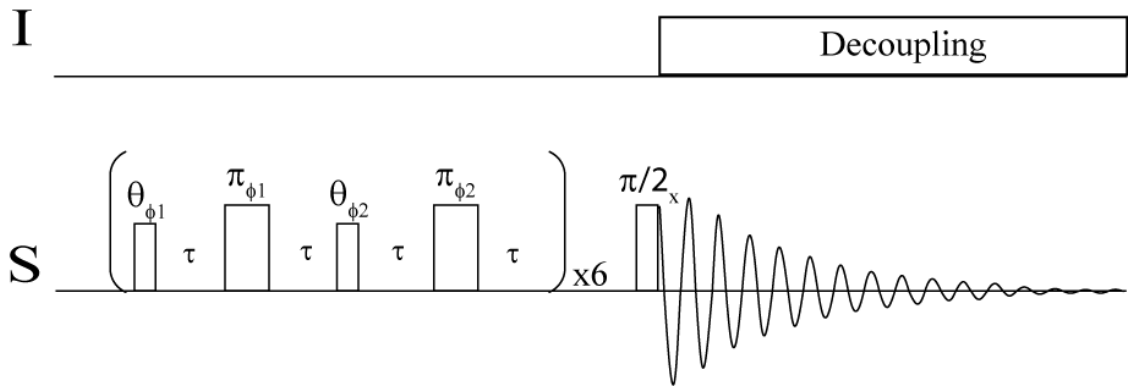

Figure 56 The Refocused DIVAM pulse sequence.

The refocusing pulses are added to remove the effect of coherent dephasing due to linear terms, which include the isotropic chemical shift, of the Hamiltonian during the inter-pulse delay; thereby reducing both the phase distortions seen at large excitation angles (θ) and the offset dependence of Direct DIVAM. The phase cycle (given in table 3) is implemented to ensure that the magnetization accumulates in the transverse plane in a similar manner to the previous DIVAM experiments, as shown in Figure 57.

Table 3 The phase cycle of the Refocused DIVAM sequence.

$\theta_{\phi 1}$	$\pi_{\phi 1}$	$\theta_{\phi 2}$	$\pi_{\phi 2}$	$\theta_{\phi 1}$	$\pi_{\phi 1}$	$\theta_{\phi 2}$	$\pi_{\phi 2}$
X	Y	(-X)	(-Y)	Y	Y	Y	(-Y)
X	(-Y)	(-X)	Y	Y	(-Y)	Y	Y
X	X	X	(-X)	Y	X	(-Y)	(-X)
X	(-X)	X	X	Y	(-X)	(-Y)	X
(-X)	X	(-X)	(-X)	(-Y)	Y	(-Y)	(-Y)
(-X)	(-X)	(-X)	X	(-Y)	(-Y)	(-Y)	Y
(-X)	Y	X	(-Y)	(-Y)	X	Y	(-X)
(-X)	(-Y)	X	Y	(-Y)	(-X)	Y	X

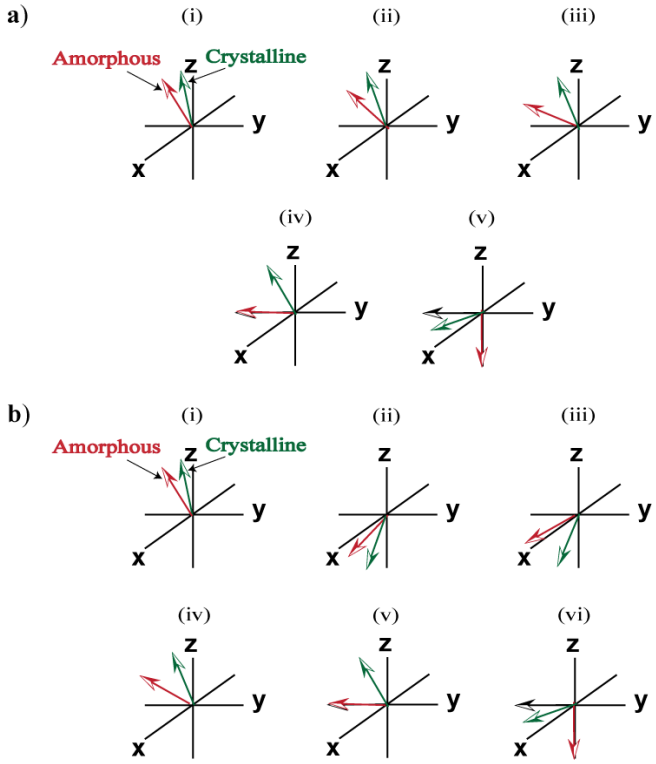

Figure 57 a) A vector diagram of magnetization from the two domains, with differing T_2 relaxation times, under the operation of the DIVAM pulse train illustrating the Magnetization after the:(i) 1st pulse-delay cycle, (ii) 2nd pulse-delay cycle, (iii) 3rd pulse-delay cycle, (iv) 12 pulse-delay cycles, and (v) the final $\pi/2$ pulse. b) A Similar diagram to above but for the Refocused DIVAM pulse train and its first phase cycle, illustrating the magnetization after the: (i) 1st θ_x-pulse and an inter-pulse delay, (ii) 1st π_y-pulse and an inter-pulse delay, (iii) 1st θ_{-x} -pulse and an inter-pulse delay, (iv) 1st π_{-y}-pulse and an inter-pulse delay, (v) full Refocused DIVAM train, and (vi) the final $\pi/2$ pulse.

The phase cycle also makes use of EXORCYCLE, discussed earlier in section 1.4.3, ensuring that any remaining contributions to the signal that result from the miss setting of 180 degree pulses are removed. The experiment is repeated with an offset alternating above and below the RF carrier frequency in order to ensure that any phase distortions due to the breakdown of the hard pulse approximation are minimized. This chapter provides experimental and simulation results that show how these modifications affect the selection mechanism of the Direct DIVAM sequence.

3.2 Experimental

The α-PVDF sample had a molecular weight of $1x10^6$D as determined by gel permeation chromatography (GPC), crystallinity of ~28% and reverse unit content of 4.7% as determined by NMR, and a melting point of 158 ^oC as determined by differential scanning calorimetry (DSC)[118-119]. The sample of α-PVDF was supplied by Atofina, France. The Nafion 117™ sample was purchased from Dupont in the form of a commercial fuel cell membrane film. All measurements were made on a VARIAN INOVA 500 MHz NMR spectrometer operating at a carrier frequency of 470.18 MHz for fluorine and 500.00 MHz for proton. A Varian 2.5 mm four channel HFXY probe operating at 21 ^oC and capable of MAS speeds up to 30 kHz was used. The 90^o pulse was calibrated at 2.5 μs for both ^{19}F and ^1H nuclei and corresponds to an RF strength of 100 kHz. The RF resonance frequency during acquisition was set to the amorphous peak of PVDF at –91.2 ppm, and is indicated in the figure captions for the Nafion experiments. TPPM decoupling was applied to ^1H during fluorine acquisition and also during spectral referencing so that the Bloch-Siegert shift could be neglected.[2] Spectral referencing was

done using C_6F_6 (δ_F = 166.4 ppm with respect to $CFCl_3$) and zirconium oxide rotors with vespel drive caps were used in order to avoid unwanted fluorine background signal.

All experimental measurements of the Refocused DIVAM sequence were implemented over a minimum of 32 transients to allow for the full phase cycling of the 180^o refocusing pulses. The phase cycle used (Table 3) ensures that all feed-through terms are suppressed and effective refocusing occurs.[59] Blocks of 32 transients are required because the normal 16 step phase cycle is run twice, but with a different pulse offset used in each full cycle. The two pulse offsets used are of equal magnitude but opposite sign. The pulse offset used for each experiment will be indicated in the figure caption. The pulse offset is only applied to the DIVAM pulse train; therefore, the terminal 90^o observation pulse is still applied on resonance with the amorphous peak of PVDF.

The Refocused DIVAM sequence was performed using a pulse train that consisted of twelve 2.5 μs (pulse width (pw_{90}) = 2.5 μs) pulses each followed by a 5 μs (pulse width (pw_{180}) = 5 μs) refocusing pulse, with all pulses separated by an inter-pulse delay (τ). After the pulse train a terminal 90^o observation pulse was applied. Measurements for the nutation series were made with the pulse excitation angle (θ) varied from 0^o to 90^o in 2.5^o steps and both the inter-pulse delay and magnitude of the pulse offset fixed. The variance of the pulse excitation angle (θ) was accomplished by altering the strength of the B_1 field, while keeping the pulse duration constant in order to attain rotor synchronization. The transient series measurements of Refocused DIVAM were run with both the magnitude of the pulse offset and excitation angle (θ) fixed, while varying the inter-pulse delay (τ). Similarly, the pulse offset series measurements were

run with both the inter-pulse delay (τ) and pulse excitation angle (θ) fixed, while varying the magnitude of the pulse offset. The discussion of rotor-synchronization will always be with respect to the total filtering time (T_F), where $T_F = (24 \times \tau) + (12 \times pw_{90}) + (12 \times pw_{180})$. All experimental measurements were implemented with an MAS rate between 20 and 25 kHz. The specific MAS rate used for each experiment is indicated in the figure captions.

All simulations were carried out using SIMPSON 1.1.0[69] with an Intel Core 2 Duo 7200 processor. The Refocused and Direct DIVAM simulations were run separately for three different terms in the Hamiltonian corresponding to the isotropic frequency, chemical shift anisotropy (CSA), and the dipolar coupling. For each of these terms the pulse sequence was simulated using real (soft) pulses and the strength of the Hamiltonian terms was varied in size from 0-50 kHz. These simulations were also run under timing conditions in which the total duration of the pulse train was or was not synchronized with the rotor period. An example of the SIMPSON input file used to simulate Refocused DIVAM can be found in Appendix 2.

The CSA and Isotropic terms of the Hamiltonian were simulated as a 1-spin system with the initial density matrix set as $\mathbf{I}_z$. The dipolar coupling term of the Hamiltonian was simulated as a 2-spin system with the initial density matrix set as $\mathbf{I}_z^{(1)} + \mathbf{I}_z^{(2)}$. At the end of the sequence the $\mathbf{I}_z$ component of the density matrix was reported as a function of the pulse excitation angle (θ). For the dipolar coupling simulations, only the $\mathbf{I}_z^{(1)}$ term of the density matrix was reported.

Simulations of the Refocused DIVAM sequence were implemented using the same pulse-train values as in the solid state NMR measurements (pw_{90} = 2.5μs and pw_{180}

= 5μs). The rotor-synchronized and non-rotor-synchronized simulations used a spinning speed of 20 and 25 kHz, respectively. All simulations used the direct method of calculation and were powder averaged with 30 gamma angles and set of 168 crystal orientations.

All NMR spectra were processed using the MatNMR[120] 3.9 processing toolbox (© Jakko van Beek) for MathWorks™ MATLAB® 6.5. The polymer chemical structure representations were created in CambridgeSoft® ChemDraw© Ultra 11.0.1. All figures were created with a combination of Adobe® Illustrator© CS4, Microsoft® Office Excel© 2007, and SigmaPlot® 2000 software.

3.3 Experimental Results

3.3.1. Nutation Behaviour

The Refocused DIVAM nutation array of the ^{19}F MAS NMR spectra of PVDF is shown in figure 58. The amorphous signal is seen to nutate at a faster rate than the crystalline signal, and passes through a null condition at $\sim \theta = 22.5^{o}$, where positive intensity of the crystalline signal remains. Also, the crystalline signal passes through a null condition at $\sim \theta = 62.5^{o}$, where the amorphous signal has returned to a positive intensity. Furthermore, the defect signals now nutate at a rate similar to that of the amorphous signal; this will be discussed further later. It is important to point out that these selection angles are approximate. To achieve complete selection of either the crystalline or amorphous domain one would have to increment the excitation angle in steps much smaller than 2.5^{o}.

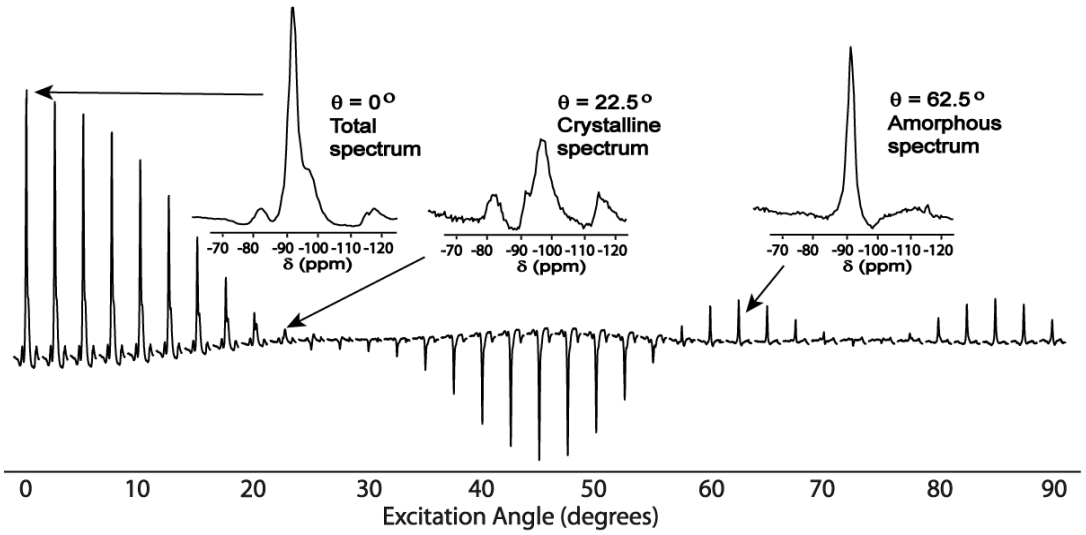

Figure 58 The Refocused DIVAM nutation array of the ^{19}F MAS NMR spectra of PVDF over a series of excitation angles with an inter-pulse delay of 2.5 μ, a 90^{o} pulse width of 2.5 μs, a 180^{o} pulse width of 5 μs (T_F = 150 μs), and a pulse offset of 1 kHz. The nutation array ranges over excitation angles of 0^{o}-90^{o} in steps of 2.5^{0} and was acquired with a spinning speed of 20 kHz. Enlargements of the ^{19}F MAS NMR spectra of PVDF for selected excitation angles are shown above the array.

When comparing the nutation behaviour in Refocused DIVAM (figure 58) with Direct DIVAM (figure 43), a few observation can be made. First, note that the phase distortions in the Direct DIVAM array have been reduced in the Refocused DIVAM experiment. Second, the signal from all three chemical environments nutate for all excitation angles indicating that the offset dependence of Direct DIVAM has been reduced. Lastly, Refocused and Direct DIVAM show differences in their overall rate of nutation, which can be attributed to three factors: 1) the inter-pulse delays used in Direct DIVAM differ from the Refocused DIVAM sequence; 2) the Refocused DIVAM sequence has 24 inter-pulse delay periods due to the addition of refocusing pulses; 3) the selection mechanisms of Direct and Refocused DIVAM are different. As a result of the first two factors, the total filtering time of the sequence is changed and the net evolution in the transverse plain is different; therefore differences in their nutation rates are to be

expected. The selection mechanism in Direct DIVAM, when off-resonance, becomes dominated by its offset dependence, while in Refocused DIVAM it appears to be driven primarily by the CSA term. This is further supported by SIMPSON simulations on Refocused DIVAM, which is discussed in Section 3.4.1.

Although, the offset dependence of Direct DIVAM has been greatly reduced, it can still be seen to a minor degree when comparing nutation rates of the amorphous and defect signals in Refocused DIVAM (Figure 58). These signals are known to be from similar environments and should have similar nutation rates; however, upon closer examination nutation of the defect signals lags slightly behind the amorphous signal. The extent of this remaining offset dependence will be examined further using Nafion 117™.

The ^{19}F MAS NMR spectra of Nafion 117™ and its structural assignment can be seen in Figure 59.[49, 124] Nafion provides an ideal case for testing the experimental extent over which the offset dependence of Direct DIVAM has been removed. The sidechain (SC) CF_3 and OCF_2 signals of Nafion (signal E and F, respectively, in figure 59b) have an isotropic chemical shift of ~40 ppm, or ~20 kHz, from the main backbone (BB) CF_2 signal (signal B in figure 59b). In addition, these signals are far enough removed from each other that simple nutation behaviour is expected for each signal, so long as Direct DIVAM is applied on-resonance with respect to the signal of interest. Figures 60a and 60b show the nutation profile of the backbone (BB) signal (B in figure 59) at –122 ppm, and side-chain (SC) signals (E and F in figure 59) at –82 ppm, with the RF resonance frequency centered on the backbone (BB) signals. Similarly, Figures 60c and 60d show analogous nutation profiles but with the RF resonance centered on the SC signal.

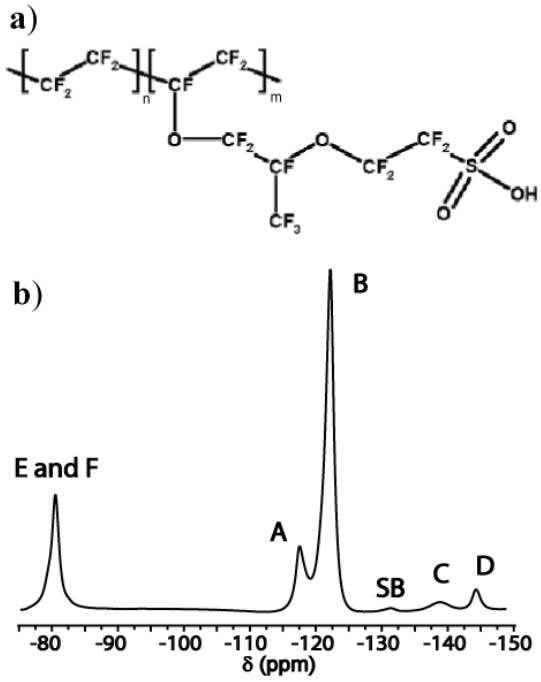

Figure 59 a) The polymer structure of Nafion 117™ and b) the ^{19}F MAS NMR spectra and structural assignment of Nafion 117™ under ambient conditions, with the RF resonance set on the backbone CF_2 peak, and a MAS rate of 24 kHz where: A = SCF_2, B = $(CF_2)_n$, C = CF (Backbone), D = CF (Side-chain), E = CF_3, F = OCF_2, SB = Spinning side band.

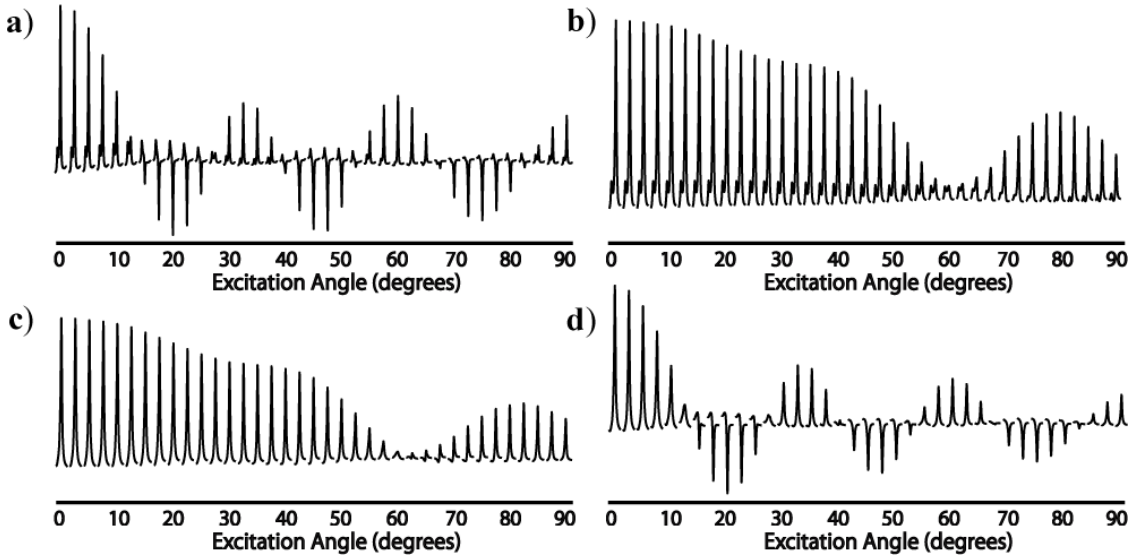

Figure 60 The ^{19}F Direct DIVAM nutation arrays of various peaks in Nafion with an MAS frequency of 24 kHz and ranging over excitation angles of 0^o-90^o in steps of 2.5^0.Each Direct DIVAM array used an inter-pulse delay of 1.67 μs and a pulse width of 4.44 μs (T_F = 83.3 μs). Array of the backbone CF_2 peak (a, c) and side-chain CF_3 and OCF_2 peaks (b, d), with the RF resonance centered on either the backbone CF_2 peak (a, b) or the side-chain CF_3 and OCF_2 peaks (c,d).

It is clear that nutation of each signal occurs only when the RF resonance is centered directly on the peak of interest (figures 60a and 60d) and that once the RF resonance is moved nutation is lost (figures 60b and 60c). This is a direct result of the aforementioned offset dependence of Direct DIVAM and will be further confirmed in section 3.4.1. Figure 61 illustrates the nutation profiles of the BB and SC signals in Nafion acquired using the Refocused DIVAM sequence and with the RF frequency centered at –100 ppm.

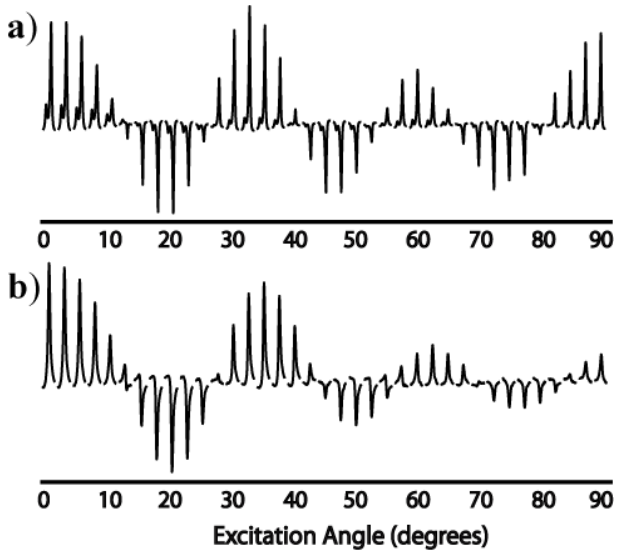

Figure 61 The ^{19}F Refocused DIVAM nutation array, at an MAS rate of 24 kHz and ranging over excitation angles of 0^o-90^o in steps of 2.5^0, of the a) backbone CF_2 peak and the b) side-chain CF_3 and OCF_2 peaks in Nafion with the RF resonance centered at –100 ppm for both arrays. An inter-pulse delay of 1.46 μs, a 90^o pulse width of 2.5 μs, a 180^o pulse width of 5 μs (T_F = 125 μs), and a pulse offset of 1 kHz were used.

Refocused DIVAM recovers nutation of both the SC and BB signals and has removed the frequency offset dependence over a range of at least ~±20 ppm (~±10 kHz). Figure 61 illustrates the increase in the effective frequency range of the Direct DIVAM sequence by the introduction of refocusing pulses. Earlier it was stated that the selection mechanism of Refocused DIVAM appears to be driven by the CSA term. This term has

an orientational dependence with respect to the static magnetic field and transient behaviour is expected on the rotor-time scale. This was investigated by carrying out a series of experimental measurements in which the inter-pulse delay was varied while both the pulse offset and excitation angle were fixed.

3.3.2. Transient Behaviour

Figure 62 illustrates the response of the ^{19}F spectra of PVDF for each of the selected excitation angles as the inter-pulse delay is varied such that the T_F ranges over approximately two rotor periods (τ_r) in steps of 3/50 τ_r (referred to as the short time series). It is important to note that the use of both a 100 Hz and 5 kHz pulse offset did not significantly change the observed transient behaviour (this will be shown later in section 3.6.1). Refocused DIVAM has been implemented using a 1 to 5 kHz pulse offset and the effect of using a pulse offset larger than 5 kHz will be discussed in section 3.6. Similarly to Direct DIVAM, very little to no variation is seen in the signal intensity with respect to the inter-pulse delay for the excitation angle of 2.5^o. In contrast, variations in the signal intensity with respect to inter-pulse delay, or the rotor phase, did not become apparent in Direct DIVAM until the excitation angle was greater than 30^o; however, such behaviour is already quite pronounced in Refocused DIVAM at excitation angles of 15^o or greater. This indicates that the selection mechanism at much smaller angles is being driven by an orientationally dependent term. This further supports the earlier statement that the CSA is the main interaction driving the selection mechanism of Refocused DIVAM. The amorphous signal is seen to nutate through one cycle for an excitation angle of 15^o and multiple cycles for excitation angles greater than 15^o. Nutation of the crystalline signals

can be seen, but is far less pronounced than that of the amorphous signal. The periodic behaviour of the amorphous signal, with respect to the rotor period, is very different from that seen in Direct DIVAM. The addition of 180^{o} refocusing pulses could be causing partial recoupling of the CSA term in the Hamiltonian. The oscillations in the intensity of the amorphous signal will be further explored with Simpson simulations in section 4.4.2.

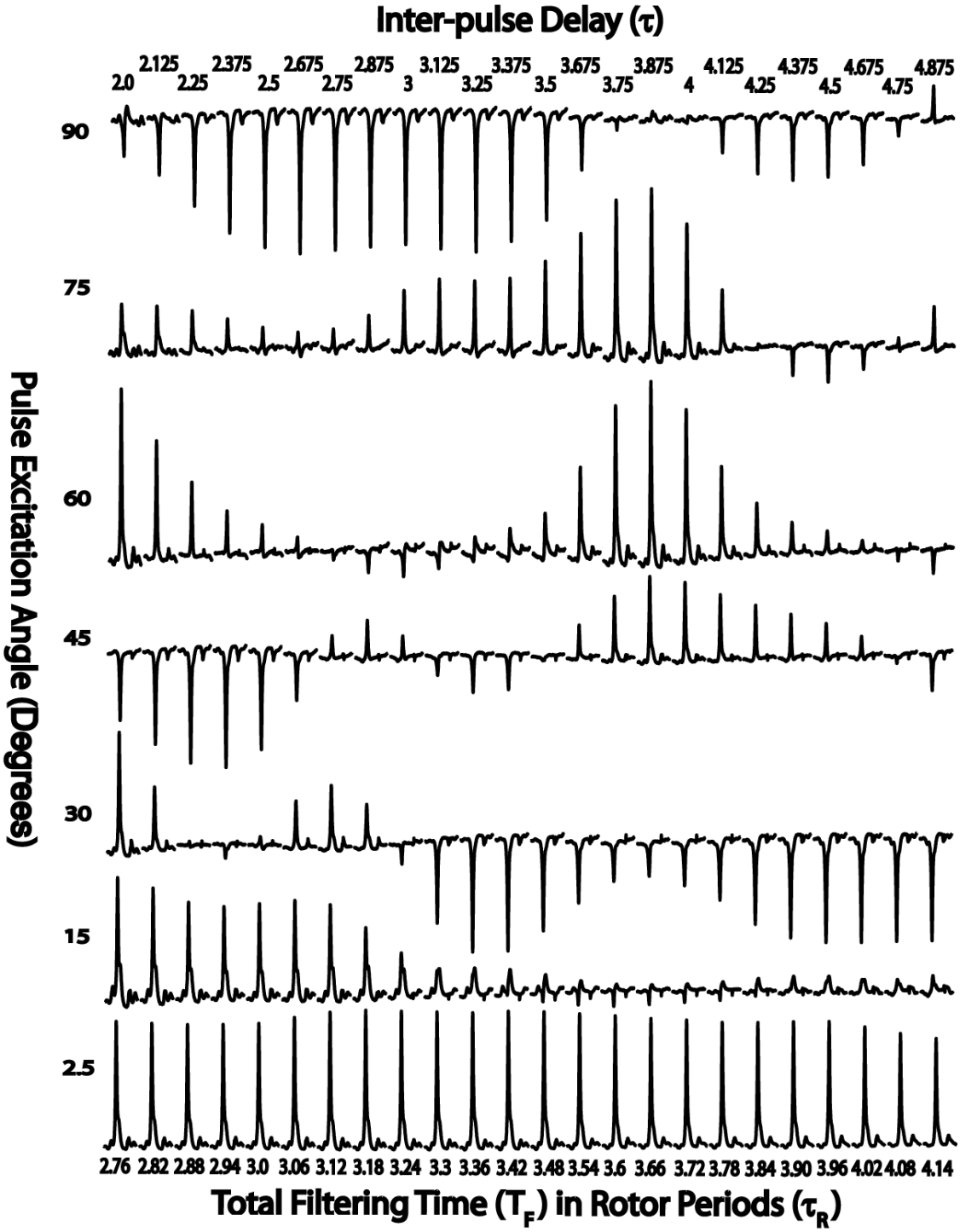

Figure 62 ^{19}F Refocused DIVAM spectra of PVDF over a series of inter-pulse delays, calibrated such that T_F covers 3 to 4 rotor periods (T_R). This array is shown for selected excitation angles from 2.5 to 90 degrees using a MAS rate of 20 kHz, a 90^o pulse width of 2.5 μs, a 180^o pulse width of 5 μs (T_F = 150 μs), and a pulse offset of 1 kHz.

Figure 63 illustrates the response of the ^{19}F MAS NMR spectra of PVDF for each of the selected excitation angles as the inter-pulse delay is varied such that the T_F covers 500 rotor periods (τ_r) in a non-linear fashion, with the spacing increasing from 5, 10, to 100 τ_r (referred to as the long time series). For the small excitation angles, *ca*. 2.5^o, the intensity of the amorphous signal appears to oscillate around its maximum and it will be shown later that this minor oscillation can be attributed to the CSA term of the Hamiltonian (see section 4.4.2.). For short delay times (τ = 17.06 μs), as the excitation angles increases (θ = 2.5 ^{o} to θ = 30^o) the net rotation of the amorphous signal also increases and its intensity is reduced until it reaches the first null condition, as seen in the excitation angle array (figure 58). As the delay time increases none of the signals appear to recover intensity when exceeding the T_2 time scale. In the case of Direct DIVAM, T_2 recovery behaviour was apparent for the excitation angles of both 15^o and 30^o. This indicates that relaxation plays a lesser role in the domain selection of Refocused DIVAM. This is most likely due to the application of the refocusing pulses as they remove the effects of field in-homogeneity and effectively lengthen the T_2 value. Beyond 30^o the net rotation in the transverse plane becomes large enough that the saturation effect becomes increasingly pronounced, eventually reaching a point at which the signal does not recover over the long time range. The amorphous signal at large excitation angles (θ = 45^o or larger) does appear to recovery for small inter-pulse delays that coincide with multiples of the rotor period. This again suggests that the use of 180^o refocusing pulses may lead to some recoupling of the CSA term in the Hamiltonian.

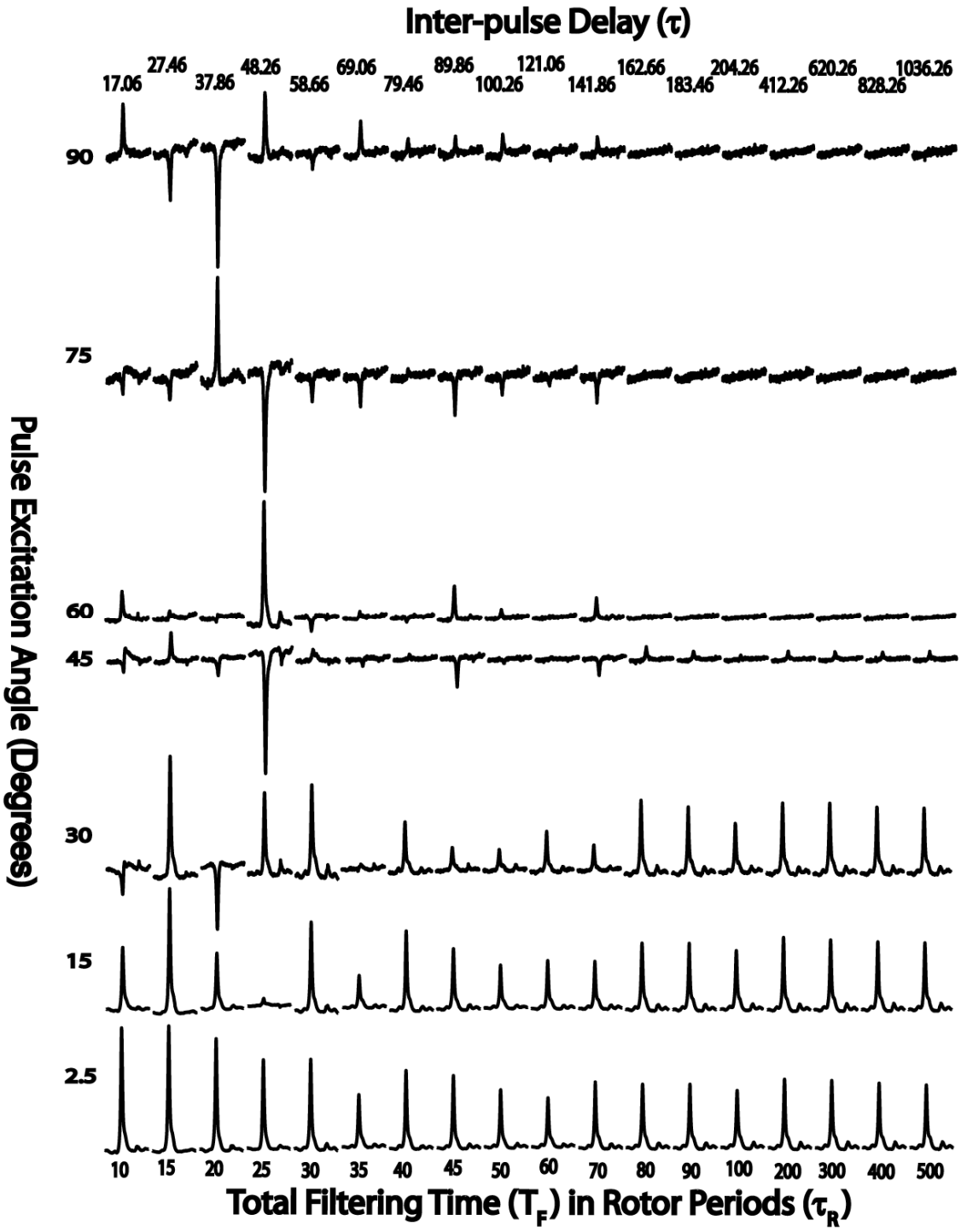

Figure 63 ^{19}F Refocused DIVAM spectra of PVDF over a series of inter-pulse delays, calibrated such that T_F covers 10 to 500 rotor periods (T_R). This array is shown for selected excitation angles from 2.5 to 90 degrees using a MAS rate of 20 kHz, a 90^o pulse width of 2.5 μs, a 180^o pulse width of 5 μs (T_F = 150 μs), and a pulse offset of 1 kHz.

In summary, the long and the short time series illustrate aspects of the spin dynamics during the Refocused DIVAM experiment that differ from those seen in Direct DIVAM. The short time series for Direct DIVAM showed that transient oscillations are observed for excitation angles larger than 30^o. In contrast, the analogous Refocused DIVAM series illustrated significant transient behaviour for angles of 15^o or larger. The long time series of both Refocused and Direct DIVAM illustrate that the saturation effect is more pronounced with increasing excitation angle; however, in Refocused DIVAM this saturation does not appear to recover on the T_2 time scale for small excitation angles, as was seen in Direct DIVAM. Both of these results suggest that coherent spin dynamics play a much larger role in the selection mechanism of Refocused DIVAM, while the role of relaxation seems to have decreased.

3.4 Spin Dynamics Simulations

Simulations of the Refocused and Direct DIVAM sequences were performed to investigate the effect of each term in the ^{19}F Hamiltonian separately. Parallel simulations were performed using real (soft) pulses under rotor-synchronized and non-rotor-synchronized conditions. In the first section, the nutation behavior is investigated by simulating the signal over a range of excitation angles from 0^o to 90^o with an inter-pulse delay of 2.5 μs and a pulse offset of 1 kHz. The second section investigates the transient behaviour of the sequence, where the signal is computed over a range of inter-pulse delay values for various fixed excitation angles and a fixed pulse offset. In both cases, the nutation behaviour of the longitudinal magnetization (z-magnetization) remaining after the filter sequence will be explained separately for each term in the Hamiltonian.

3.4.1. Nutation Behaviour

I. The Isotropic Offset Term

Figure 64 shows that for a large range of frequencies the isotropic shift term of the Hamiltonian has been fully refocused in the rotor and non-rotor synchronized cases of Refocused DIVAM. No difference is observed between the rotor synchronized and non-synchronized cases, which is also to be expected as the isotropic term is not modulated by sample rotation. Note that in the Direct DIVAM simulations (figure 64c) the isotropic shift (offset) dependence of the nutation behaviour is obvious and has been clearly removed in Refocused DIVAM. Also, the nutation of the 25 kHz curve in the Direct DIVAM simulations closely resembles the nutation of the BB and SC signals in the off-resonance Direct DIVAM arrays of Nafion (Figure 59b and c), where the BB and SC signals are approximately 20 kHz off-resonance. This provides further support for the argument that the nutation behaviour of Direct DIVAM is dominated by the isotropic chemical shift term of the Hamiltonian.

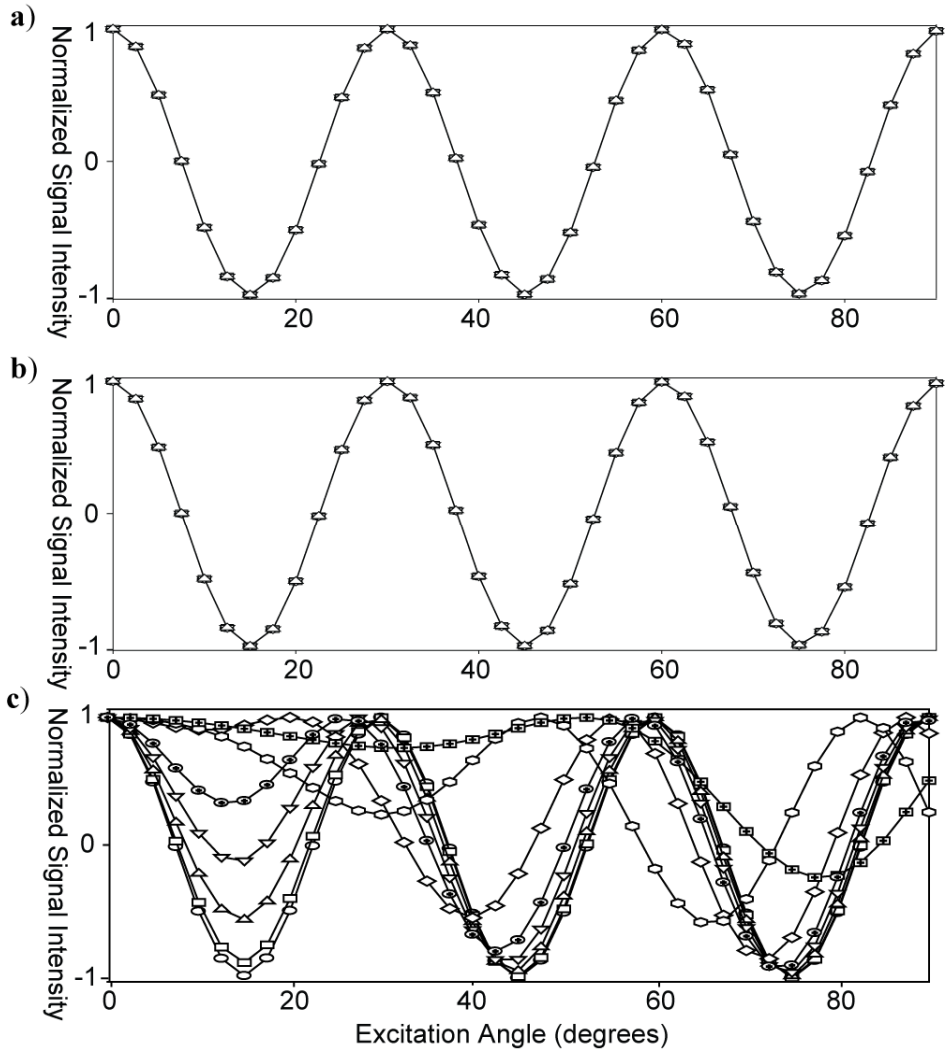

Figure 64 Simulation of the Refocused (a,b) and Direct DIVAM sequences (c), which illustrate the behaviour of the isotropic chemical shift term of the Hamiltonian. The rotor synchronized (a, c) and the non-rotor synchronized (b) simulations used an MAS rate of 20 and 25 kHz, respectively. The isotropic chemical shift was varied between 1 to 50 kHz, where ○ = 1 kHz, □ = 2.5 kHz, △ = 5 kHz, ▽ = 7.5 kHz, ◇ = 10 kHz, ⬡ = 15 kHz, ⊞ = 25 kHz, and ⊕ =50 kHz. The Refocused DIVAM simulations used real 100 kHz pulses with a 90^{o} pulse width of 2.5 μs, a 180^{o} pulse width of 5 μs, an inter-pulse delay of 2.5 μs (T_F = 150 μs) and a pulse offset of 1 kHz. The Direct DIVAM simulations used real 100 kHz pulses with a 90^{o} pulse width of 2.5 μs and an inter-pulse delay of 1.67 μs (T_F = 50 μs).

II. The Chemical Shift Anisotropy Term

Figure 65 shows the nutation behaviour of the Refocused and Direct DIVAM sequences over a range of CSA strengths. Some interesting observations can be made when comparing the rotor-synchronized Refocused (figure 65a) and Direct DIVAM simulations (figure 65c). For selection to occur in Direct DIVAM an interaction strength of 50 kHz or larger is required. In comparison, Refocused DIVAM is sensitive to weaker interaction strengths when using small excitation angles; therefore, Refocused DIVAM appears to be a more sensitive CSA filter, as suggested earlier.

From the rotor synchronized Refocused DIVAM simulations, one can see that the first minimum is quite different for strengths of 10 kHz and above. More importantly, note that there is very little difference at the point of the first zero crossing for interaction strengths up to 15 kHz. For larger excitation angles, *ca* $\theta \geq 30^{o}$, the zero crossing points do not vary significantly for interaction strengths less than 50 kHz.

The behaviour under non-rotor synchronized conditions (figure 65b) is substantially different from the rotor-synchronized case, due to the rotational dependence of the CSA term. In this case, no difference in the point of the first zero crossing can be seen for interaction strengths up to 25 kHz. On the other hand, differentiation in the maximum, minimum, and zero crossing of the nutation behaviour is seen for interaction strengths above 10 kHz when an excitation angle greater than 30^{o} is used. Interestingly, when an excitation angle of 30^{o} or less is used the non-rotor-synchronized behaviour of Refocused DIVAM closely resembles behaviour of Direct DIVAM. These results indicate that in order to achieve optimum selection the rotor-synchronization conditions of the sequence must be considered.

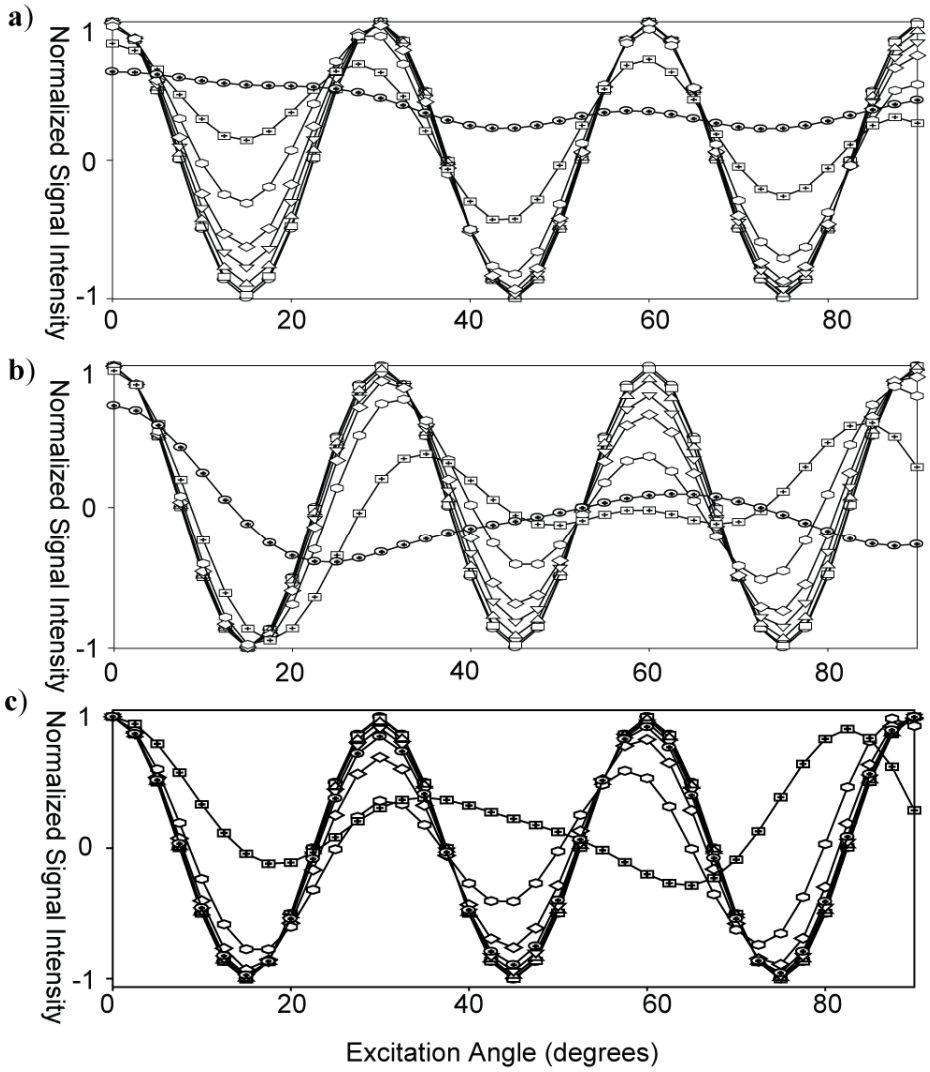

Figure 65 Simulation of the Refocused (a,b) and Direct DIVAM sequences (c), which illustrate the behaviour of the chemical shift anisotropy term of the Hamiltonian. The rotor synchronized (a, c) and non-rotor synchronized (b) simulations used an MAS rate of 20 and 25 kHz, respectively. The CSA was varied between 1 to 50 kHz, where ○ = 1 kHz, □ = 2.5 kHz, △ = 5 kHz, ▽ = 7.5 kHz, ◇ = 10 kHz, ⬡ = 15 kHz, ⊞ = 25 kHz, and ⊕ =50 kHz. The Refocused DIVAM simulations used real 100 kHz pulses with a 90^{o} pulse width of 2.5 μs, a 180^{o} pulse width of 5 μs, an inter-pulse delay of 2.5 μs (T_F = 150 μs) and a pulse offset of 1 kHz. The Direct DIVAM simulations used real 100 kHz pulses with a 90^{o} pulse width of 2.5 μs and an inter-pulse delay of 1.67 μs (T_F = 50 μs).

The effects of rotor synchronization were further explored using a range of CSA values over a series of inter-pulse delays, at a spinning speed of 20 kHz (Figure 66). Rotor synchronization occurs at $\tau = 2.5$ μs and corresponds to a T_F = 150 μs. At these

conditions the first zero crossing is seen between $\theta = 7.5^{o}$ and $\theta = 10^{o}$, indicating the first selection condition. Upon closer examination, the selection condition becomes more favourable as the inter-pulse delay increases towards $\tau = 2.5$ μs and deteriorates beyond this value. Interestingly, the selection behaviour at small angles does not improve when the sequence is synchronized at either 2 or 4 rotor periods. This indicates that not only rotor synchronization, but also the number of rotor periods to which you synchronize the sequence, is important in achieving optimum selection when using small excitation angles. This suggests using inter-pulse delays approaching 5 rotor periods; however, for interaction strengths of 90 kHz one can see that the signal is completely lost for longer inter-pulse delays ($\tau = 5$ μs). The sequence must therefore be restricted to shorter inter-pulse delays in order to select for larger CSA values. It is important to note that the nutation curve of the 25 kHz CSA interaction, for an inter-pulse delay of 3μs (top right of figure 66), closely resembles the nutation profile of the amorphous peak in Refocused DIVAM array (figure 58). This provides further support that the selection mechanism for Refocused DIVAM is driven by the CSA term, but only when its strength is greater than or equal to 15 kHz. This correspondence between the rotor synchronized measurements and the non-rotor-synchronized simulations is most likely due to spinning instabilities in the MAS controller.

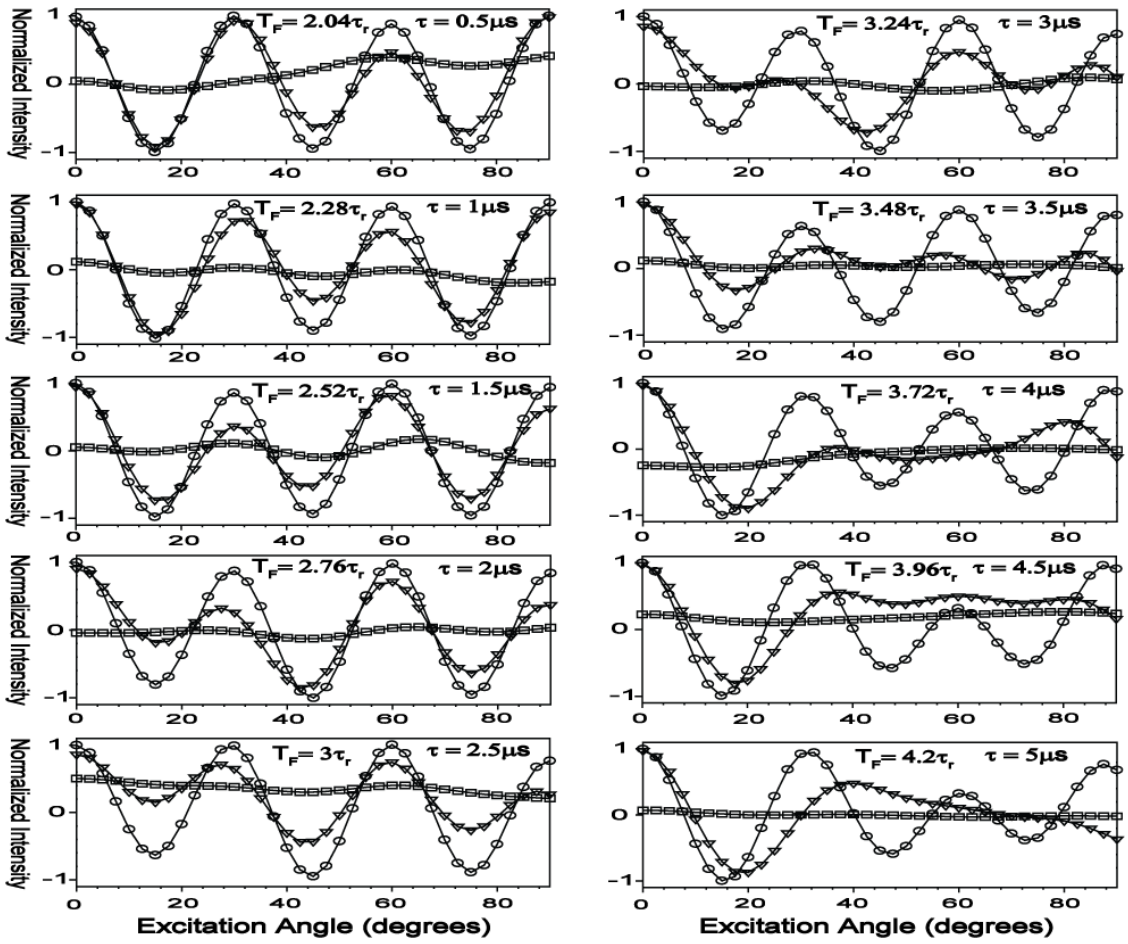

Figure 66 The effect of rotor-synchronization on the selectivity of the Refocused DIVAM pulse sequences for various chemical shift anisotropy and τ values, where ○ = 10 kHz, ▽ = 25 kHz, and □ = 90 kHz. These Simulations used real 100 kHz pulses with an MAS rate of 20 kHz, a 90° pulse width of 2.5 μs, a 180° pulse width of 5 μs, and a pulse offset of 1 kHz. The inter-pulse delay and total filtering time (T_F) are indicated at the top of each figure.

III. The Dipolar Coupling Term

Figure 67 shows the nutation behaviour of the signal from the Refocused and Direct DIVAM sequences over a range of Dipolar coupling interaction strengths. The comparison between the Refocused (figure 67a) and Direct DIVAM (figure 67c) rotor-synchronized simulations is quite different than what was seen for the CSA term. Differentiation is observed at the first zero crossing for couplings of 25 kHz or greater in

Direct DIVAM while a larger coupling of 50 kHz or greater is required for Refocused DIVAM. Also note that selection between the excitation angles of $\theta = 30^{o}$ and $\theta = 90^{o}$ is not apparent in Direct DIVAM while it is quite profound in Refocused DIVAM.

. In the rotor synchronized case for small excitation angles, *ca* $\theta < 30^{o}$, very little difference can be seen between the signals for interaction strengths less than 50 kHz; however, there is a significant difference in the signal when excitation angles greater than 30^{o} are used. A dipolar coupling of 50 kHz is uncommon in fluoropolymers and therefore, for small excitation angles, the dipolar coupling should not be expected to contribute to the selection behaviour in the rotor-synchronized case. It is possible that selection could occur in the excitation angle range of $\theta = 30^{o} - 60^{o}$ and would be based on a dipolar interaction of 15 kHz or greater.

The nutation of each signal is much more complicated in the non-rotor synchronized case (figure 67b), due to the rotational dependence of the dipolar term. Similar to the CSA term, no significant differences in signal for the various interaction strengths are observed in the small excitation angle regimes, *ca* $\theta < 30^{o}$. In the case of the intermediate excitation angles, *ca* $\theta = 30^{o}$ -- 60^{o}, the nutation behaviour varies less and now requires interaction strengths of 25 kHz or greater for selection to occur. In the large excitation angles, *ca* $\theta \geq 60^{o}$, more differentiation is seen between signals and selection can be achieved with interaction strengths of 15 kHz or higher. This again suggests that in order to achieve optimum selection conditions rotor synchronization must be considered.

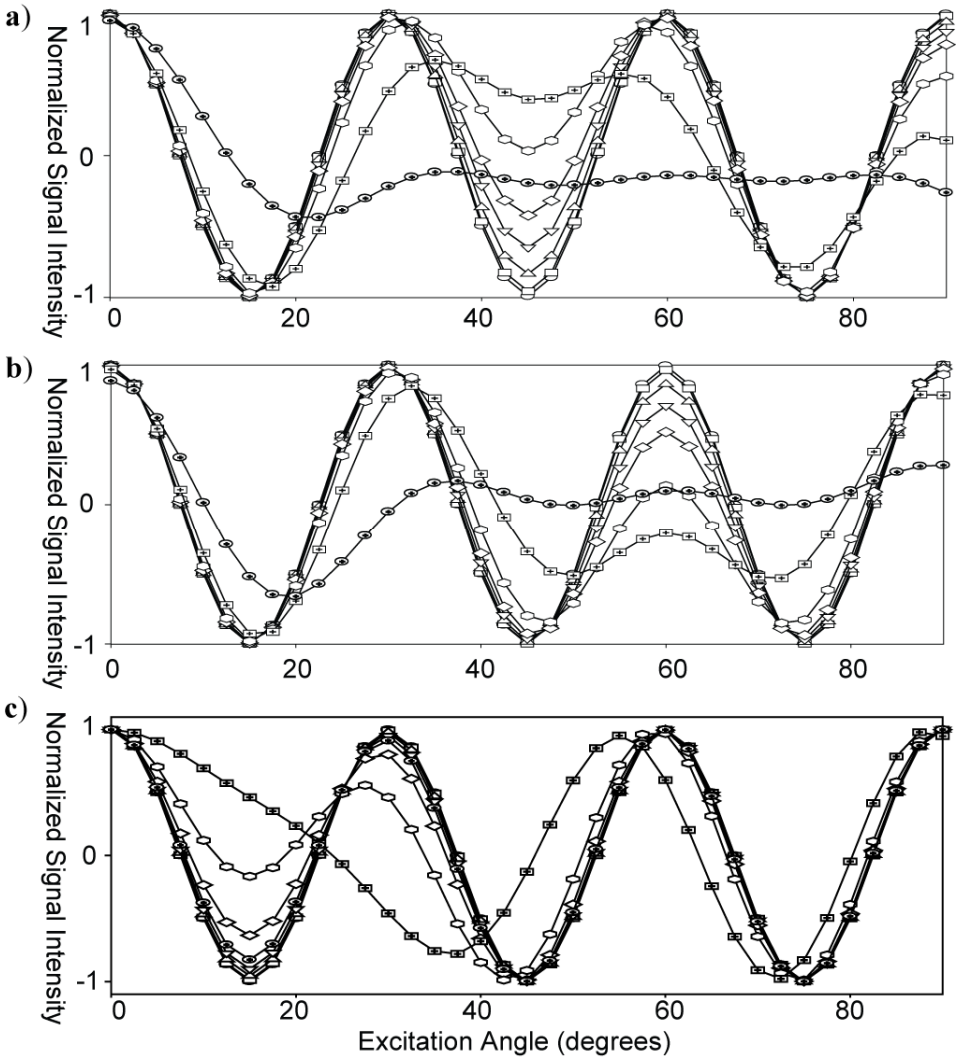

Figure 67 Simulation of the Refocused (a,b) and Direct DIVAM sequences (c), which illustrate the behaviour of the dipolar coupling term of the Hamiltonian. The rotor synchronized (a, c) and non-rotor synchronized (b) simulations used an MAS rate of 20 and 25 kHz, respectively. The dipolar coupling was varied between 1 to 50 kHz, where ○ = 1 kHz, □ = 2.5 kHz, △ = 5 kHz, ▽ = 7.5 kHz, ◇ = 10 kHz, ⬡ = 15 kHz, ⊞ = 25 kHz, and ⊕ =50 kHz. The Refocused DIVAM simulations used real 100 kHz pulses with a 90^o pulse width of 2.5 μs, a 180^o pulse width of 5 μs, an inter-pulse delay of 2.5 μs (T_F = 150 μs) and a pulse offset of 1 kHz. The Direct DIVAM simulations used real 100 kHz pulses with a 90^o pulse width of 2.5 μs and an inter-pulse delay of 1.67 μs (T_F = 50 μs).

Figure 68 shows a series of simulations of the dipolar term over a range of inter-pulse delays for two dipolar coupling values. For the small excitation angles, *ca* $\theta < 30^o$, rotor synchronization seems to be less important and no significant selection is seen

between the two curves. For the large excitation angles, *ca* $\theta \geq 60^{o}$, no noticeable selection occurs as the inter-pulse delay is decreased from 2.5 μs to 0.5 μs ($T_F = 2.04\ \tau_r$); however, selection can be seen the inter-pulse delay is increased to a value of 4.5 μs ($T_F = 3.96\ \tau_r$). This indicates that for the larger excitation angles, *ca* $\theta \geq 60^{o}$, the rotor synchronization and the number of rotor periods are important when optimizing the selection conditions of the sequence.

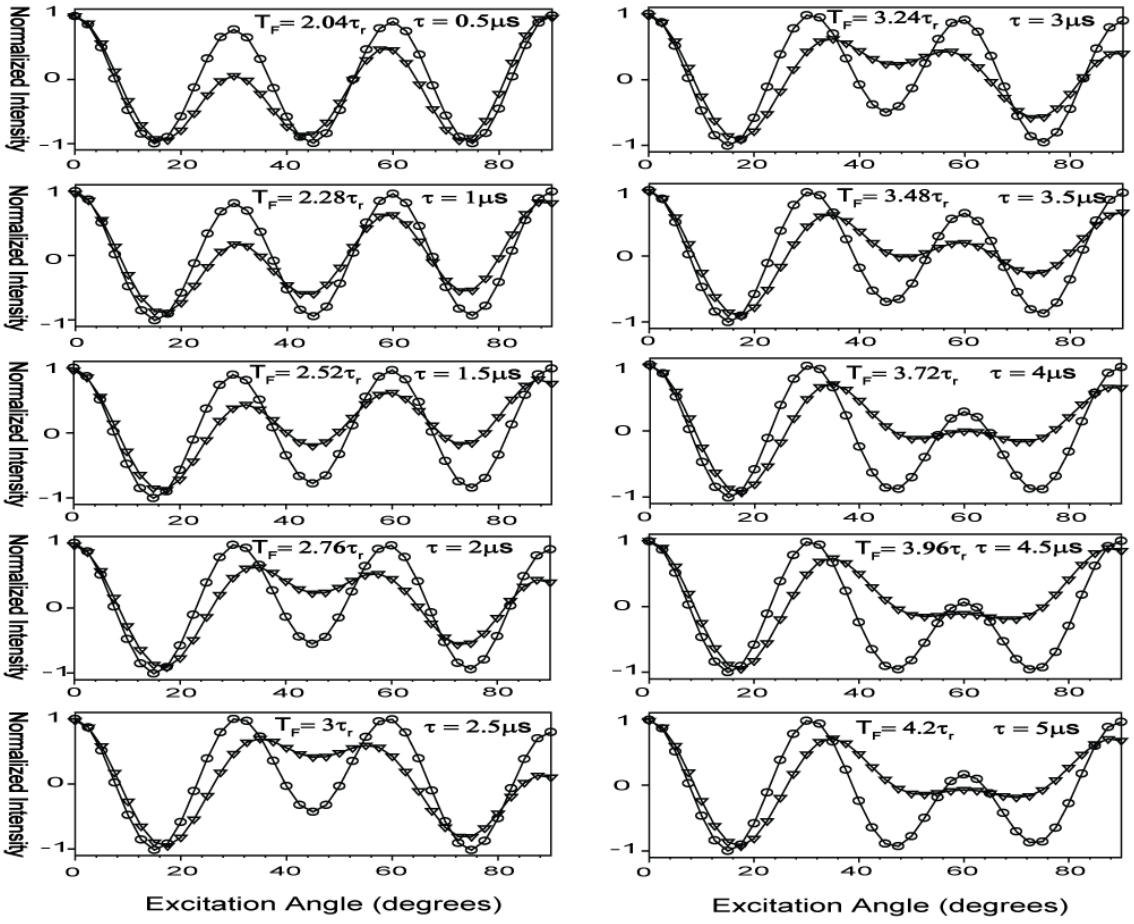

Figure 68 The effect of rotor-synchronization on the selectivity of the Refocused DIVAM pulse sequences for various dipolar coupling and τ values, where ○ = 10 kHz and ▽ = 25 kHz. These Simulations used real 100 kHz pulses with an MAS rate of 20 kHz, a 90° pulse width of 2.5 μs, a 180° pulse width of 5 μs, and a pulse offset of 1 kHz. The inter-pulse delay and total filtering time (T_F) are indicated at the top of each figure.

IV. Summary

If rotor synchronization is to be considered a requirement for domain selection then the effect of the CSA and Dipolar Hamiltonian should be considered in two cases: small and large angles. In the former case, CSA and dipolar interaction strengths of 15 and 50 kHz, respectively, are required for these terms to have a role in the selection. In the latter case, both rotor synchronization and the number of rotor periods over which the filter is applied are an important consideration. The total filtering time must be chosen such that no selection takes place for CSA and dipolar interaction strengths less than 25 and 50 kHz, respectively. A total filtering time which is rotor synchronized and limited to a number of rotor periods reduces the amount of coherent dephasing that can occur during the inter-pulse delays, thereby ensuring minimal phase distortion in the large angle nutation behaviour. Also, Refocused DIVAM is a more sensitive CSA filter than Direct DIVAM, with the latter requiring a CSA interaction strength of at least 50 kHz for selection to occur. The next section of simulations is designed to mimic the experimental transient series presented in section 3.3.2 in order to better understand the observed behaviour.

3.4.2. Transient Behaviour

The simulations of the transient behavior for both the CSA and Dipolar terms of the Hamiltonian were carried out with a pulse offset of 1 kHz. It is important to note that these simulations were also run using a pulse offset of 100 Hz and 5 kHz and all three sets of simulations produced identical results. This is in agreement with the experimental transient series run at these three pulse offsets indicating that, as long as a pulse offset no

larger than 5 kHz is used, the pulse offset has no effect on the observed transient behaviour.

I. The Chemical Shift Anisotropy Term

Figure 69 shows the response of the ^{19}F signal intensity, for a set of selected excitation angles and CSA strengths, as a function of the inter-pulse delay used. These simulations use a time scale which corresponds to the experimental short time series (figure 62), where the inter-pulse delay is varied such that the T_F ranges over approximately two rotor periods (τ_r) in steps of 3/50 τ_r. When examining figure 69 it is apparent that the transient behaviour can only lead to selection when an excitation angle larger than 2.5^o is used; however, the transient oscillations seen in the signal intensity for an excitation angle of 2.5^o appear to agree with the oscillations of the amorphous signal seen experimentally for this angle (figure 62). This indicates that the selection at 2.5^o may also be driven by the CSA term. The fact that the transient behaviour for any excitation angle larger than 2.5^o can lead to selection further exemplifies the need to ensure that the sequence is rotor-synchronized, as indicated above in section 3.4.1. Furthermore, the number of zero crossings seen in the signal oscillations appears to be dependent upon the excitation angle used. For example, only one zero crossing is seen for an excitation angle of 15^o, while three zero crossings are seen for an excitation angle of 30^o. This is in agreement with the experimental transient behaviour for the amorphous signal of PVDF at both of these angles (see figure 62). Upon closer examination, the experimental transient oscillations of the amorphous signal appears to resemble the simulated CSA curves in figure 69 for an interaction strength ranging between 30 and 40

kHz; however, the experimental behavior seems to lag slightly behind the simulated curves. The oscillations in the experimental data can only be fit by the simulations if we consider the simulated curves to begin at an inter-pulse delay of 2.75 μs. This 0.75 μs lag can most likely be attributed to both spinning instabilities in the MAS controller and fluctuations in the applied RF power of the pulses (B_1).

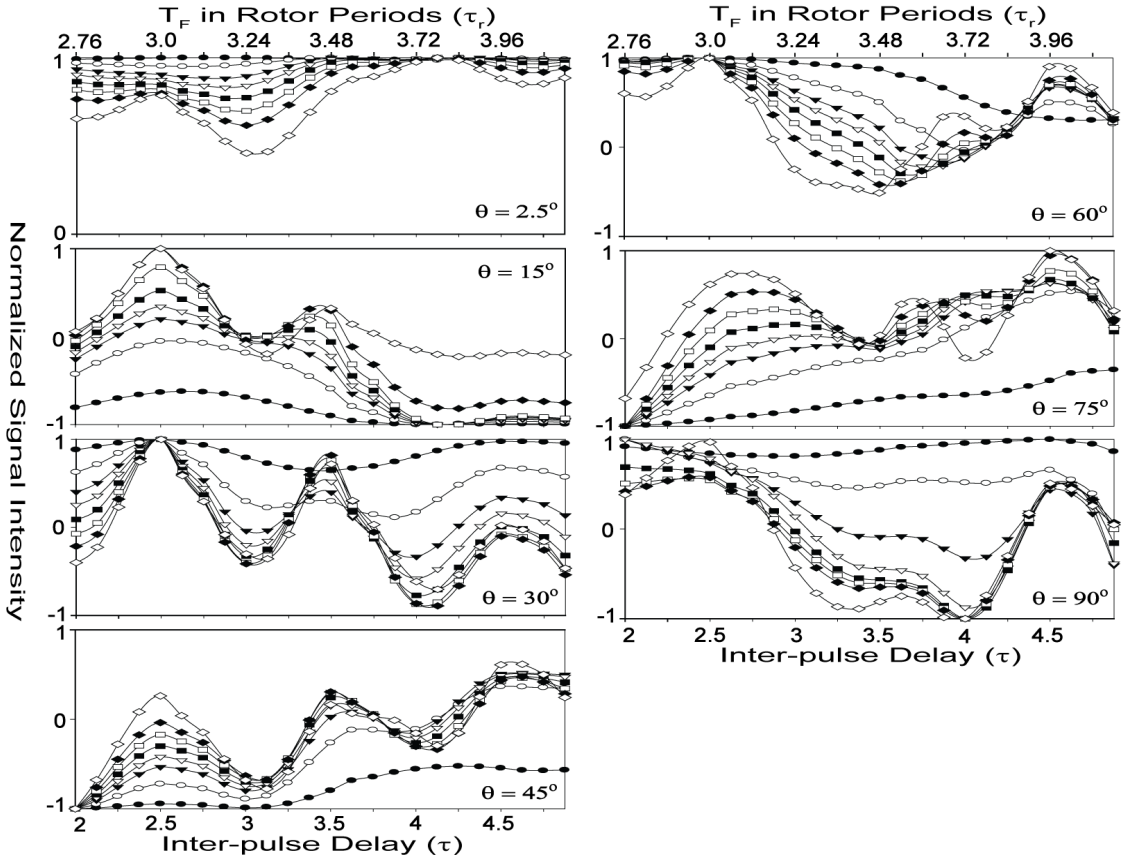

Figure 69 The effect of varying the inter-pulse delay on the selectivity of the Refocused DIVAM pulse sequences for selected excitation angles and CSA strenths, where the excitation angle is indicated in the figure and the CSA interaction strengths are represented by the following: ● = 10 kHz, ○ = 20 kHz, ▼ = 25 kHz, ▽ = 27.5 kHz, ■ = 30 kHz, □ = 32.5 kHz, ◆ = 35 kHz, and ◇ = 40 kHz. These Simulations used real 100 kHz pulses with an MAS rate of 20 kHz, a 90° pulse width of 2.5 μs, a 180° pulse width of 5 μs, and a pulse offset of 1 kHz.

II. The Dipolar Coupling Term

Figure 70 shows the response of the ^{19}F signal intensity, for a set of selected excitation angles and dipolar coupling strengths, as a function of the inter-pulse delay used. These simulations use a time scale which corresponds to the experimental short time series (figure 62), where the inter-pulse delay is varied such that the T_F ranges over approximately two rotor periods (τ_r) in steps of 3/50 τ_r. The dipolar couplings presented in Figure 70 are homo-nuclear interactions and a coupling of 25 kHz is at the large end of what is typically found in a fluoropolymer system. When looking at the transient behaviour of the 10 and 25 kHz curves it is clear that no zero crossings occur for any excitation angle; therefore, the dipolar coupling should not be expected to lead to any selection in the ^{19}F spectra of fluoropolymer systems. However, it can be expected to contribute to the signal oscillations seen experimentally. This again further supports the earlier argument that the selection behaviour of Refocused DIVAM, when applied to the ^{19}F nucleus, is driven by the CSA term. Alternatively, a coupling of 50-75 kHz can be found when looking at proton nuclei in a highly crystalline polymer system. In this case the transient behaviour due to the dipolar coupling could lead to selection at any excitation angle greater than 30^o.

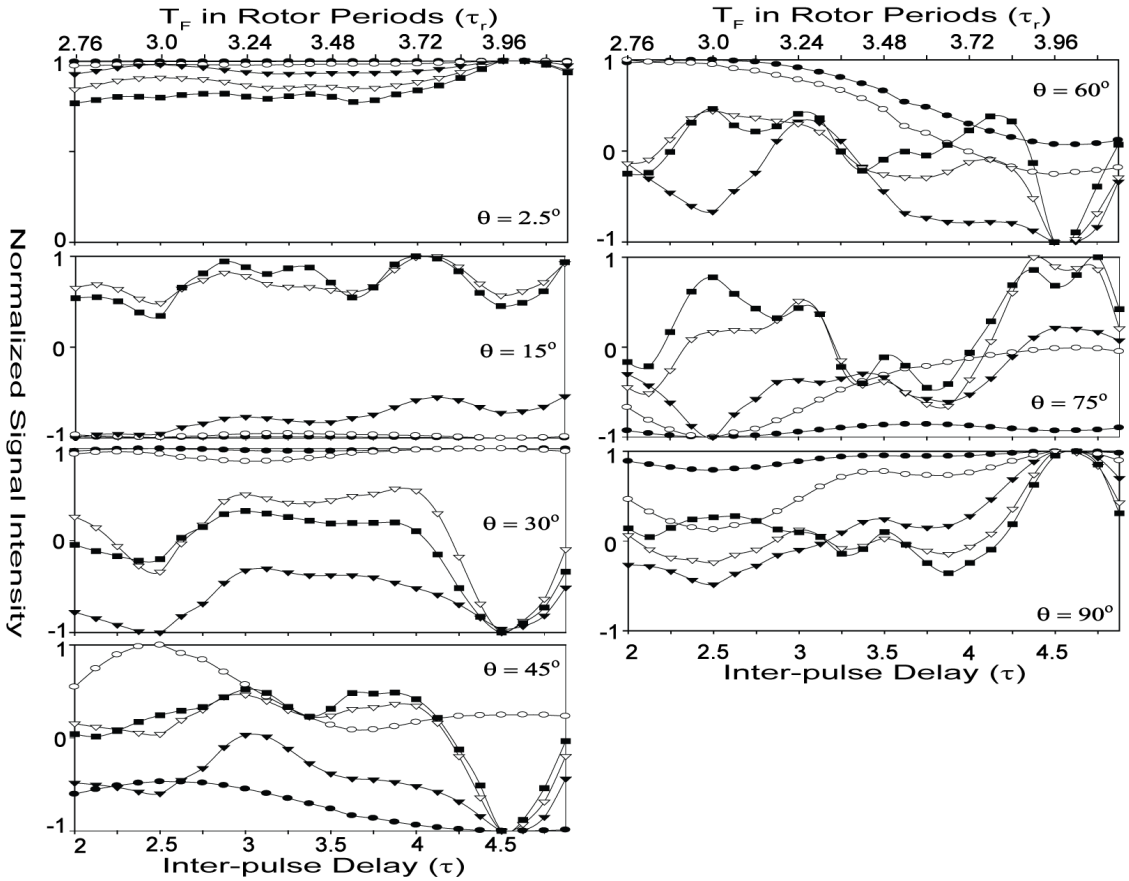

Figure 70 The effect of varying the inter-pulse delay on the selectivity of the Refocused DIVAM pulse sequences for selected excitation angles and dipolar coupling values, where the excitation angle is indicated in the figure and the dipolar coupling values are represented by the following: ● = 10 kHz, ○ = 25 kHz, ▼ = 50 kHz, ▽ = 75 kHz, and ■ = 90 kHz. These Simulations used real 100 kHz pulses with an MAS rate of 20 kHz, a 90^{o} pulse width of 2.5 μs, a 180^{o} pulse width of 5 μs, and a pulse offset of 1 kHz.

3.5 Selection Mechanism

Refocused DIVAM experiments show that the phase distortions at large angles seen in the Direct DIVAM experiments have been successfully removed by the addition of refocusing pulses. These experiments also demonstrate that the offset dependence of Direct DIVAM has been greatly reduced and that nutation of all signals has been restored. SIMPSON simulations illustrate that the effect of the isotropic term has been removed. They also show that the effect of the CSA and dipolar terms on the selection

mechanism of Refocused DIVAM is profoundly different than for Direct DIVAM. In fact, Refocused DIVAM is more sensitive to the CSA term and less sensitive to the dipolar term. Both the experimental and simulated transient series indicate that the CSA term now plays a much larger role in the selection mechanism for small excitation angles; furthermore, they provide some evidence that even selection at the excitation angle of 15^{o} may be dominated by the CSA term. Imposing rotor synchronization in Refocused DIVAM is particularly important in order to reduce the effect of coherent dephasing during the inter-pulse delays and ensures optimum selection.

In summary, the Refocused DIVAM sequence provides nutation behaviour that is less complex than that of Direct DIVAM, yet similar to the original DIVAM experiment, and appears to be driven by the CSA term of the Hamiltonian. Refocused DIVAM now provides a far more robust method for directly applying the DIVAM sequence to the nucleus of interest, while mostly removing the offset term from the selection process.

3.6 Pulse Offset Effects

3.6.1 Overview

Earlier it was mentioned that the Refocused DIVAM sequence is typically implemented with a pulse offset of 5 kHz or less. This section explores how the use of a pulse offset larger than 5 kHz affects the oscillation of the observed signals during the Refocused DIVAM sequence. Figure 71 shows the observed nutation behavior for Refocused DIVAM when various different pulse offsets are used. Figure 71a illustrates that the observed behaviour when using a pulse offset of 5 kHz is very similar to that

seen when using a pulse offset of 1 kHz (see figure 58); however, this is not the case when using a pulse offset of 15 or 25 kHz. When a pulse offset of 15 kHz is used the amorphous and crystalline peaks undergo a second inversion for the excitation angles of 80^{o} - 90^{o}. This difference is even more pronounced for a pulse offset of 25 kHz, showing three extra inversions in the excitation angle ranges of 20^{o} - 25^{o}, 62.5^{o} - 72.5^{o}, and 82.5^{o} - 90^{o}. More importantly, when examining the spectra for each excitation angle a surprising result is seen when using a pulse offset of 25 kHz.

Figure 71d shows expansions of the ^{19}F spectra for a set of chosen excitation angles from the nutation array at 25 kHz (figure 71c). Upon closer examination, the excitation angles of 30^{o} and 57.5^{o} show an additional signal in the chemical shift region of the defect units that is very narrow, compared to the amorphous signal, and appears at ~115 ppm. Both the line width and shift of this peak coincide with the signal from the highly mobile end-chain signals observed previously for PVDF.[88] The end-chain signal has a much longer T_2 than the rest of the signals in the PVDF spectra, due to high mobility. Previously this peak could only be resolved, or observed, by using a Hahn echo experiment with a long enough delay to allow all other signals in the spectra to dephase completely. In this case, the Refocused DIVAM experiment has allowed for the observation of these signals without the complete removal of the other signals. This is an important result because it provides a method of measuring spin diffusion between the end chain signals and all of the various signals in PVDF; hence, allowing for domain size measurements.[104] A series of experiments and simulations must now be carried out in order to better understand how varying the pulse offset leads to the selection of the end chain signal.

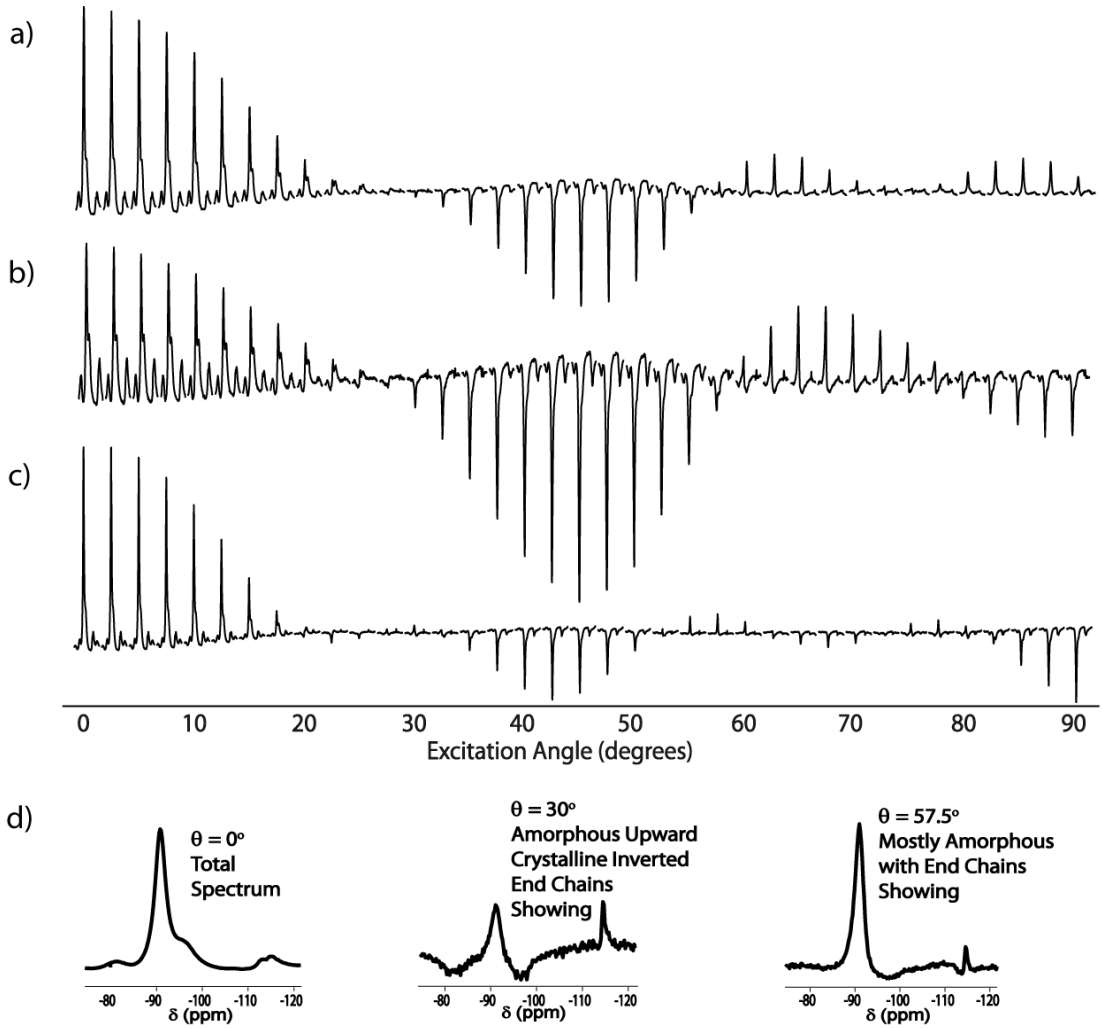

Figure 71 The Refocused DIVAM nutation array of the ^{19}F MAS NMR spectra of PVDF at 20 kHz and ranging over excitation angles of 0^0-90^0 in steps of 2.5^0. An inter-pulse delay of 2.5 μs, a 90^o pulse width of 2.5 μs, a 180^o pulse width of 5 μs (T_F = 150 μs), and a pulse offset of (a) 5 kHz, (b) 15 kHz, and (c) 25 kHz were used. d) Enlargements of the ^{19}F MAS NMR spectra of PVDF for selected angles in the Refocused DIVAM nutation array using a pulse offset of 25 kHz, illustrating the selection of the side chain signals in PVDF.

3.6.2 Experimental Pulse Offset Behaviour

The effect of a pulse offset can be further investigated by looking at the excitation profile of a 2.5 μs (100 kHz) pulse as shown in figure 72. The profiles in figure 72 were obtained by changing the offset frequency (or carrier frequency) of an excitation pulse while keeping the receiver fixed on a central resonance. All pulse offsets shown in figure 72 are with respect to the receiver frequency. Figure 72a shows the excitation profile of a single 2.5 ms excitation pulse when applied to hexafluorobenzene (C_6F_6) and with the receiver set to the frequency of the C_6F_6 peak (–166.4 ppm). The excitation profile of C_6F_6 is symmetric with respect to a pulse offset of zero and as a result the addition of two spectra acquired at opposite pulse offsets gives a Lorentzian peak. The symmetry of the excitation profile for C_6F_6 is lost at pulse offsets greater than 70 kHz and this imposes an instrumental limit on the pulse offset that can be employed. The behaviour seen above 70 kHz is most likely caused by phase instabilities within the console hardware occurring at these specific frequencies, which is typical of aging analogue equipment.

Figure 72b shows the excitation profile of a single 2.5 ms excitation pulse when applied to PVDF and with the receiver set to the frequency of the amorphous peak (–91.2 ppm). This is analogous to the pulse offsets used during the Refocused DIVAM sequence. Each pulse in the DIVAM train is applied with a pulse offset, while the observation pulse and receiver are centered at the frequency of the amorphous peak. The abnormalities seen in the excitation profile of C_6F_6 are still present; however, they begin to occur when employing a pulse offset of 35 kHz. If this behaviour was caused by phase instabilities in the console hardware then it should shift linearly with a change in the receiver frequency. The resonance frequency of the amorphous peak in PVDF is –91.2

ppm and is shifted ~ + 35 kHz (+75.2 ppm) from the C_6F_6 resonance frequency. This shift in receiver frequency is in agreement with the frequency shift for the observed abnormalities. This supports the earlier assumption that the distortions are caused by phase instabilities in the console hardware and imposes an instrumental limit of 35 kHz on the pulse offset that can be employed to study PVDF; however, the symmetry of the PVDF excitation array appears to deteriorate before a pulse offset of 35 kHz. Recall that the two crystalline components of PVDF are not equally shifted with respect to the amorphous peak. The downfield and upfield crystalline components are shifted ~6.35 kHz (13.5 ppm) and ~2.07 kHz (4.4ppm) from the amorphous peak, respectively. As a direct result, dispersion components of each crystalline peak will not be equivalent for two equal but opposite in magnitude pulse offsets. This problem can be clearly seen when comparing the phase shift of the spectra in figure 72b. The spectra acquired using a pulse offset of 10 kHz is no longer symmetric with the spectra acquired using a pulse offset of –10 kHz; therefore, the co-addition of the two spectra will not result in purely Lorentzian line shapes.

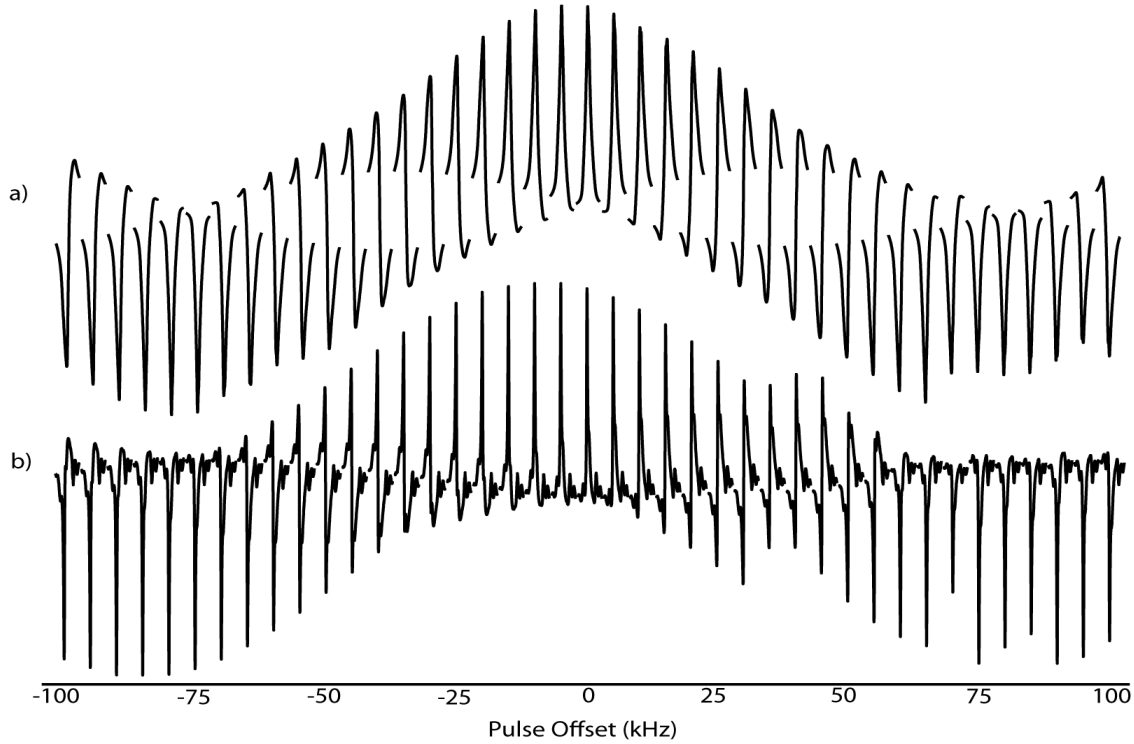

Figure 72 Excitation Profile of a) Hexafluorobenzene (C_6F_6) and b) PVDF obtained using a 2.5 μs pulse width (100 kHz pulse strength). The HFB profile was acquired without spinning while the PVDF profile was acquired while spinning at 20 kHz.

The effect of implementing Refocused DIVAM with an offset larger than 5 kHz was further explored by carrying out a series of measurements in which both the excitation angle and inter-pulse delay were fixed while varying the pulse offset of the Refocused DIVAM pulse train (referred to as the pulse offset array). The pulse offset array for an inter-pulse delay of 2.5 μs (T_F = 150 μs) and several fixed excitation angles can be seen in figure 73. Very little difference can be seen when using a pulse offset of 1 to 5 kHz, with only a minor change in the intensity of the amorphous peak occurring for all angles. Figure 72b showed that when a pulse offset greater than 35 kHz is used, with respect to the amorphous peak of PVDF, the console introduces a form of noise that interferes with normal pulse offset behavior. This interference can be clearly seen when

looking at the excitation angle of 30^{o} and the use of a pulse offset equal to or larger than 32.5 kHz; therefore, only the behavior seen when using a pulse offset of 30 kHz or less will be discussed from this point forward.

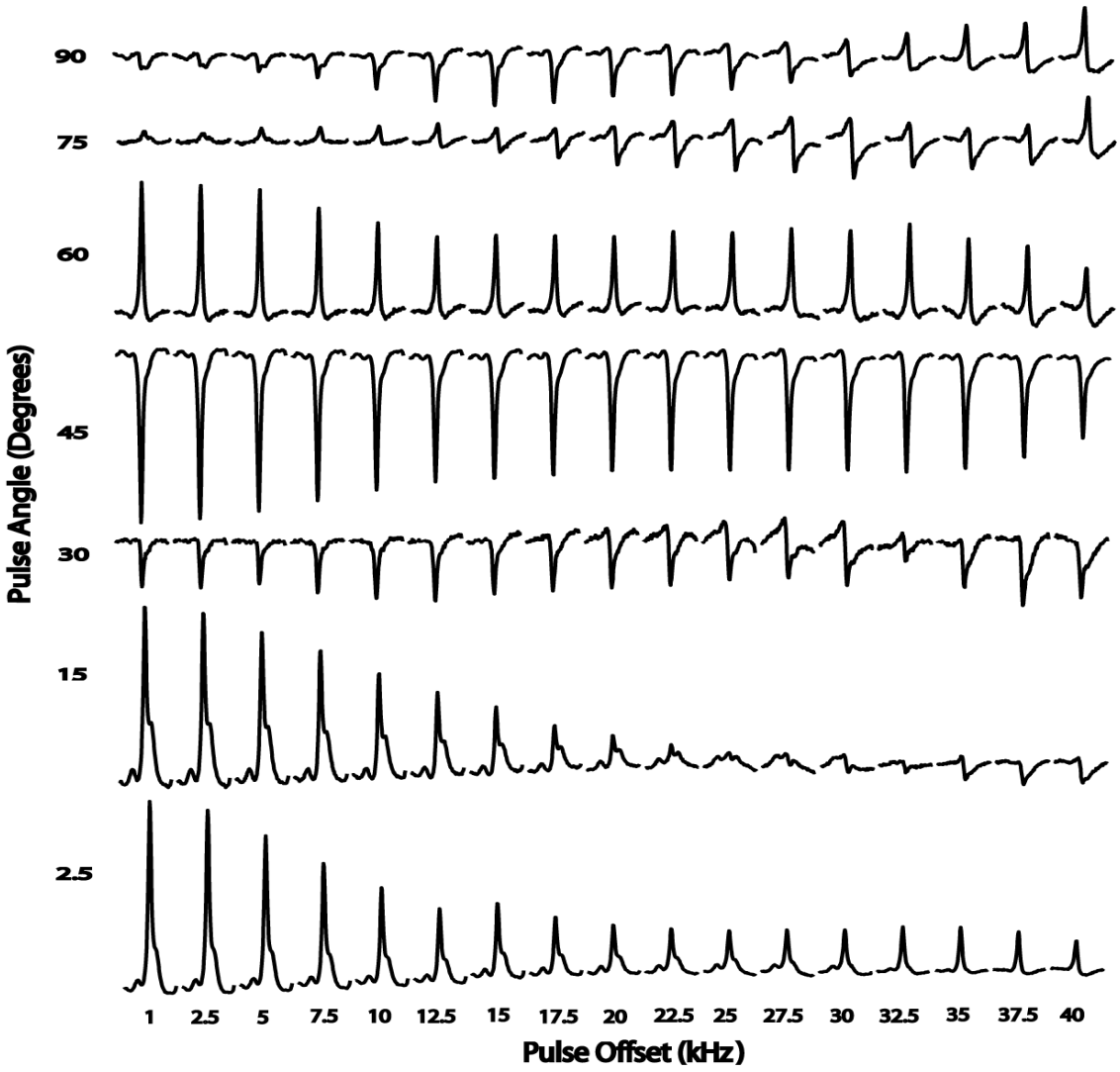

Figure 73 Pulse offset array of the ^{19}F Refocused DIVAM spectra of PVDF. This array is shown for selected excitation angles from 2.5 to 90 degrees using a MAS rate of 20 kHz, a 90^{o} pulse width of 2.5 μs, a 180^{o} pulse width of 5 μs, and an inter-pulse delay of 2.5 μs (T_F = 150 μs).

Figure 73 clearly indicates that oscillations in the amorphous signal are observed with respect to the pulse offset used for all excitation angles. These can now lead to a

null point in the amorphous signal and provide an alternative method by which the crystalline signals may be selected. The excitation of 15^{o} (row 2 in figure 69) shows that as the pulse offset is increased the amorphous signal gradually loses intensity until the spectra is almost purely crystalline when a pulse offset of 25 kHz is used. The use of a pulse offset to cause selection of the crystalline signals in PVDF will be further explored with SIMPSON simulations in section 3.6.3.

The Refocused DIVAM pulse offset array for an inter-pulse delay of 4.58 μs (T_F = 200 μs) and several fixed excitation angles can be seen in figure 74. This figure is analogous to figure 73, but is obtained with the sequence rotor synchronized to 4 rotor periods and allows for the investigation of pulse offset behaviour over multiple rotor periods. The oscillations in the amorphous signal are similar to those seen in figure 73 as long as they are considered with respect to the first spectra in the array. The first spectra in the array is expected to change because it was shown earlier (see section 3.3.2 figure 62) that the number of rotor periods over which the sequence is synchronized will change the observed nutation behavior. The only excitation angle at which no change in the initial spectra is expected is 2.5^{o} and this was indeed observed in figure 74

There are a couple of key differences that can be observed when comparing figures 73 and 74. Firstly, in figure 73 the use of a pulse offset between 1 and 5 kHz produced only a small change in the amorphous signal intensity and was not considered to be significant to the observed pulse offset behaviour. In contrast, Figure 74 shows that for an excitation angle of 15^{o} (row 2 figure 71) this small difference in the intensity results in the complete selection of the crystalline signals. Secondly, figure 74 shows significant oscillations when using an excitation angle of 90^{o} and a pulse offset up to 15

kHz and these are absent in figure 73; however, the oscillations seem to agree quite nicely beyond a pulse offset of 15 kHz. This variation is most likely caused by the relative intensity of the amorphous signal seen for a pulse offset of 1 kHz. Figure 73 has a rather large initial intensity of the amorphous signal, making the observation of the small deviations in signal intensity very difficult to observe. Figure 74 has a very small initial intensity of the amorphous signal and this makes observations of minor deviations in the signal intensity much easier to see. This is analogous to the behaviour seen when calibrating the pulse powers on a solid-state NMR spectrometer. Thirdly, figure 74 shows a continuous decrease in the signal intensity of the amorphous peak for an excitation angle of 30^{o}. In contrast, figure 73 shows an initial increase in the signal intensity at this angle and this persists up to a pulse offset of 12.5 kHz. The pulse offset behaviour of Refocused DIVAM will be further investigated with simulations from the SIMPSON program in the section below.

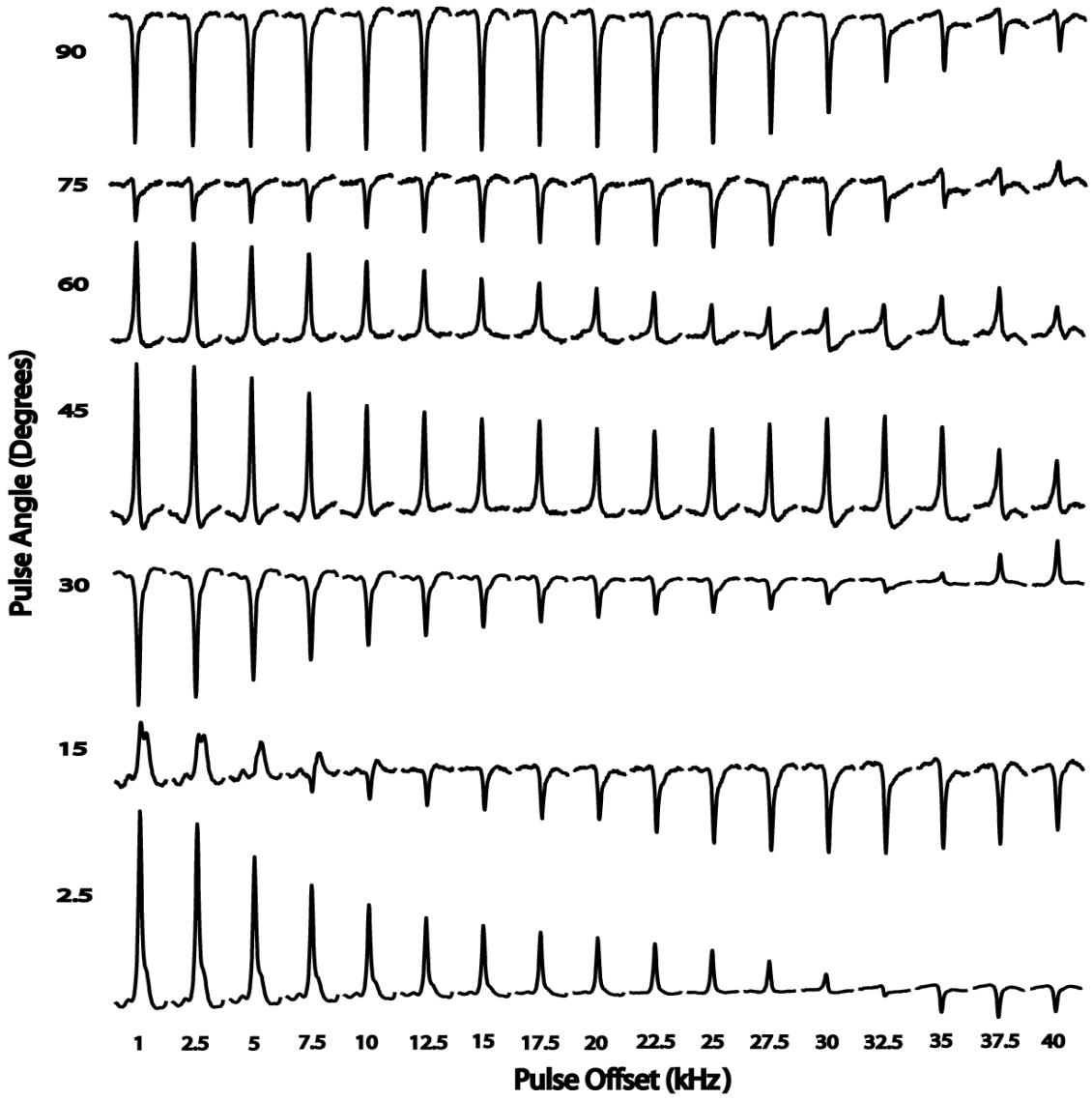

Figure 74 Pulse offset array of the ^{19}F Refocused DIVAM spectra of PVDF. This array is shown for selected excitation angles from 2.5 to 90 degrees using a MAS rate of 20 kHz, a 90^{o} pulse width of 2.5 μs, a 180^{o} pulse width of 5 μs, and an inter-pulse delay of 4.58 μs (T_F = 200 μs).

3.6.3 Simulations of the Pulse Offset Behaviour

Simulations of the pulse offset behavior for both the CSA and Dipolar terms of the Hamiltonian were carried out for both a fixed inter-pulse delay and excitation angle. These simulations should provide a valuable insight into how the behaviour of varying the pulse offset changes with respect to the spin dynamics of the system. It is important to note that both the CSA and Dipolar simulations do not take into account the chemical shift differences of the crystalline units with respect to the amorphous unit. The results presented below clearly show that the signal intensity oscillates with respect to the pulse offset used. This means that the earlier assumption that the oscillations of the amorphous signal were caused by the chemical shift differences between the amorphous and crystalline signals was not entirely correct. The following sections will investigate how the presence of various different CSA and dipolar coupling interaction strengths effects the signal oscillations observed with respect to the pulse offset used.

I. The Chemical Shift Anisotropy Term

Figures 75 and 76 show the response of the ^{19}F signal intensity, for a set of selected excitation angles and CSA strengths, as a function of the pulse offset used. These are analogous to the experimental results obtained in the two pulse offset arrays (figure 73 and 74) in that they used an inter-pulse delay of 2.5 μs (T_F = 150 μs) and 4.58 μs (T_F = 200 μs), respectively, and represent the sequences behaviour when rotor synchronized to 3 and 4 rotor periods, respectively. When examining figure 75 it is apparent that the pulse offset behaviour can lead to a great deal of selection based on the CSA term of the Hamiltonian. A large difference occurs in the first point of zero crossing

for CSA interaction strength less than 30 kHz. More importantly, the selection for all angles appears to be quite strong for small pulse offsets. This creates another situation in which overlapping domains with varying mobility, and therefore varying chemical shift anisotropies, can be selected using Refocused DIVAM.

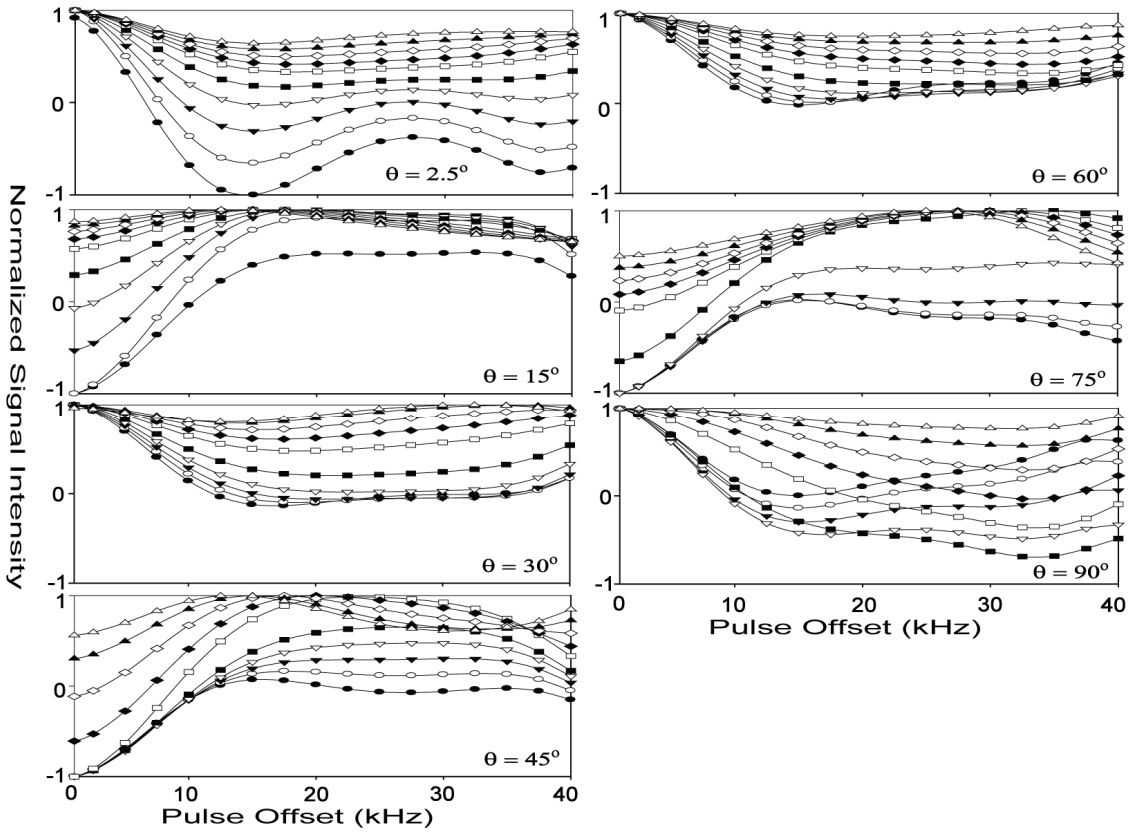

Figure 75 The effect of varying the pulse offset on the selectivity of the Refocused DIVAM pulse sequences for selected excitation angles and CSA values, where the excitation angle is indicated in the figure and the CSA values are represented by the following: ● = 1 kHz, ○ = 10 kHz, ▼ = 15 kHz, ▽ = 20 kHz, ■ = 25 kHz, □ = 30 kHz, ◆ = 32.5 kHz, and ◇ = 35 kHz, ▲ = 37.5 kHz, and △ = 40 kHz. These Simulations used real 100 kHz pulses with an MAS rate of 20 kHz, a 90° pulse width of 2.5 μs, a 180° pulse width of 5 μs, and an inter-pulse delay of 2.5 μs (T_F = 150 μs).

Earlier it was shown that the oscillations in the amorphous signal intensity during the experimental transient series closely resembled the simulated behaviour for CSA interaction strengths of 30-40 kHz. A series of similar conclusions can be made when

comparing the experimental and simulated oscillations of the signal during the pulse offset array. The excitation angle of 15^o is the only angle at which a zero crossing occurs experimentally (figure 73); however, as mentioned earlier, zero crossings can be seen for most excitation angles in the simulated array (figure 75). This restricts the comparison to the CSA strengths that do not lead to zero crossing at each of the remaining angles. Upon closer examination it is clear that for the excitation angles of 2.5^o, 30^o, 60^o, 75^o, and 90^o the simulated curves for a CSA strength of 30-40 kHz most closely resembles the experimental oscillations in the amorphous signal. This is in agreement with the conclusions from the transient series analysis performed earlier in this chapter. The only two exceptions to this conclusion are the excitation angles of 15^o and 45^o. In the case of an excitation angle of 45^o only a CSA strength of 37.5-40 kHz agrees with the oscillations observed experimentally. The excitation angle of 15^o is in complete disagreement with the above conclusion because at this angle only a CSA strength of 20 kHz or less could lead to the zero crossing observed experimentally. This disagreement could be caused by the lack of a dipolar interaction in these simulations or quite possibly the absence of relaxation effects.

Figure 76 illustrates the pulse offset behaviour for various CSA strengths when the Refocused DIVAM sequence is rotor synchronized to 4 rotor periods. It is clear that major differences are still present between the curves for the various CSA interaction strengths and that this can still lead to selection at most of the excitation angles. A zero crossing is only observed experimentally for the excitation angles of 15^o and 30^o and this again restricts our comparison of the curves for various CSA interaction strengths. In this case all of the remaining excitation angles require a CSA strength of 25 kHz or greater in

order to agree with the oscillations observed experimentally. This is slightly less than the 30 kHz or greater required when the sequence is rotor synchronized over 3 rotor periods and emphasizes, as mentioned earlier, that rotor synchronization must be considered when looking at all aspects of the selection mechanism. The excitation angles of 15^{o} and 30^{o} behave in a different manner than the other 5 angles and the curves corresponding to CSA strengths of 25-40 kHz no longer explain the oscillations seen experimentally. In the case of 15^{o} the zero crossing seen experimentally can only occur for CSA strengths of 15 kHz or less. Similarly, for an excitation angle of 30^{o} the experimental amorphous signal intensity initially decreases with increasing pulse offset and this behaviour can only be reproduced in simulation using a CSA strength of 20 kHz or less.

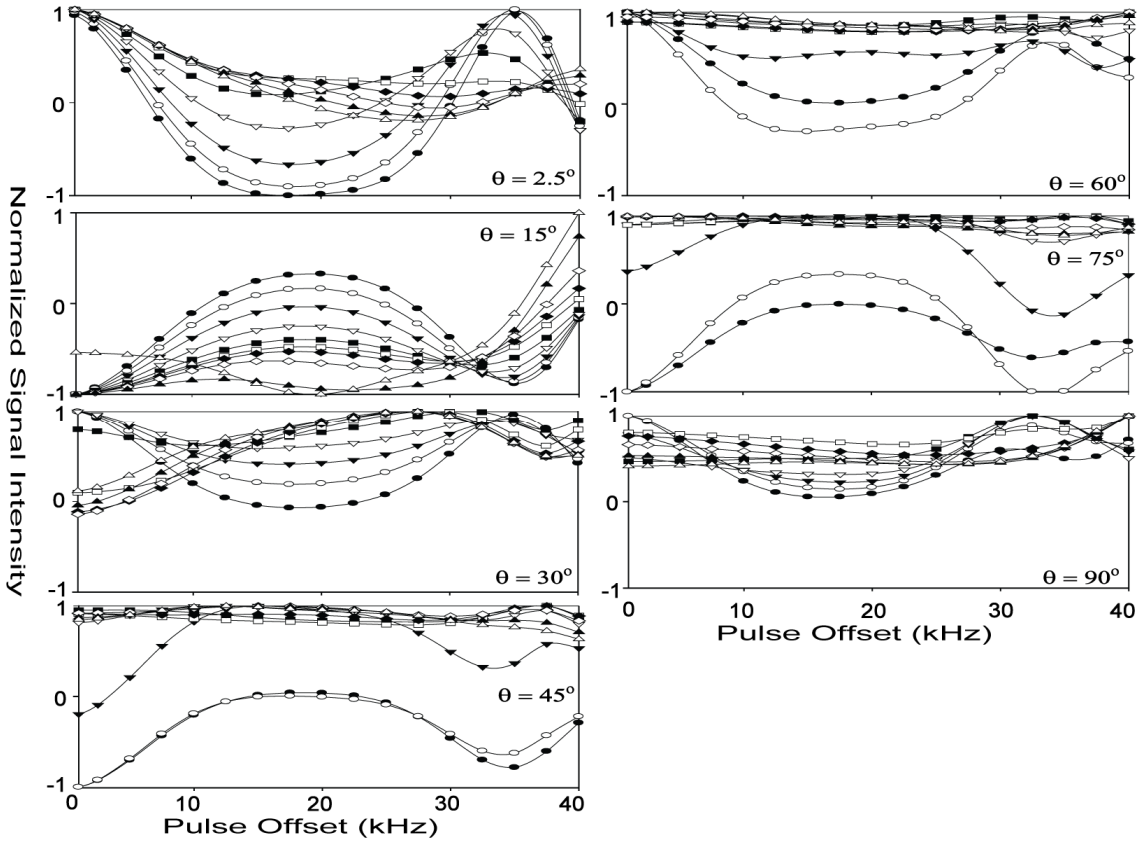

Figure 76 The effect of varying the pulse offset on the selectivity of the Refocused DIVAM pulse sequences for selected excitation angles and CSA values, where the excitation angle is indicated in the figure and the CSA values are represented by the following: ● = 1 kHz, ○ = 10 kHz, ▼ = 15 kHz, ▽ = 20 kHz, ■ = 25 kHz, □ = 30 kHz, ◆ = 32.5 kHz, and ◇ = 35 kHz, ▲ = 37.5 kHz, and △ = 40 kHz. These Simulations used real 100 kHz pulses with an MAS rate of 20 kHz, a 90° pulse width of 2.5 μs, a 180° pulse width of 5 μs, and an inter-pulse delay of 4.58 μs (T_F = 200 μs).

II. The Dipolar Coupling Term

Figures 77 and 78 show the response of the ^{19}F signal intensity, for a set of selected excitation angles and dipolar coupling strengths, as a function of the pulse offset used. These are analogous to the experimental results obtained in the two pulse offset arrays (figure 73 and 74) in that they used an inter-pulse delay of 2.5 μs (T_F = 150 μs) and 4.58 μs (T_F = 200 μs), respectively, and represent the sequences behaviour when rotor synchronized to 3 and 4 rotor periods, respectively. The first key observation can be

made when comparing the curves for various dipolar coupling strengths (figures 77 and 78) with those for the various CSA strengths (figures 75 and 76). In the case of the transient series, the dipolar and CSA curves for the same interaction strength were quite different. Surprisingly, when comparing the curves for similar dipolar and CSA strengths in the pulse offset array the curves follow similar trends. As a direct result, differences in dipolar coupling values can now lead to selection, via differences in zero crossings, when considered as a function of fixed excitation angle and variable pulse offset. The differences in the various curves for differing dipolar coupling strength is much smaller than with the CSA curves, but nonetheless it could lead to selection. In the transient series only the CSA leads to significant selection and the dipolar coupling term resulted in simple signal oscillations, but no zero crossings.

The oscillations in the signal intensity for each dipolar coupling strength in figure 77 can be directly compared to the oscillations in the amorphous signal intensity seen experimentally. It is important to recognize that a dipolar coupling of 50 kHz is highly unlikely in fluoropolymer systems; therefore, only interaction strengths of 25 kHz or less will be compared to the experimental results. All of the selected excitation angles, with the exception of 60^{o} and 75^{o}, have zero crossings for dipolar coupling strengths up to 25 kHz. In the CSA simulations, the experimental oscillations seen at an excitation angle of 15^{o} could not be explained by the simulations; however, the dipolar simulations for an excitation angle of 15^{o} do fit to the experimental oscillations. This supports the earlier argument that a set of simulations should be run in which the dipolar coupling value is fixed while the CSA strength is varied. This simulation could be used to better fit the observed experimental oscillations.

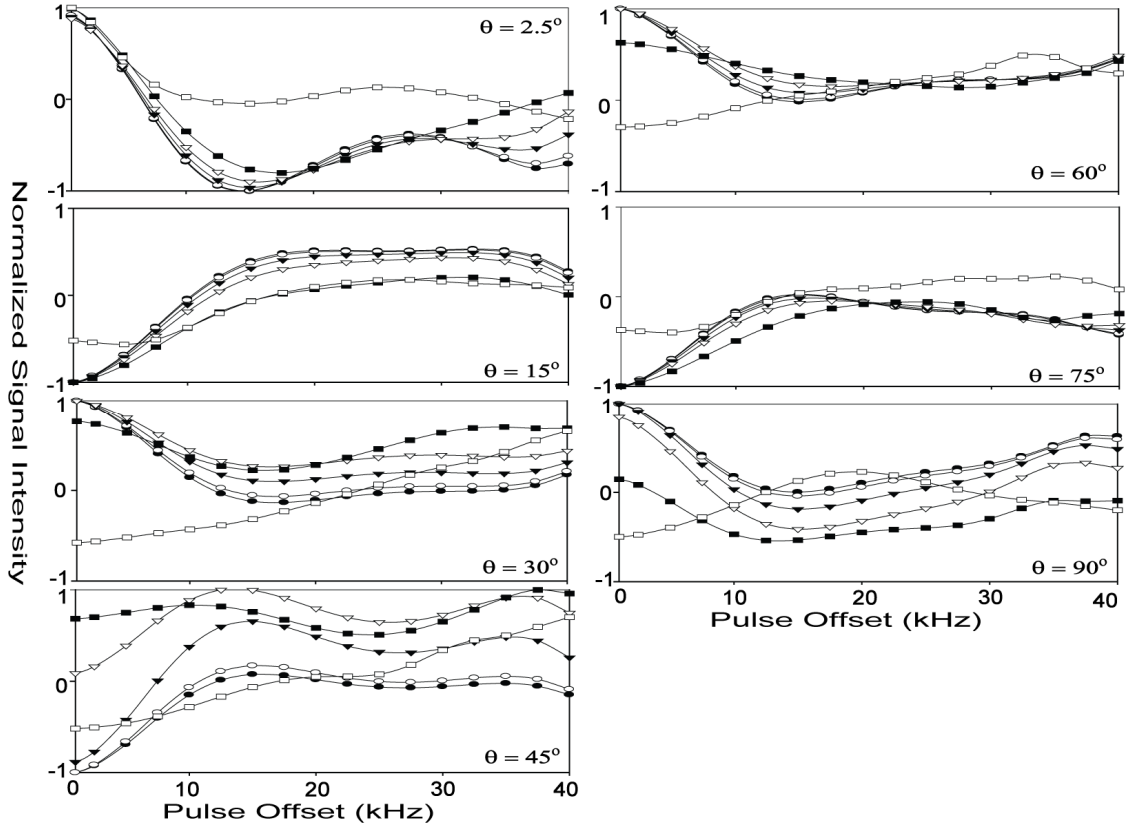

Figure 77 The effect of varying the pulse offset on the selectivity of the Refocused DIVAM pulse sequences for selected excitation angles and dipolar coupling values, where the excitation angle is indicated in the figure and the dipolar coupling values are represented by the following: ● = 1 kHz, ○ = 5 kHz, ▼ = 10 kHz, ▽ = 15 kHz, ■ = 25 kHz, and □ = 50 kHz. These Simulations used real 100 kHz pulses with an MAS rate of 20 kHz, a 90^o pulse width of 2.5 μs, a 180^o pulse width of 5 μs, and an inter-pulse delay of 2.5 μs (T_F = 150 μs).

Figure 78 illustrates the pulse offset behaviour for various dipolar coupling strengths when the Refocused DIVAM sequence is rotor synchronized to 4 rotor periods. Similarly to the CSA simulations, it is clear that a major difference is still present between the curves for the various dipolar coupling strengths and this can lead to selection at most of the excitation angles. Also, the oscillations seen for each of the various dipolar coupling strengths has changed now that the sequence is rotor synchronizing to 4 rotor periods instead of 3. This is in agreement with the behaviour

seen for the various CSA strengths and further indicates that the pulse offset behaviour varies dramatically based upon the rotor synchronization conditions.

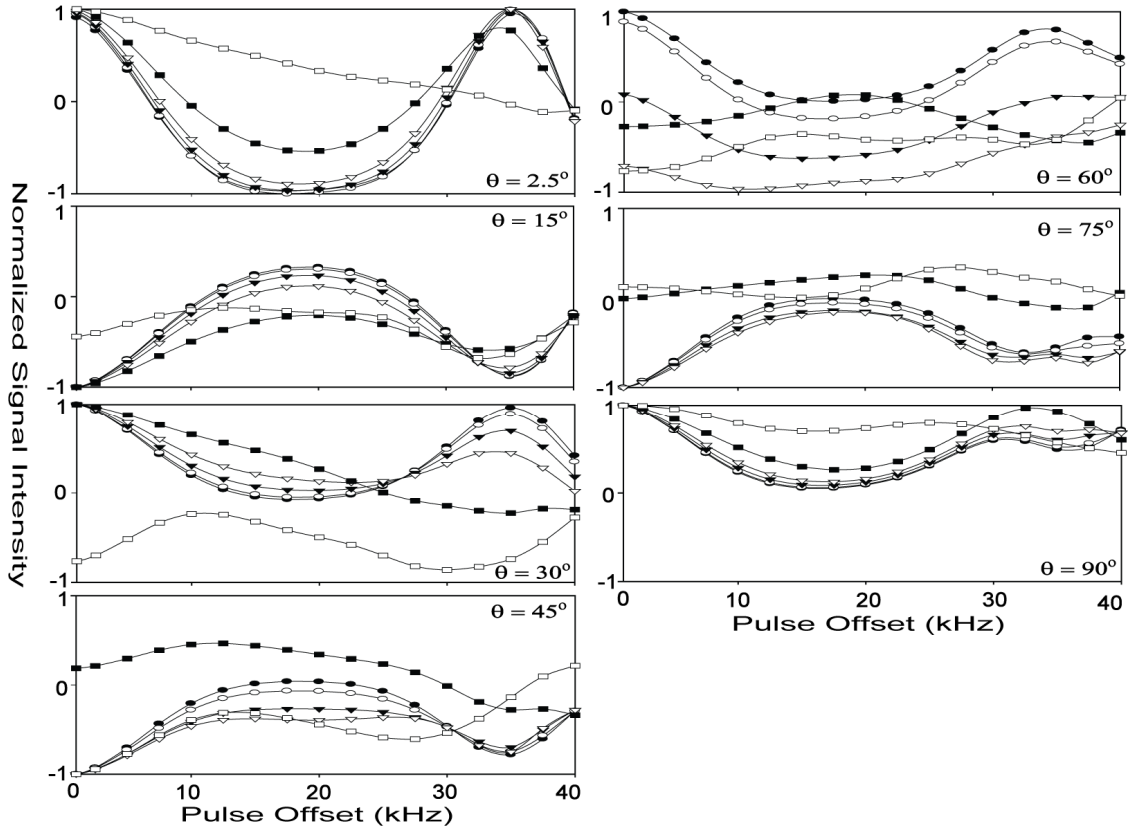

Figure 78 The effect of varying the pulse offset on the selectivity of the Refocused DIVAM pulse sequences for selected excitation angles and dipolar coupling values, where the excitation angle is indicated in the figure and the dipolar coupling values are represented by the following: ● = 1 kHz, ○ = 5 kHz, ▼ = 10 kHz, ▽ = 15 kHz, ■ = 25 kHz, and □ = 50 kHz. These Simulations used real 100 kHz pulses with an MAS rate of 20 kHz, a 90^o pulse width of 2.5 μs, a 180^o pulse width of 5 μs, and an inter-pulse delay of 4.58 μs (T_F = 200 μs).

3.6.4 Summary of the Pulse Offset Behaviour

It is clear that the pulse offset behaviour of Refocused DIVAM is quite complicated and must be considered when implementing the sequence. Experimental and simulation results both show pronounced oscillations in the amorphous signal intensity with respect to the pulse offset used. The simulations of the pulse offset array show that various CSA and Dipolar coupling strengths are sensitive to the pulse offset used and both terms can lead to zero crossings (domain selection). Earlier it was shown that, when the pulse offset is fixed, the Dipolar coupling is not expected to play a major role in the selection mechanism. The pulse offset now presents a way in which Refocused DIVAM can be used to select for various domains based upon both the CSA and dipolar coupling interactions. Furthermore, past use of the DIVAM sequences was based upon selection mechanisms that the user had no control over, such as the individual terms of the Hamiltonian or relaxation rates. Selection based upon the pulse offset shows promise as a method by which the user of the sequence can control the selection behaviour such that it is dominated by the interaction of their choice.

4. CONCLUSIONS AND FUTURE DIRECTIONS

A comparison of experimental and simulation data for both the Direct and Refocused DIVAM sequence provides an insight into their selection behaviour. Experimental nutation arrays of Direct DIVAM show that significant phase distortions are present when large excitation angles are used; furthermore, only the signal from the amorphous domain undergoes nutation. The experimental transient series illustrates that Direct DIVAM is sensitive to the rotor synchronization conditions of the sequence. A combination of analytical expressions and SIMPSON simulations illustrated that these problems were directly attributed to the isotropic offset and CSA dependence of the sequence. The analytical expressions illustrated that the selection mechanism can be driven by either relaxation or spin dynamics, depending on the excitation angle and inter-pulse delay used.

Experimental Refocused DIVAM nutation arrays demonstrate that the addition of both the refocusing pulses and a phase cycle has effectively removed the isotropic shift dependence of Direct DIVAM and that all of the signals in PVDF now nutate with respect to excitation angle. SIMPSON simulations show that the isotropic offset term has been completely removed from the selection mechanism and that Refocused DIVAM is more sensitive to the CSA term and less sensitive to the dipolar coupling term. The experimental transient series show oscillations in the signal amplitude with respect to the rotor phase, indicating that the orientational terms (CSA and Dipolar) of the Hamiltonian have an active role in the selection mechanism. SIMPSON simulations of the transient series indicate that the oscillations observed experimentally can be directly attributed to the CSA term. This further supports the conclusion that the CSA term is more involved in the selection mechanism of Refocused DIVAM than it was for Direct DIVAM and this

may be due to partial recoupling of the CSA interaction during the sequence. Refocused DIVAM now provides a far more robust method for directly applying the DIVAM sequence to the nucleus of interest, while removing the offset term from the selection process.

The experimental pulse offset arrays of Refocused DIVAM indicate that selection can be achieved by varying the pulse offset used, while fixing both the excitation angle and inter-pulse delay. SIMPSON simulations show that this is indeed the case and that varying the pulse offset can lead to selection via both the CSA and Dipolar term. This allows for selection to occur based upon small differences in the dipolar coupling values that otherwise would not lead to selection in the tradition DIVAM nutation arrays.

Further studies must be carried out on the Refocused DIVAM sequence to better understand how the selection mechanism is working. In order to model the spin dynamics effects properly and to accurately reproduce the nutation behaviour, a full treatment including the offset, CSA and dipole terms needs to be included, along with relaxation which is currently only available in one software suite known as SPINEVOLUTION.[125] A simpler approach would be to simulate the spin dynamics for the amorphous peak in PVDF with a fixed dipolar coupling and various different CSA values. This simulation could then also be carried out with a dipolar coupling corresponding to the crystalline signals, the correct chemical shift with respect to the amorphous peak, and various differing CSA values. This more complete simulation would allow for a better understanding of the experimental nutation and transient arrays of Refocused DIVAM for both the amorphous and crystalline signals. This may provide

insight into the possibility of using the observed nutation behaviour during the DIVAM sequence as a method of determining CSA values for overlapping spectral domains.

A set of Analytical expressions must be developed, similar to those seen for Direct DIVAM, but with the orientation dependence of the CSA term included. These expressions would allow for an understanding of how various different excitation angles and inter-pulse delays affect the observed selection in Refocused DIVAM. These analytical expressions would be very similar to the ones created for the dipolar interaction during the REDOR experiment.[126] An alternative approach to the use of analytical expressions would be to develop an average Hamiltonian treatment of the Refocused DIVAM sequence.[16, 31-32] This could provide useful insight into the symmetry properties of the Hamiltonian during the sequence, as is seen with the symmetry based recoupling sequences.[51, 54]

An alternative approach to understanding the behaviour of the signal intensities during the DIVAM sequences would be to create a two-dimensional plot. In this case the indirect dimension would be represented by the excitation angle used while the direct dimension would be either the inter-pulse delay or pulse offset used. This could make the interpretation of both the transient and pulse offset effects of Refocused and Direct DIVAM much easier. Similarly, a two-dimensional plot could be created in which the first dimension is the inter-pulse delay and the second dimension is the pulse offset. This could greatly simplify the interpretation of the combined behaviour of the pulse offset and inter-pulse delay for a fixed excitation angle.

The last area of potential development for the Refocused DIVAM sequence is centered on better understanding the effects of using a pulse offset larger than 5 kHz.

This can be simply done by co-adding the spectra from the equal, but opposite in sign, pulse offsets in the excitation profile of PVDF. This will provide a better understanding of how the chemical shift differences between the two crystalline units affects the phase of the amorphous peak in the co-added spectra of Refocused DIVAM. Secondly, the pulse offsets can be applied to only the excitation pulses and not the refocusing pulses. Currently, the pulse offsets are applied to all of the pulses in the Refocused DIVAM train and this change should increase the effective frequency range over which the isotropic offset term is refocused. Lastly, the transient behaviour of Refocused DIVAM can be simulated using pulse offsets larger than 5 kHz and this should provide a great deal of insight into the combined effects of the inter-pulse delay and pulse offset used in Refocused DIVAM.

REFERENCES

1. Bloch, F.; Hansen, W. W.; Packard, M. *Phys. Rev.* **1946,** *69*, 127-127.
2. Purcell, E. M.; Torrey, H. C.; Pound, R. V. *Phys. Rev.* **1946,** *69*, 37-38.
3. Grant, D. M.; Harris, R. K., *Encyclopedia of Nuclear Magnetic Resonance*. Wiley: 1996.
4. Gullion, T.; Schaefer, J. *J. Magn. Reson.* **1989,** *81*, 196-200.
5. Hing, A. W.; Vega, S.; Schaefer, J. *J. Magn. Reson.* **1992,** *96*, 205-209.
6. Gullion, T. *Concept. Magn. Reson.* **1998,** *10*, 277-289.
7. Huettel, S. A.; Song, A. W.; McCarthy, G. *Functional Magnetic Resonance Imaging*. Sinauer Associates Inc.: Sunderland, 2004.
8. Friebolin, H. *Basic One- and Two-Dimensional NMR Spectroscopy*. Wiley-VCH: Verlag, 2005.
9. Sanders, J. K. M.; Hunter, B. K. *Modern NMR Spectroscopy: A Guide for Chemists*. Oxford University Press: Oxford, 1993.
10. Keeler, J. *Understanding NMR Spectroscopy*. Wiley: Chichester, 2005.
11. French, A. P.; Taylor, E. F. *An Introduction to Quantum Physics*. W. W. Norton and Company: New York, 1978.
12. Serway, R. A.; Moses, C. J.; Moyer, C. A. *Modern Physics*. 3rd ed.; Brooks/Cole-Thomson Learning: Belmont, 2005.
13. Levitt, M. H. *Spin Dynamics: Basics of Nuclear Magnetic Resonance*. 2nd ed.; Wiley: Chichester, 2008.
14. Slichter, C. P. *Principles of Magnetic Resonance*. 3rd ed.; Springer: New York, 1990.
15. Duer, M. J. *NMR Spectroscopy: Principles and Apllications*. Blackwell Science: Oxford, 2002.
16. Schmidt-Rohr, K.; Spiess, H. W. *Multidimensional Solid-State NMR and Polymers*. Academic Press: London, 1994.
17. Cavanaugh, J.; Fairbrother, W. J.; Palmer, A. G.; Rance, M.; Skelton, N. J. *Protein NMR Spectroscopy: Principles and Practices*. 2nd ed.; Academic Press: Burlington, 2007.
18. Borisov, A. S.; Hazendonk, P.; Hayes, P. G. *J. Inorg. Organomet. Polym. Mater.* **2010,** *20*, 183-212.
19. Halliday, D.; Resnick, R.; Walker, J. *Fundamentals of Physics*. 6th ed.; Wiley: New York, 2001.
20. Laukien, D. D.; Tschopp, W. H. *Concept. Magn. Reson.* **1994,** *6*, 255-273.
21. Doty, F. D.; Entzminger, G.; Yang, Y. A. *Concept. Magn. Reson.* **1998,** *10*, 133-156.
22. Doty, F. D.; Entzminger, G.; Yang, Y. A. *Concept. Magn. Reson.* **1998,** *10*, 239-260.
23. Traficante, D. D. *Concept. Magn. Reson.* **1990,** *2*, 181-195.
24. Boas, M. L. *Mathematical Methods in the Physical Sciences*. 3rd ed.; Wiley: New York, 2006.
25. Zare, R. N. *Angular Momentum: Understanding Spatial Aspects in Chemistry and Physics*. 1st ed.; John Wiley & Sons, Inc.: New York, 1988.

26. Ratner, M. A.; Schatz, G. C. *Introduction to Quantum Mechanics in Chemistry*. Prentice Hall: Upper Saddle River, 2001.
27. Holzner, S. *Quantum Physics for Dummies*. Wiley: Hoboken, 2009.
28. Al-Khalili, J. *Quantum: A Guide for the Perplexed*. Weidenfeld and Nicolson: London, 2003.
29. Satterlee, J. D. *Concept. Magn. Reson.* **1990,** *2,* 119-129.
30. Satterlee, J. D. *Concept. Magn. Reson.* **1990,** *2,* 69-79.
31. Haeberlen, U. In *Advances in Magnetic Resonance*; Academic Press: New York, 1976.
32. Duer, M. J. *NMR Spectroscopy: Principles and Applications*. Blackwell Science: Oxford, 2002.
33. Pake, G. E.; Purcell, E. M. *Phys. Rev.* **1948,** *74,* 1184-1188.
34. Wasylishen, R. E. In *Encyclopedia of Magnetic Resonance*; Grant, D. M.,Harris, R. K., Eds.; Elsevier: New York, 1996; pp 3901-3904.
35. Ashbrook, S. E.; Duer, M. J. *Concept. Magn. Reson. A.* **2006,** *28A,* 183-248.
36. Lowe, I. J. *Phys. Rev. Lett.* **1959,** *2,* 285-287.
37. Andrew, E. R.; Bradbury, A.; Eades, R. G. *Nature* **1959,** *183,* 1802-1803.
38. Schaefer, J.; Stejskal, E. O. *J. Am. Chem. Soc.* **1976,** *98,* 1031-1032.
39. Samoson, A.; Tuherm, T.; Gan, Z. *Solid State Nucl. Magn. Reson.* **2001,** *20,* 130-136.
40. Ernst, M. *J. Magn. Reson.* **2003,** *162,* 1-34.
41. Bennett, A. E.; Rienstra, C. M.; Auger, M. l.; Lakshmi, K. V.; Griffin, R. G. *J. Chem. Phys.* **1995,** *103,* 6951.
42. Bräuniger, T.; Wormald, P.; Hodgkinson, P. *Monatsh. Chem.* **2002,** *133,* 1549-1554.
43. Fung, B. M.; Khitrin, A. K.; Ermolaev, K. *J. Magn. Reson.* **2000,** *142,* 97-101.
44. Gan, Z. H.; Ernst, R. R. *Solid State Nucl. Magn. Reson.* **1997,** *8,* 153-159.
45. Sakellariou, D.; Lesage, A.; Hodgkinson, P.; Emsley, L. *Chem. Phys. Lett.* **2000,** *319,* 253-260.
46. Vinogradov, E.; Madhu, P. K.; Vega, S. *Chem. Phys. Lett.* **1999,** *314,* 443-450.
47. Yu, Y.; Fung, B. M. *J. Magn. Reson.* **1998,** *130,* 317-320.
48. Detken, A.; Hardy, E. H.; Ernst, M.; Meier, B. H. *Chem. Phys. Lett.* **2002,** *356,* 298-304.
49. Liu, S. F.; Schmidt-Rohr, K. *Macromolecules* **2001,** *34,* 8416-8418.
50. Gullion, T.; Baker, D. B.; Conradi, M. S. *J. Magn. Reson.* **1990,** *89,* 479-484.
51. Brinkmann, A.; Levitt, M. H. *J. Chem. Phys.* **2001,** *115*.
52. Carravetta, M.; Edén, M.; Zhao, X.; Brinkmann, A.; Levitt, M. H. *Chem. Phys. Lett.* **2000,** *321,* 205-215.
53. Eden, M.; Levitt, M. H. *J. Chem. Phys.* **1999,** *111,* 1511.
54. Kristiansen, P. E.; Carravetta, M.; van Beek, J. D.; Wai Cheu, L.; Levitt, M. H. *J. Chem. Phys.* **2006,** *124,* N.PAG.
55. Lee, Y. K.; Kurur, N. D.; Helmle, M.; Johannessen, O. G.; Nielsen, N. C.; Levitt, M. H. *Chem. Phys. Lett.* **1995,** *242,* 304-309.
56. Madhu, P. K.; Zhao, X.; Levitt, M. H. *Chem. Phys. Lett.* **2001,** *346,* 142-148.
57. Zhao, X.; Edén, M.; Levitt, M. H. *Chemical Physics Letters* **2001,** *342,* 353-361.

58. Zhao, X.; Hoffbauer, W.; Schmedt auf der Günne, J.; Levitt, M. H. *Solid State Nucl. Magn. Reson.* **2004,** *26*, 57-64.
59. Rance, M.; Byrd, R. A. *J. Magn. Reson.* **1983,** *52*, 221-240.
60. Hartmann, S. R.; Hahn, E. L. *Phys. Rev.* **1962,** *128*, 2042-&.
61. Hazendonk, P.; Harris, R. K.; Galli, G.; Pizzanelli, S. *Phys. Chem. Chem. Phys.* **2002,** *4*, 507-513.
62. Rovnyak, D. *Concept. Magn. Reson. A.* **2008,** *32A*, 254-276.
63. Taylor, R. E. *Concept. Magn. Reson. A.* **2004,** *22A*, 37-49.
64. Kupce, E.; Freeman, R. *J. Magn. Reson. Ser. A* **1995,** *115*, 273-276.
65. Ernst, R. R. *Chimia* **1987,** *41*, 323-340.
66. Aue, W. P.; Bartholdi, E.; Ernst, R. R. *J. Chem. Phys.* **1976,** *64*, 2229-2246.
67. Harris, R. K.; Jackson, P. *Chem. Rev.* **1991,** *91*, 1427-1440.
68. Harris, R. K.; Monti, G. A.; Holstein, P. In *Solid State NMR of Polymers*; Ando, I.,Asakura, T., Eds.; Elsevier: New York, 1998; pp 667-712.
69. Bak, M.; Rasmussen, J. T.; Nielsen, N. C. *J. Magn. Reson.* **2000,** *147*, 296-330.
70. Smith, S. A.; Levante, T. O.; Meier, B. H.; Ernst, R. R. *J. Magn. Reson. Ser. A* **1994,** *106*, 75-105.
71. Welch, B. B. *Practical Programming in Tcl and Tk*. Prentice Hall: Englewood Cliffs, 1995.
72. Hu, B.; Delevoye, L.; Lafon, O.; Trebosc, J.; Amoureux, J. P. *J. Magn. Reson.* **2009,** *200*, 178-188.
73. Eden, M.; Levitt, M. H. *J. Magn. Reson.* **1998,** *132*, 220-239.
74. Bak, M.; Nielsen, N. C. *J. Magn. Reson.* **1997,** *125*, 132-139.
75. Mark, J. E.; Allcock, H. R.; West, R. *Inorganic Polymers*. 2nd ed.; Oxford University Press: New York, 2005.
76. Takayama, T. In *Solid State NMR of Polymers*; Ando, I.,Asakura, T., Eds.; Elsevier: New York, 1998; pp 612-666.
77. Yamanobe, T. In *Solid State NMR of Polymers*; Ando, I.,Asakura, T., Eds.; Elsevier: New York, 1998; pp 267-305.
78. Dolbier, W. R. *J. Fluorine Chem.* **2005,** *126*, 157-163.
79. Nalwa, H. S. *J. Macromol. Sci.-Rev. Macromol. Chem. Phys.* **1991,** *C31*, 341-432.
80. Park, J. W.; Seo, Y. A.; Kim, I.; Ha, C. S.; Aimi, K.; Ando, S. *Macromolecules* **2004,** *37*, 429-436.
81. Lovinger, A. J. *Science* **1983,** *220*, 1115-1121.
82. Katoh, E.; Ogura, K.; Ando, I. *Polym. J.* **1994,** *26*, 1352-1359.
83. Holstein, P.; Harris, R. K.; Say, B. J. *Solid State Nucl. Magn. Reson.* **1997,** *8*, 201-206.
84. Holstein, P.; Scheler, U.; Harris, R. K. *Polymer* **1998,** *39*, 4937-4941.
85. Hucher, C.; Beaume, F.; Eustache, R. P.; Tekely, P. *Macromolecules* **2005,** *38*, 1789-1796.
86. Wormald, P.; Ameduri, B.; Harris, R. K.; Hazendonk, P. *Solid State Nucl. Magn. Reson.* **2006,** *30*, 114-123.
87. Holstein, P.; Scheler, U.; Harris, R. K. *Magn. Reson. Chem.* **1997,** *35*, 647-649.
88. Wormald, P.; Apperley, D. C.; Beaume, F.; Harris, R. K. *Polymer* **2003,** *44*, 643-651.

89. Scheler, U.; Harris, R. K. *Solid State Nucl. Magn. Reson.* **1996,** *7*, 11-16.
90. Holstein, P.; Monti, G. A.; Harris, R. K. *Phys. Chem. Chem. Phys.* **1999,** *1*, 3549-3555.
91. Ando, S.; Harris, R. K.; Holstein, P.; Reinsberg, S. A.; Yamauchi, K. *Polymer* **2001,** *42*, 8137-8151.
92. Ando, S.; Harris, R. K.; Reinsberg, S. A. *Magn. Reson. Chem.* **2002,** *40*, 97-106.
93. Hu, B.; Trebosc, J.; Amoureux, J. P. *J. Magn. Reson.* **2008,** *192*, 112-122.
94. Nielsen, N. C.; Bildsoe, H.; Jakobsen, H. J.; Levitt, M. H. *J. Chem. Phys.* **1994,** *101*, 1805.
95. Caravatti, P.; Bodenhausen, G.; Ernst, R. R. *Chem. Phys. Lett.* **1982,** *89*, 363-367.
96. Caravatti, P.; Braunschweiler, L.; Ernst, R. R. *Chem. Phys. Lett.* **1983,** *100*, 305-310.
97. Bennett, A. E.; Griffin, R. G.; Ok, J. H.; Vega, S. *J. Chem. Phys.* **1992,** *96*, 8624.
98. Bennett, A. E.; Rienstra, C. M.; Griffiths, J. M.; Zhen, W. G.; Lansbury, P. T.; Griffin, R. G. *J. Chem. Phys.* **1998,** *108*, 9463-9479.
99. Lesage, A.; Auger, C.; Caldarelli, S.; Emsley, L. *J. Am. Chem. Soc.* **1997,** *119*, 7867-7868.
100. Lesage, A.; Bardet, M.; Emsley, L. *J. Am. Chem. Soc.* **1999,** *121*, 10987-10993.
101. Lesage, A.; Sakellariou, D.; Steuernagel, S.; Emsley, L. *J. Am. Chem. Soc.* **1998,** *120*, 13194-13201.
102. Lesage, A.; Emsley, L. *J. Magn. Reson.* **2001,** *148*, 449-454.
103. Schmidt-Rohr, K. *Abstr. Pap. Am. Chem. S.* **1994,** *208*, 111-PMSE.
104. Buda, A.; Demco, D. E.; Bertmer, M.; Blumich, B.; Reining, B.; Keul, H.; Hocker, H. *Solid State Nucl. Magn. Reson.* **2003,** *24*, 39-67.
105. Ando, S.; Harris, R. K.; Hazendonk, P.; Wormald, P. *Macromol. Rapid Commun.* **2005,** *26*, 345-356.
106. Harris, D. J.; de Azevedo, E. R.; Bonagamba, T. J. *J. Magn. Reson.* **2003,** *162*, 67-73.
107. Ando, S.; Harris, R. K.; Reinsberg, S. A. *J. Magn. Reson.* **1999,** *141*, 91-103.
108. Kenwright, A.; Say, B. J. In *NMR Spectroscopy of Polymers*; Ibbett, R. N., Ed. Blackie Academic: Glasgow, 1993; pp 231-274.
109. Hu, J. Z.; Taylor, C. M. V.; Pugmire, R. J.; Grant, D. M. *J. Magn. Reson.* **2001,** *152*, 7-13.
110. Mao, J. D.; Schmidt-Rohr, K. *J. Magn. Reson.* **2003,** *162*, 217-227.
111. Opella, S. J.; Frey, M. H. *J. Am. Chem. Soc.* **1979,** *101*, 5854-5856.
112. Cai, W. Z.; Schmidt-Rohr, K.; Egger, N.; Gerharz, B.; Spiess, H. W. *Polymer* **1993,** *34*, 267-276.
113. Egger, N.; Schmidt-Rohr, K.; Blumich, B.; Domke, W. D.; Stapp, B. *J. Appl. Polym. Sci.* **1992,** *44*, 289-295.
114. Hazendonk, P.; Harris, R. K.; Ando, S.; Avalle, P. *J. Magn. Reson.* **2003,** *162*, 206-216.
115. Borisov, A. S.; Hazendonk, P.; Hayes, P. G. *J. Inorg. Organomet. Polym. Mater.* **2008,** *18*, 163-174.
116. Hazendonk, P.; deDenus, C.; Iuga, A.; Cahoon, P.; Nilsson, B.; Iuga, D. *J. Inorg. Organomet. Polym. Mater.* **2006,** *16*, 343-357.

117. Hazendonk, P.; Wormald, P.; Montina, T. *J. Phys. Chem. A* **2008,** *112,* 6262-6274.
118. Teyssedre, G.; Bernes, A.; Lacabanne, C. *J. Polym. Sci. Pol. Phys.* **1993,** *31,* 2027-2034.
119. Nakagawa, K.; Ishida, Y. *J. Polym. Sci. Pol. Phys.* **1973,** *11,* 2153-2171.
120. van Beek, J. D. *J. Magn. Reson.* **2007,** *187,* 19-26.
121. Herzfeld, J.; Berger, A. E. *J. Chem. Phys.* **1980,** *73,* 6021-6030.
122. Bodenhausen, G.; Freeman, R.; Morris, G. A. *J. Magn. Reson.* **1976,** *23,* 171-175.
123. Morris, G. A.; Freeman, R. *J. Magn. Reson.* **1978,** *29,* 433-462.
124. Chen, Q.; Schmidt-Rohr, K. *Macromolecules* **2004,** *37,* 5995-6003.
125. Veshtort, M.; Griffin, R. G. *J. Magn. Reson.* **2006,** *178,* 248-282.
126. Mueller, K. T. *J. Magn. Reson. Ser. A* **1995,** *113,* 81-93.

APPENDIX 1: SIMPSON DIRECT DIVAM CODE

```
# Direct DIVAM single spin simulation.
# Array all excitation angles

spinsys {
    channels 19F
    nuclei 19F
    shift 1 0 0 0 0 0 0
        }

par {
    spin_rate        20000
    gamma_angles     30
    crystal_file     rep168
    np               37
    start_operator   Inz
    detect_operator  I1z
    proton_frequency 500e6
    verbose          1101
}

proc pulseq {} {
    global par
    maxdt 1

      for {set i 0} {$i < $par(np)} {incr i} {
            reset
            for {set k 0} {$k < 12} {incr k} {

                  pulse 2.5 [expr $i*2.5*1e6/900] x
                  delay 2.5
                  }
            acq }
}

proc main {} {
   global par

#index o is the index of interaction values to run

   foreach o {{27500} {32500} {35000} {37500} {40000} {42500} {45000}
{47500}} {

   set csa        [lindex $o 0]
   set fd [fsimpson [list [list \shift_1_aniso $csa]]]
   fsave $fd $par(name)-$csa.tmp

   set aaa [open $par(name)-totalz-$csa.xy w]
   for {set i 1} {$i <= $par(np)} {incr i} {
      puts $aaa "[expr ($i-1)*2.5], [findex $fd $i -re]"}
   close $aaa

   funload
}
}
```

APPENDIX 2: SIMPSON REFOCUSED DIVAM CODE

```
# Offset Compensated DIVAm single spin simulation.
# Array all excitation angles


spinsys {
    channels 19F
    nuclei 19F
    shift 1 0 0 0 0 0 0
        }

par {
    spin_rate        20000
    gamma_angles     30
    crystal_file     rep168
    np               37
    start_operator   Inz
    detect_operator  I1z
    proton_frequency 500e6
    verbose          1101

}

proc pulseq {} {
    global par

    maxdt 1

      for {set i 0} {$i < $par(np)} {incr i} {
            reset
            for {set k 0} {$k < 6} {incr k} {
                  offset $par(offset)
                  pulse 2.5 [expr $i*2.5*1e6/900] $par(p1)
                  delay 2.5
                  pulse 5 100000 $par(p2)
                  delay 2.5
                  pulse 2.5 [expr $i*2.5*1e6/900] $par(p3)
                  delay 2.5
                  pulse 5 100000 $par(p4)
                  delay 2.5
                  }
            acq }
            }

proc main {} {
   global par

#index o is the index of interaction values to run

   foreach o {{27500} {32500} {35000} {37500} {40000} {42500} {45000}
{47500}} {

#index pp is the index of the two offsets to use

   foreach pp {{1000 0} {-1000 1}} {
```

```
#index p is the index containing the phase table for the pulses

   foreach p {{x y -x -y 1} {x -y -x y 2} {x x x -x 3} {x -x x x 4}
              {-x x -x -x 5} {-x -x -x x 6} {-x y x -y 7} {-x -y x y 8}
              {y y y -y 9} {y -y y y 10} {y x -y -x 11} {y -x -y x 12}
              {-y y -y -y 13} {-y -y -y y 14} {-y x y -x 15} {-y -x y x
16}} {


      set csa           [lindex $o 0]
      set par(offset)         [lindex $pp 0]
      set num           [expr [lindex $p 4]+[expr [lindex $pp 1]*16]]
      set par(p1)       [lindex $p 0]
      set par(p2)       [lindex $p 1]
      set par(p3)       [lindex $p 2]
      set par(p4)       [lindex $p 3]
      set par(model)    $par(name)-$num


   set fd [fsimpson [list [list \shift_1_aniso $csa]]]


   fsave $fd $par(model)-$csa.tmp

}
}

   funload $fd

   #section for the addition of the 16 cyclops scans
   #simple load function to add function to open and put function

   set aa [fload OSCOMP-RS-re100Khz-csa-final-cyclops-1-$csa.tmp]

      for {set int 2} {$int <= 32} {incr int} {
            set ab [fload OSCOMP-RS-re100Khz-csa-final-cyclops-$int-
$csa.tmp]
            fadd $aa $ab
            }

   set aaa [open $par(name)-totalz-$csa.xy w]
   for {set i 1} {$i <= $par(np)} {incr i} {
      puts $aaa "[expr ($i-1)*2.5], [findex $aa $i -re]"}
   close $aaa


   funload
}
}
```